

Copyright
by
PENG DONG
2010

The Dissertation Committee for PENG DONG Certifies that this is the approved version of the following dissertation:

Laboratory Visualization of Laser-Driven Plasma Accelerators in the Bubble Regime

Committee:

Downer, Michael C., Supervisor

Becker, Michael

Ditmire, Todd

Lang, Karol

Shvets, Gennady

**Laboratory Visualization of Laser-Driven Plasma Accelerators in
the Bubble Regime**

by

PENG DONG, B.S.

Dissertation

Presented to the Faculty of the Graduate School of

The University of Texas at Austin

in Partial Fulfillment

of the Requirements

for the Degree of

Doctor of Philosophy

The University of Texas at Austin

May, 2010

Dedication

I dedicate this dissertation to my parents.

Acknowledgements

I would like to express the deepest appreciation to my supervisor, Professor Mike Downer, who has the attitude and the substance of a genius: he continually and convincingly conveyed a spirit of adventure in regard to research and scholarship, and an excitement in regard to teaching. Without his guidance and persistent help this dissertation would not have been possible.

I would like to thank my committee members for their wisdom and excellent advice throughout the years, and for agreeing to be part of my committee.

I would like to express special thanks to Nicolas Matlis, Chris McGuffey and Steve Reed for their advice, experience and help that made the experiment possible. I would like to thank my Michigan collaborators Anatoly Maksimchuk, Victor Yanovsky, Takeshi Matsuoka, Vladimir Chvykov, Galina Kalintchenko, Karl Krushelnick. I also wish to thank Professor Gennady Shvets, Austin Yi and Serguei Kalmykov for their theoretical support.

I thank all the members of the lab: Yongquian An, Benjamin Bowes, Ramon Carriles, Dongsu Du, Robert Ehlert, Peter Figliozzi, Xiaohui Gao, Franklin Grigsby, Watson Henderson, Jinhee Kwon, Ming Lei, Zhengyan Li, J.C. Sanders, Bonggu Shim, P. J. Smith, Liangfeng Sun, Xiaoming Wang, Junwei Wei. It's a great pleasure to work with them all these years.

Laboratory Visualization of Laser-Driven Plasma Accelerators in the Bubble Regime

Publication No. _____

PENG DONG, Ph.D.

The University of Texas at Austin, 2010

Supervisor: Michael C. Downer

Accurate single-shot visualization of laser wakefield structures can improve our fundamental understanding of plasma-based accelerators. Previously, frequency domain holography (FDH) was used to visualize weakly nonlinear sinusoidal wakes in plasmas of density $n_e < 0.6 \times 10^{19}/\text{cm}^3$ that produced few or no relativistic electrons. Here, I address the more challenging task of visualizing highly nonlinear wakes in plasmas of density $n_e \sim 1$ to $3 \times 10^{19}/\text{cm}^3$ that can produce high-quality relativistic electron beams. Nonlinear wakes were driven by 30 TW, 30 fs, 800 nm pump pulses. When bubbles formed, part of a 400 nm, co-propagating, overlapping probe pulse became trapped inside them, creating a light packet of plasma wavelength dimensions — that is, an optical "bullet" — that I reconstruct by FDH methods. As n_e increased, the bullets first appeared at $0.8 \times 10^{19}/\text{cm}^3$, the first observation of bubble formation below the electron capture threshold. WAKE simulations confirmed bubble formation without electron capture and the trapping of optical bullets at this density. At $n_e > 1 \times 10^{19}/\text{cm}^3$, bullets appeared with high shot-to-shot stability together with quasi-monoenergetic relativistic electrons. I also directly observed the temporal walk-off of the optical bullet from the

beam-loaded plasma bubble revealed by FDH phase shift data, providing unprecedented visualization of the electron injection and beam loading processes.

There are five chapters in this thesis. Chapter 1 introduces general laser plasma-based accelerators (LPA). Chapter 2 discusses the FDH imaging technique, including the setup and reconstruction process. In 2006, Dr. N. H. Matlis used FDH to image a linear plasma wakefield. His work is also presented in Chapter 2 but with new analyses. Chapter 3, the main part of the thesis, discusses the visualization of LPAs in the bubble regime. Chapter 4 presents the concept of frequency domain tomography. Chapter 5 suggests future directions for research in FDH.

Table of Contents

List of Figures	xi
List of Tables	xii
Chapter 1. Introduction to Laser-Plasma Particle Acceleration	1
1.1. Conventional Particle Accelerators.....	4
1.1.1. Applications	5
1.1.2. Types of accelerators	8
1.1.3. Fundamental limitation of conventional accelerators	10
1.2. Direct Laser Acceleration (DLA)	10
1.2.1. Lorentz equation: Laser-interaction with single particles..	12
1.2.2. Lawson criterion and its limits.....	14
1.2.3. Examples of DLA experiments.....	15
1.2.4. Limitations of direct laser acceleration.....	16
1.3. Laser-Plasma Electron Acceleration (LPA).....	18
1.3.1. Space charge fields in a perturbed plasma	19
1.3.2. Ponderomotive force: Creation of a Langmuir wave.....	20
1.3.3. Types of laser-plasma electron accelerators	23
1.3.3.1. Resonantly-driven linear plasma waves: LWFA	23
1.3.3.2. Plasma Beat-Wave Accelerator (PBWA)	24
1.3.3.3. Far-off-resonantly-driven plasma waves: Self-modulated LWFA	24
1.3.3.4. Raman beam seeded acceleration.....	25
1.3.3.5. Resonantly driven, strongly nonlinear, broken plasma waves: Bubble regime.....	25
1.3.4. Limitations to acceleration length.....	27
1.3.4.1. Diffraction length	27
1.3.4.2. Dephasing length.....	29
1.3.4.3. Depletion length	31

1.3.5.	Emerging applications of monoenergetic laser-plasma electron accelerators	32
1.3.6.	How far can laser-plasma electron accelerators go?.....	33
Chapter 2.	Visualization of Laser Wakefields in Tenuous Plasma: Frequency-Domain Holography.....	35
2.1.	Why we need to see laser wakefields directly.	35
2.2.	Why it is difficult to visualize laser wakefields.....	36
2.3.	Previous methods for characterizing laser wakefields in tenuous plasma	37
2.4.	Single-shot visualization: basics of FDH.....	38
2.4.1.	The plasma object	39
2.4.2.	Reference and probe pulses.	40
2.4.3.	Recording frequency-domain holograms.....	41
2.4.4.	Reading frequency-domain holograms	43
2.5.	Holographic Images of Laser Wakefields.....	44
2.6.	Summary	51
Chapter 3.	Visualization of Laser Wakefields in Dense Plasma: Frequency-Domain Shadowgraphy.....	58
3.1.	New issues in visualizing dense plasma structures.....	59
3.2.	Previous methods of characterizing laser wakes in dense plasma	60
3.3.	Experimental procedure for single-shot visualization of bubbles.....	62
3.4.	Electron Generation	66
3.5.	Optical bullets	72
3.6.	Simulation of plasma bubble and optical bullet formation.....	78
3.7.	comparison of phase and amplitude reconstruction	84
3.8.	Conclusions.....	88
Chapter 4.	Visualization of evolving laser wakefields: frequency-domain tomography	98
4.1.	Concept of Frequency Domain Tomography	98
4.2.	Simulations of phase streaks.....	99
4.3.	Prototype frequency-domain streak camera.....	101

4.4. Simulations of Multi-Frame “Movie” reconstruction.....	101
4.5. Design of frequency-domain streak camera for the Texas Petawatt Laser- Plasma Acceleration Experiment.....	103
Chapter 5. Future directions	112
5.1. Visualization of beam-driven PWFAs	112
5.2. Visualization of channeled LWFAs.....	114
Appendix: Publications by the Author.....	119
Bibliography	120
Vita	129

List of Figures

Figure 1-1.	Characteristic orbits of free electron in a mildly relativistic linearly polarized laser field in its average rest frame.....	13
Figure 2-1.	Schematic Frequency Domain Holography (FDH) configuration for imaging laser wakefields.	52
Figure 2-2.	Practical FDH configuration for imaging laser wakefields.	53
Figure 2-3.	Reconstructing probe electric field.	54
Figure 2-4.	Single-shot image of a wakefield produced by a 30 TW laser pulse in plasma of electron density $n_e = 2.7 \times 10^{18} \text{ cm}^{-3}$	55
Figure 3-1.	The experimental setup.	65
Figure 3-2.	Photo of experimental setup.....	66
Figure 3-3.	False-color images of electron beam energy spectrum at different electron densities.....	69
Figure 3-4.	False-color images of electron beam energy spectrum at $2.0 \times 10^{19} \text{ cm}^{-3}$..	70
Figure 3-5.	Experimental and analytical prediction of maximum electron energy	71
Figure 3-6.	$\phi(r, \omega)$ at $r=0 \mu\text{ m}$ (left) and $\phi(r, \omega)$ at $r=40 \mu\text{ m}$ (right).	74
Figure 3-7.	Probe pulse focal spot in plasma and in vacuum	75
Figure 3-8.	FDS snapshot and electron spectra.	76
Figure 3-9.	WAKE simulations.	82
Figure 3-10.	VLPL simulations.	83
Figure 3-11.	1-D and 2-D phase unwrapping of the data.	89
Figure 3-12.	Optical bullets outrunning the plasma bubble.....	91
Figure 3-13.	Bubble-shaped structure at $1 \times 10^{19}/\text{cm}^3$	90
Figure 3-14.	Lineout of the bubble feature taken from the line features..	92
Figure 3-15.	Probe pulse amplitude and phase.	93
Figure 3-16.	Probe pulse reconstruction with limited bandwidth 380nm to 420nm. ...	94
Figure 3-17.	The FDS snapshot before the bubble formation ($1.1 \times 10^{19}/\text{cm}^3$).....	95
Figure 3-18.	Typical FDS snapshot with complicated line features.....	96
Figure 3-19.	A typical FDS snapshot showing an optical bullet..	97
Figure 4-1.	Schematic of noncollinear FDH for characterizing longitudinal evolution of a luminal velocity plasma bubble..	105
Figure 4-2.	Simulation of the frequency domain streak camera..	107
Figure 4-3.	Experimental results showing formation of a phase bullet.	108
Figure 4-4.	Simulation of frequency-domain tomography..	109
Figure 4-5.	Preliminary experimental setup of Texas Petawatt LWFA experiment..	110
Figure 4-6.	A design setup of the probe pulse intersecting the gas cell.....	111
Figure 5-1.	Schematic layout of BNL-ATF experiment.....	111
Figure 5-2.	WAKE simulations showing plasma wake generated in a preformed plasma channel..	111

List of Tables

Table 1-1: Comparison light intensities from various sources.	12
Table 3-1: Comparison of experimental parameters: 2006 experiment versus 2009 experiment.....	63

Chapter 1. Introduction to Laser-Plasma Particle Acceleration

Particle accelerators are used to probe nature's deepest subatomic secrets [1], to irradiate cancerous tumors [2], and to produce bright X-rays that reveal the structure of molecules essential to life [3]. They have also become the largest and most expensive of scientific instruments [4]. Thirty years ago, theoretical physicists John Dawson and Toshiki Tajima proposed an idea for making particle accelerators thousands of times smaller. In their approach, particles surf on electron density waves driven by short intense laser pulses propagating through a plasma, or ionized gas [5]. In such a laser-plasma accelerator (LPA), the laser pulse propagates through the plasma making electron density waves in its wake just as a boat generates water waves as it passes through a lake. A charged particle accelerates by surfing the density wave from crest to trough before it exits the accelerator. Since much steeper accelerating gradients can be built up within such waves than in conventional accelerators, particles can accelerate much faster, so that accelerators can be much smaller. Early prototypes of LPAs, however, produced poor-quality beams with a wide spread of particle energies and directions [6-11].

In a 2004 breakthrough, experimental physicists showed that LPAs could produce high-quality, monoenergetic, collimated beams of electrons just like those in conventional accelerators [12-14]. By 2006, an LPA only 1 inch long produced monoenergetic electrons with energies as high as 1 gigaelectron volt (1 GeV) — about 3% of the energy of electrons produced by the 2-mile-long Stanford Linear Accelerator (SLAC) [15]. More recently, several groups have demonstrated GeV-range LPAs and improved their operation in various ways [16-21]. In all cases, the secret was for the

laser to produce a “bubble” almost completely devoid of electrons in its immediate wake. The bubble captured electrons from the surrounding plasma and accelerated them in an exceptionally uniform way [22]. Recent theoretical work has explained how the bubble captures the electrons and accelerates them so uniformly, thus solving one of the outstanding mysteries of this field [23].

This thesis describes the first direct laboratory visualization of laser-driven electron density bubbles which have transformed laser-plasma acceleration from a fringe discipline into serious accelerator science. Prior to the work described in this thesis, intensive computer simulations were the only source of detailed knowledge of the formation, structure, and dynamics of plasma bubbles. In modeling experiments, such simulations rely on estimates of initial conditions. Because the laser-plasma interaction that forms bubbles depends nonlinearly on laser intensity, however, the bubble’s structure and dynamics, and the bubble accelerator’s operating characteristics, can become sensitive to small, uncontrolled variations in the initial conditions.

The importance of single-shot laboratory visualization is to provide an immediate detailed view of the plasma bubble that can be related directly to the properties of the accelerated electrons. Such visualization helps us understand how bubbles form and then capture and accelerate electrons under various conditions. For example, experiments described in Chapter 3 show for the first time that bubbles sometimes form without capturing or accelerating any electrons at all. Under other conditions, the bubbles produce polyenergetic electrons, and under still other conditions they produce monoenergetic electrons, which are more desirable for most applications. Thus, direct laboratory visualization helps us understand why LPAs sometimes work poorly and sometimes work very well. In addition, visualization helps us design better LPAs that

can accelerate particles to higher energies while maintaining excellent beam quality. To appreciate the importance of direct laboratory visualization, it may help to imagine an engineer trying to design, build, and operate a conventional accelerator while wearing blindfolds. Seeing the accelerating structure directly is an essential part of the enterprise of accelerating particles.

This chapter introduces the main concepts of laser-plasma particle acceleration. I will first survey conventional radio-frequency (rf) accelerators, their applications, their various types, and their limitations. I will then briefly describe ideas being pursued by some researchers to accelerate charged particles directly with laser fields. This approach is difficult because laser fields are transverse and oscillatory, and thus do not easily accelerate particles rectilinearly. I will then devote the bulk of this chapter to laser-plasma accelerators, in which plasma mediates between an intense laser pulse and the accelerating particles. The plasma converts the laser's transverse oscillatory field into a longitudinal electrostatic field that accelerates the particle continuously in one direction.

This thesis is mainly concerned with electron LPAs that use underdense plasma, that is, plasma for which the electron plasma frequency $\omega_p = n_e e^2 / \epsilon_0 m$ is less than the frequency ω of the driving laser pulse. However, an entire parallel subfield of LPA is devoted to a type of LPA that uses overdense plasma ($\omega_p > \omega$) and usually a solid target. This subfield shows promise for a compact acceleration of protons and ions [24]. I will not discuss these overdense plasma accelerators except to point out briefly some parallels with underdense LPAs. Most overdense LPAs to date have been based on so-called Target Normal Sheath Acceleration (TNSA): electrons in the target are intensely heated by a relativistically intense laser pulse, which separates the electrons from the ion background to create a strong space-charge field that ionizes and accelerates hydrogen

and other impurities on the target surface along the target normal. In this respect, overdense LPAs are analogous to laser wakefield accelerators in underdense plasmas (discussed in Sec. 1.3), except that the charge separation is driven by heating instead of the laser's ponderomotive force (discussed in Sec. 1.3.2), and the space charge field reaches $\sim 10^{12}$ V/m compared to $\sim 10^{10}$ V/m in underdense LPAs albeit over a shorter scale length, $\lambda_{\text{Debye}} \approx 10^{-6}$ m compared to ~ 1 cm for underdense LPAs [25]. Protons have been accelerated to as much as 60 MeV by TNSA [26]. Recently, ~ 100 MeV positron beams (created by an electron-gamma shower in the solid target) were generated by TNSA [27]. More recently, computer simulations have shown that relativistically intense circularly-polarized laser pulses of ultrahigh peak-to-pedestal contrast can accelerate protons to even higher energy (~ 500 MeV) by Radiation Pressure Acceleration (RPA) [28]. IN RPA, electrons are separated from solid density ions directly by the ponderomotive pressure of the laser pulse, in close analogy to laser wakefield accelerators in underdense plasma. The incentive that drives researchers in RPA is that it could provide a very compact source of protons of ~ 200 MeV energy, which is useful for therapy on deep cancers, such as brain tumors. To date, however, neither RPA nor laser-accelerated protons of energy exceeding ~ 60 MeV have been demonstrated in the laboratory.

1.1. CONVENTIONAL PARTICLE ACCELERATORS

The applications, categories and limitations of conventional particle accelerators are discussed in this section.

1.1.1. Applications

Particle accelerators are manmade devices that generate fast-moving charged particles. The cathode ray tube (CRT) inside a CRT TV is a kind of particle accelerator. The large hadron collider (LHC), the world's largest particle accelerator, lies in a tunnel 17 miles in circumference and 574 feet beneath the earth. Accelerators are major tools for detecting the properties, internal structure and interactions of atomic and nuclear particles and are widely used in industry, agriculture, and medicine. Their applications include nucleosynthesis, elementary particle physics, low-energy science, and coherent radiation sources.

Ever since Ernest Rutherford bombarded nitrogen with alpha particles from radioactive polonium and successfully transmuted it to oxygen [29], physicists have realized that to probe and alter the atomic nucleus, high-energy particles must be used. However, particles from radioactive material typically have a few MeV, while cosmic rays, though as energetic as 100 TeV, are limited in fluence and hard to control and predict. To have controlled, high-quality, high-energy particles, man has to build accelerators and not rely on natural sources.

Rutherford's successors transmuted nuclei by bombarding them with beams from manmade accelerators. In 1980, Glenn Seaborg, 1951 Nobel Laureate in Chemistry, succeeded in transmuting a minute quantity of lead (possibly via bismuth) into gold using 5 GeV to 28 GeV proton beams at the Lawrence Berkeley Lab (LBL) Bevalac facility

[30]. Particle accelerators are fundamental to synthesizing most elements heavier than uranium as well as thousands of lighter manmade radioactive elements [31].

Particle accelerators were also essential to the discovery of quarks, pions, and leptons and have become the central instrument for high-energy and elementary particle physics. For example, in 1968 deep inelastic scattering experiments at Stanford Linear Accelerator (SLAC) using 7 to 17 GeV electron beams showed that protons consists of smaller, point-like particles unlike any fundamental particles known up to that time [32]. Later, those new particles were confirmed to be quarks. The tau lepton was found in 1975 by Martin Perl (1995 Nobel Prize winner in Physics) when electron and positron collided at the center of a mass energy of 4 GeV in SLAC's then-new e^+e^- colliding ring [33]. Without modern particle accelerators, our understanding of fundamental particles would be still in the Stone Age.

In recent decades, accelerators have been utilized increasingly in low-energy sciences, such as material science, surface science, molecular biology, and chemistry. For instance, accelerators are used in isotope production, oncology, radiation disinfection, nondestructive flaw detection, radiation polymerization, ion injection, ion beam analysis, space radiation simulation, and nuclear explosion simulation. In medical diagnosis and biological studies, from a few to tens of megaelectronvolts of electrons or protons are generated in medical accelerators for nuclear activation to create isotope tracers [34]. Ion beams up to megaelectronvolts from accelerators are used to probe solid surfaces, a

method that is highly sensitive and allows the detection of elements in the sub-monolayer range [35].

Particle accelerators are also used as radiation sources. In the 1940s, when GE build a 70 MeV electron synchrotron (Sec 1.1.2), a technician saw a bright arc of light in the vacuum tube, which was later found to be synchrotron radiation [36]. In the 1950s, synchrotron radiation facilities were called parasitic facilities because the linear accelerators were mainly constructed for particle physics research. Thanks to the usefulness of synchrotron radiation for solid state physics, dedicated storage rings are now built into accelerators for the primary purpose of achieving higher radiation flux and stable operation [37]. In 1974, SLAC built the first multi-GeV storage ring. To increase the brightness of synchrotron radiation, undulators and wigglers were inserted into the electron beam line. The undulator consisted of an array of permanent dipole magnets with alternating polarity, and the electron beams were forced to oscillate in the magnet array. The synchrotron radiation from the different bends in the trajectory interfered, producing a few spectral peaks. Thus, the undulator radiation wa very intense and had a narrow spectrum. The wiggler, however, had higher field and fewer dipoles and could produce a broader spectrum [37].

The latest generation of synchrotron radiation device is called a free electron laser (FEL). This device can produce a fully coherent 100 fs light pulse that has many orders of magnitude greater energy than conventional synchrotron radiation [36]. FELs either in operation or under construction are the world's first X-ray laser, Linac Coherent Light

Source (LCLS) located at the SLAC National Accelerator Center, and the soft X-ray Free-Electron Laser in Hamburg (FLASH) located at Germany's German Electron Synchrotron (DESY). With small wavelength ($\sim 1 \text{ \AA}$), high power (multi-gigawatt), and short duration ($\sim 100 \text{ fs}$), the radiation from FELs can probe many new molecular and atomic processes [38]. Fields like material science and biology will greatly benefit from this amazing light source.

1.1.2. Types of accelerators

The first manmade particle accelerator was an electrostatic accelerator with a constant electric field, that is, a cathode ray tube (CRT). However, CRTs are constrained by electric breakdown to accelerating fields no larger than 100 MV per meter. By applying a time-varying electric field to a bunch of charged particles, radio frequency (RF) accelerators can divide the acceleration process into many stages and synchronize the field of each stage with the accelerating particles. In this way, the particles are accelerated continuously over distances much longer than a typical CRT, enabling the generation of high energy particles despite the limitation of the electric breakdown.

RF accelerators include linacs, where particles propagate in a straight line, cyclotrons where particles orbit in an expanding spiral; and synchrotrons, where particles orbit in a circle. The linac was invented in 1928 by Rolf Widerøe, a Norwegian particle physicist. Currently, the longest linac is SLAC. Inspired by Widerøe, Ernest Lawrence invented the cyclotron, in which an alternating electric field is perpendicular to a constant magnetic field \mathbf{B} . When the electric field oscillates at the cyclotron frequency $\omega_c = e\mathbf{B}/m$

in phase with the circulation of the particles (e is electron charge; m is electron mass), the particles are continuously accelerated in a spiral. The world's largest cyclotron is TRIUMF, Canada's national laboratory for nuclear and particle physics. However, when the particles experience relativistic mass increase at large velocity, they dephase from the oscillating electric field. Consequently, the cyclotron can accelerate particles only to a few percent of light speed. The synchrotron was invented to overcome this limitation. In a synchrotron the frequency of the oscillating electric field is varied to compensate for the mass increase of the particles as they are accelerated. Thus, in a synchrotron, the particles move in a circle. The Large Hadron Collider (LHC) is the world's largest synchrotron; in fact, it is the largest scientific device ever built. The LHC has accelerated protons to 3.5 TeV.

For linacs, the ratio of power radiated to power supplied by the external source is [39]

$$\frac{P}{(dE/dt)} = \frac{2}{3} \frac{e^2}{m^2 c^3} \frac{1}{v} \frac{dE}{dx} \rightarrow \frac{2}{3} \frac{e^2/mc^2}{mc^2} \frac{dE}{dx} \quad (1-1)$$

For the case of SLAC ($dE/dx \sim 10^8$ V/m), the ratio is $\sim 10^{-12}$. For the case of LPAs ($dE/dx \sim 10^{11}$ V/m), the ratio is $\sim 10^{-9}$. We conclude that acceleration loss is unimportant unless the acceleration gradient is greater than 2×10^{20} V/m. For heavier particles the losses are even smaller; thus, radiation losses are negligible in linacs [39]. For the high-energy electron synchrotron, the radiative-energy loss per revolution is $\delta E = \frac{4\pi}{3} \frac{e^2}{\rho} \beta^3 \gamma^4$,

where ρ is the orbit radius. For the high-energy electrons, ($\beta \sim 1$) this has the numerical value

$$\delta E (MeV) = 8.85 \times 10^{-2} \frac{[E(GeV)]^4}{\rho(meters)} \quad (1-2)$$

Therefore, to constrain losses to a few percent, 5-10 GeV is the maximum energy range of kilometer-scale circular electron accelerators [39]. On the other hand, because radiation loss is inversely proportional to the fourth power of particle masses, protons can be accelerated by kilometer-scale synchrotrons with minimal loss.

1.1.3. Fundamental limitation of conventional accelerators

The size of an accelerator ultimately is determined by the maximum voltage applied to the drift tubes. The maximum measured electric field in any manmade accelerator is 200 MV/m [40], as limited by RF breakdown. Any imperfections on the tube multiply the externally applied electric field near the surface. Those strong local fields accelerate electrons out of the tube surface, causing them to hit the surface again and create secondary emission and free ions. This surface plasma dissipates its energy on the surface and creates even more imperfections [41]. To avoid such degradation, fields in most accelerators must be limited to 70 MeV/m. Based on this value, to produce 50 GeV electron beams, the SLAC must be 3 km long, an excellent approximation of its actual length.

1.2. DIRECT LASER ACCELERATION (DLA)

Chirped pulse amplification (CPA) [42] has, for the first time, enabled lasers to produce “relativistic” focused intensities, that is, light intensities that cause free electrons to quiver at relativistic speed. Table 1-1 lists light intensities in W/cm² over a 23-decade range achievable with various sources, both natural and manmade. As discussed below, the corresponding electric field of current lasers can reach several orders of magnitude more than the RF field in conventional accelerators, raising the possibility that such fields applied directly to charged particles in a vacuum might form the basis of extremely compact accelerators.

If we define the normalized vector potential of a linearly polarized laser field as

$$\mathbf{a} = \frac{e\mathbf{A}}{m_e c^2}, \quad (1-3)$$

where \mathbf{A} denotes the usual vector potential defined by the relations $\mathbf{B} = \nabla \times \mathbf{A}$ and $\mathbf{E} = -\partial\mathbf{A}/\partial t$ to the fields \mathbf{B} and \mathbf{E} , then its dimensionless magnitude can be related to peak laser intensity I by [43]

$$a_0 = \left(\frac{2e^2\lambda_0^2 I}{\pi m_e^2 c^5}\right)^{\frac{1}{2}} \cong 0.855 \times 10^{-9} I^{\frac{1}{2}} \left[\frac{\text{W}}{\text{cm}^2}\right] \lambda_0 [\mu\text{m}] \quad (1-4)$$

where I is the laser peak intensity and $\lambda_0 = 2\pi c/\omega_0$ is the laser wavelength with frequency ω_0 . The value of a_0 can be understood as the ratio of the momentum $e\mathbf{A}/c$ gained by an electron in a single oscillation of the laser field to mc , meaning that relativistic effects become important at $a_0 > 1$, or at $I > 10^{18}$ W/cm² for $\lambda_0 \sim 1 \mu\text{m}$ (see Eq. 1-4). The amplitude of the transverse electric field is then

$$E_L [\text{TV/m}] = \frac{m_e c^2 k}{e} a_0 \cong 3.21 \frac{a_0}{\lambda [\mu\text{m}]} \cong 2.7 \times 10^{-9} I^{\frac{1}{2}} [\text{W/cm}^2] \quad (1-5)$$

For example, for $I = 1 \times 10^{19} \text{ W/cm}^2$, Equ. 1-5 gives $E_L = 8.1 \text{ TV/m}$. If we were somehow able to use this field directly, we could accelerate electrons to 8.1 TeV in 1 meter.

Table 1-1: Comparison light intensities from various sources.

Light source	Light intensity [W/cm^2]
Ambient sunlight	0.1
Unfocused cw laser	$\sim 1-10$
At the surface of sun	10^4
Focused cw laser	$\sim 10^8$
Focused Q-switched laser(ns pulse)	$\sim 10^{11}$
Intensity needed to field ionize Helium gas	10^{15}
Intensity at which free electrons quiver at relativistic speed ($\lambda \sim 1 \mu \text{ m}$)	10^{18}
Focused 100 TW 30 fs laser (CPA)	$\sim 10^{19}$
Focused Texas PW 100 fs laser (CPA)	$\sim 10^{19}$
Highest recorded laser intensity[44]	10^{22}

1.2.1. Lorentz equation: Laser-interaction with single particles

An electron responds to both the electric and magnetic fields of a laser pulse. The movement of a single electron is determined by the Lorentz equation [45]:

$$\frac{d\mathbf{p}}{dt} = -e \left(\mathbf{E} + \frac{1}{c} \mathbf{v} \times \mathbf{B} \right) \quad (1-6)$$

where $\mathbf{p} = \gamma m_e \mathbf{v}$, $\mathbf{E} = -\partial \mathbf{A} / \partial ct$, and $\mathbf{B} = \nabla \times \mathbf{A}$.

At $a_0 = \frac{eA}{m_e c^2} \ll 1$, $v/c \ll 1$, and with the $\frac{1}{c} \mathbf{v} \times \mathbf{B}$ term negligible, electrons simply oscillate about their original position. At a mildly relativistic laser intensity ($a_0 > 1$), the electron moves in a figure-eight pattern (see Fig. 1-1) in the plane associated with the laser's polarization and propagation direction [46]. At a highly relativistic intensity, the orbits of electrons become extremely complicated. Because of their sharply curved orbits, radiation losses are enormous, an effect called nonlinear Thomas scattering [9]. Because the fields are oscillatory, the electrons are alternately accelerated and decelerated, rather than accelerated continuously. For that reason, direct acceleration by intense laser fields is unfavorable. One might ask, Is net acceleration of an electron by a laser pulse even possible in principle?

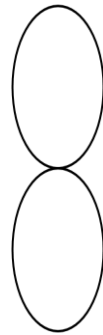


Figure 1-1. Characteristic orbits of free electron in a mildly relativistic linearly polarized laser field in its average rest frame.

1.2.2. Lawson criterion and its limits

In fact, for a laser pulse with a rising leading edge and falling trailing edge, one can show that under certain conditions, electrons will not gain any kinetic energy. They return to their initial state after the laser passes. This behavior is the conclusion of the Lawson-Woodward theorem, which states that the net energy gain of a relativistic electron interacting with an electromagnetic field in vacuum is zero [47]. This theorem assumes that

- (i) The laser field is in vacuum with no walls or boundaries present.
- (ii) The electron is highly relativistic ($v \approx c$) along the acceleration path.
- (iii) No static electric or magnetic fields are present.
- (iv) The region of interaction is infinite.
- (v) Ponderomotive effects (nonlinear forces, $\mathbf{v} \times \mathbf{B}$ force) are neglected.

This last point in principle exempts relativistically intense laser pulses from the Lawson-Woodward theorem. Nevertheless, as discussed above, complicated orbits and high radiation losses obviate the use of intense laser pulses for direct laser acceleration (DLA). Even so, some investigators are working seriously on accelerating electrons directly with nonrelativistically intense lasers. Clearly, direct acceleration by such a laser must violate at least one of the assumptions (i) to (iv) behind the Lawson-Woodward theorem, and usually that is not difficult.

1.2.3. Examples of DLA experiments

Here I will briefly summarize some of the DLA experiments. One recent experiment demonstrated a 30 KeV modulation of a 30 MeV electron beam when it interacted with a 5 TW laser pulse near the surface of an 8 μm -thick gold-coated Kapton tape near focus [48]. This metallic optical element in the focal region of the laser pulse terminates the laser electron interaction. In this way, the deceleration portion of DLA was avoided, and the phase slippage between the electron and laser pulse was minimal over the short interaction near the metal surface. Lawson-Woodward assumptions (i) and (iv) were violated to achieve this. The obvious drawback of this method is that the optics at the focal spot will be damaged at high laser pulse energies.

Other researchers have reduced the phase velocity of the laser pulse to decrease the phase slippage between the laser pulse and electrons by copropagating laser and electrons through gas, thus violating Lawson-Woodward assumption (i). Kimura et al. propagated a 580 MW CO_2 laser pulse and a 40 MeV electron beam through a 12 cm long gas cell and found 3.7 MeV energy modulations on the electron beam [49]. At a higher laser intensity (10^{14} W/cm²), ionization of the gas increased the laser phase velocity, which in turn limited the maximum acceleration gradient for this kind of method. York et al. proposed and demonstrated that a corrugated plasma channel can guide the laser pulse in subluminal phase velocity [50]. DLA will always require an externally injected electron beam. To have a small electron energy spread, the injected electron beam needs to be shorter than a quarter wavelength of the laser pulse. Kimura et al. used an inverse free electron laser (IFEL) to prebunch electron pulses to a 3 fs duration. After

propagating an ~ 100 GW CO₂ laser pulse with a 45 MeV electron beam through a second IFEL, they found an ~ 7 MeV energy gain [51]. In this case, the presence of a static magnetic field in the IFEL wiggler violated Lawson-Woodward assumption (iii). Finally, other researchers showed that DLA can play a major role in LPA experiments which have a low laser pulse energy (1.2 TW) and high plasma density ($\sim 10^{20}/\text{cm}^3$) [52]. In this case, the presence of a plasma and space-charge fields of the wake violate Lawson-Woodward assumptions (i) and (iii), respectively, while the relativistically intense laser field violates assumption (v).

1.2.4. Limitations of direct laser acceleration

There are several reasons that DLA schemes, though feasible in principle, have lagged well behind laser-plasma accelerators (LPA) in actual performance. First, the acceleration direction is not aligned with the laser pulse propagation direction and requires clever and difficult schemes to change it. Second, rapid dephasing of the electron from the acceleration field makes it hard to accelerate electron beams continuously. In DLA, the electrons must be phased within an optical wavelength λ , whereas in LPA the phasing required is on the order of a plasma wavelength λ_p , which is usually much longer. Third, diffraction of the laser pulse limits the acceleration distance. Finally, the need for electron injection, a strong magnetic field, the insertion of a mirror near the laser focus, or a half cycle laser are all technically difficult to implement. LPA avoids most of these difficulties or encounters them in milder forms. Finally, the maximum energy gain of DLA scales as the square root of laser power. Thus DLA is

not efficient when compared with large power LPA, for which maximum energy gain scales linearly with laser power [53].

By using a plasma into which laser energy can be coupled, however, we can generate an electron plasma wave moving in the direction of the laser, whose electric field is parallel to the direction of propagation. The plasma converts the transverse laser field to the axial electric field of the plasma wave. There are several other advantages. First, the phase velocity of the plasma wave is equal to the group velocity of the laser pulse. Thus, the electron can ride on the subluminal plasma wave to a higher velocity with much less phase slippage than in DLA. Second, the ponderomotive force scales inversely with the electron γ factor. The DLA schemes using ponderomotive force is most efficient at low electron energy. For LPA, the ponderomotive force directly works on the low energy plasma electrons and thus is not limited by this scaling. Third, a plasma can prevent laser beam diffraction by several means. One is relativistic self-focusing [54] for $P_{\text{laser}} > 17(\omega_0/\omega_p)^2$ GW, where ω_0 is the laser frequency, $\omega_p = (n_e e^2 / \gamma \epsilon_0 m)^{1/2}$ is the plasma frequency, n_e is the plasma electron density, e is electron charge, and m is electron mass. The focusing is caused by the increase of the dielectric constant $(1 - \omega_p^2 / \omega_0^2)$ near the axis, where the beam is most intense and the electrons have the largest γ factor. Another is by creating a plasma waveguide with lower n_e (and thus a higher dielectric constant) on the axis. Such a waveguide can be preformed by a variety of techniques, including laser-induced cylindrical shocks [55] and capillary discharge [56]. In the case of plasma “bubble” accelerators [22],[57], the main subject

of this thesis, the bubble accelerating structure also forms a natural waveguide that extends the intensities of the drive pulse with the plasma beyond a Rayleigh length [58].

1.3. LASER-PLASMA ELECTRON ACCELERATION (LPA)

After 1979, when Tajima and Dawson published the first theoretical paper on laser-plasma acceleration [5], about 15 years elapsed before experimental activity in the field exploded because of the development of Chirped Pulse Amplification (CPA) [59-61]. CPA lasers provided, for the first time the relativistically intense optical fields needed to drive high amplitude plasma waves. LPA accelerates electrons using the ~ 100 GV/m space-charge electric field propagating inside plasma at merely the speed of light in the wake of a strong laser pulse ($P \geq \sim 10^{18}$ W/cm³). Thirty years later, electron beams with low emittance, relativistic energy, low energy spread, and high stability have been generated in numerous labs around the globe by LPA.

Ten years ago, ~ 100 MeV electron beams with a significant charge (~ 1 nC) were produced and large acceleration gradients (~ 100 GV/m) confirmed [62-68]. However, those electron beams were all born with Maxwellian energy spectrum. In 2004, three groups simultaneously reported the generation of high-quality monoenergetic electron beams (a few mrad divergence, several hundred pC of charge, and a few percent energy spread at a few hundred MeV) [12-14]. Since then, the maximum energy of such high-quality laser-accelerated electron beams has been pushed to ~ 1 GeV [69]. The stability and control of the generated electron beam have also been improved [70-73]. With the maturing of this field, future applications of those high-quality electron beams in fields such as material characterization, nuclear medicine, and high-energy particle physics have come closer to realization [74].

Meanwhile, details of the accelerator structure and the acceleration process have been studied by particle-in-cell (PIC) computer simulations [75-78]. While computer simulations help explain experimental results and guide future experiments, they are also time-consuming, require precise experimental conditions input, and sometimes contradict experimental results. Yet, to know the plasma structure accurately and immediately will help us understand the quality of the electron beam (divergence and energy spread) and to optimize the electron generation on site with a feedback system.

Researchers have searched for an effective *in-situ* method of diagnosing or visualizing the plasma structure behind the laser pulse for many years. An early effort probed the wake at individual points in time using multiple shots [79]. This method was slow and required a stable wakefield to work well. A single-shot scheme, where the entire plasma was illuminated at once utilizing picoseconds-long chirped probe pulses, unmasked the precise temporal and spatial behavior of the plasma wakefields [80]. This method was first demonstrated in the Ph.D. work of my predecessor, Nicholas Matlis (Ph.D, 2006) [81] and has been expanded to the bubble regime in this thesis. Single-shot wake visualization will be discussed in detail in Chapters 2 and 3.

1.3.1. Space charge fields in a perturbed plasma

We can calculate the space charge field that the plasma can sustain using Poisson's equation:

$$\nabla \mathbf{E}_w = -\delta n_e e / \epsilon_0 \quad (1-7)$$

where \mathbf{E}_w is the electrostatic field of the wakefield, δn_e is perturbation of the plasma electron density by the drive-laser pulse, and e is the charge of electron.

Introducing plasma frequency and wave vector,

$$\omega_p = \sqrt{\frac{n_e e^2}{\epsilon_0 m_e}} \text{ and } k = \frac{\omega_p}{c} \quad (1-8)$$

We assume for simplicity a one-dimensional sinusoidal wakefield $\mathbf{E}_w = \hat{z} E_0 \sin(k_p z - \omega_p t + \phi)$ and density perturbation $\delta n_e = \delta n_{e0} \cos(k_p z - \omega_p t + \phi)$, where ϕ is a phase factor. To estimate the maximum electrostatic wakefield E_0^{max} , we can approximate the maximum density perturbation that the plasma can sustain to be $\delta n_{e0}^{max} \approx n_e$. We then find that the maximum electric field is

$$E_0^{max} = m c \omega_p \frac{1}{\epsilon_0} \approx 96 \sqrt{m' 0 / ^{07} \text{bl}^{-2}} \text{ (F.U.1)} \quad (1-9)$$

This value is called the cold nonrelativistic wave breaking field. For $n_e = 10^{18}/\text{cm}^3$, the electric field will be ~ 100 GV/m, which is more than 3 orders of magnitude higher than the fields SLAC can maintain.

1.3.2. Ponderomotive force: Creation of a Langmuir wave

The drive laser exerts a Lorentz force on plasma electrons:

$$\frac{d\mathbf{p}}{dt} = -e \left(\mathbf{E} + \frac{1}{c} \mathbf{v} \times \mathbf{B} \right) \quad (1-6)$$

Introducing the vector potential \mathbf{A} and treating plasma electrons as a fluid, this becomes: $\frac{d\mathbf{p}}{dt} = -e \left(\mathbf{E} + \frac{1}{c} \mathbf{v} \times \mathbf{B} \right)$ (1-6)

$$\frac{\partial \mathbf{p}}{\partial t} + (\mathbf{v} \cdot \nabla) \mathbf{p} = \frac{e}{c} \frac{\partial \mathbf{A}}{\partial t} - \frac{e}{c} \mathbf{v} \times \nabla \times \mathbf{A} \quad (1-10)$$

where the second term on the left describes convection. We can separate \mathbf{p} into slow and fast time scales \mathbf{p}^s and \mathbf{p}^f , where the fast part is the transverse oscillatory motion of the electrons in the laser field $\mathbf{p}^f = e\mathbf{A}/mc$ and the slow part is the electron fluid response to

the cycle averaged laser pulse. Averaging over a laser cycle, we have the ponderomotive force [82],[83]:

$$\mathbf{F}_p = \frac{d\mathbf{p}^s}{dt} = -m_e c^2 \nabla \bar{\gamma} \quad (1-11)$$

where $\gamma = (1 + \frac{v_s^2}{m^2 c^2} + \frac{a_0^2}{2})^{\frac{1}{2}}$ (the bar means the averaging of a laser cycle). Physically, the ponderomotive force will tend to push electrons out of regions of locally higher intensity.

When the laser passes through a neutral gas, the pulse front ionizes the gas and creates a plasma. The ponderomotive force of the laser pulse then pushes the electrons away from the high laser intensity region. On a fast time scale the ions remain nearly stationary because of their large mass. The resulting charge displacement provides an electrostatic restoring force that causes the plasma electrons to oscillate at the plasma frequency after the laser pulse passes by them, creating alternating regions of net positive and net negative charge—the so-called Langmuir wave. The resulting electrostatic wakefield plasma wave propagates at a phase velocity nearly equal to the speed of light and thus can continuously accelerate properly phased electrons.

The plasma wave generated in uniform plasma for $a_0 \ll 1$ is governed by a force oscillator equation [84]:

$$(\partial^2 / \partial t^2 + \omega_p^2) \delta n_e / n_{e0} = c^2 \nabla^2 a^2 / 2 \quad (1-12)$$

where $\delta n_e/n_{e0} = n_e/n_{e0} - 1$ is the normalized density perturbation. The solution of the equation above for $\delta n_e/n_{e0} \ll 1$ is [84]

$$\delta n/n_0 = (c^2/\omega_p) \int_0^t dt' \sin[\omega_p(t-t')] \nabla^2 a^2(r, t')/2 \quad (1-13)$$

The plasma wave in the linear regime ($\delta n/n_0 \ll 1$) is a sinusoidal-shaped wave with plasma frequency ω_p and phase velocity $v_p = v_g$, where v_g is the group velocity of the laser pulse. As a_0 exceeds 1, relativistic effects become important, and we need to consider nonlinear terms in powers of a_0^2 [85],[86]. A fully nonlinear model needs to be considered for even larger a_0 . In the nonlinear regime, the peaks of the plasma wave become squeezed and rise sharply. The electric field also transforms from a sinusoidal shape to a saw-toothed shape. More interesting, the period of the plasma wave increases as a_0 increases.

$$\begin{aligned} \lambda_{Np} &= \lambda_p(1 + 3(E_{max}/E_0)^2/16), \quad \text{for} \quad E_{max}/E_0 \ll 1 \\ \lambda_{Np} &= \lambda_p(2/\pi)(E_{max}/E_0 + E_0/E_{max}), \quad \text{for} \quad E_{max}/E_0 \gg 1 \end{aligned} \quad (1-14)$$

where E_{max} is the peak electric field of the plasma wave and E_0 is defined in Eq. (1-9). For a square laser pulse with $\tau_p \approx \pi/\omega_p$ [85],[86],

$$E_{max}/E_0 = (a_0^2/2)(1 + a_0^2/2)^{-1/2} \quad (1-15)$$

For $a_0 = 3$, the plasma wavelength almost doubles. This increase in wavelength introduces an interesting effect to the plasma wave driven by a relativistically intense laser pulse. The laser pulse drives the plasma wave harder on its propagation axis ($r = 0$) than in its wings ($r > w_0$), or the edge of the pulse. As a result, the plasma wave curves

backwards into a parabolic shape. This effect was observed in experiments [80] and in 2-D particle simulations [87],[88].

1.3.3. Types of laser-plasma electron accelerators

Here five types of laser driven plasma electron accelerators are reviewed: LWFA, PBWA, self-modulated LWFA, Raman-beam seeded accelerator and plasma bubble accelerator.

1.3.3.1. *Resonantly-driven linear plasma waves: LWFA*

When a laser pulse enters a plasma, the ponderomotive force at its leading edge pushes electrons forward, leaving heavier ions behind. After the peak of the laser pulse passes, the ponderomotive force changes sign and pushes electrons backwards. Thus the plasma wave is generated most efficiently when the laser pulse duration is matched to the plasma period ($\tau_p \approx \pi/\omega_p$), so that these ponderomotive pushes act in phase with the electrostatic restoring forces. An engineering equation for the matched pulse duration τ_{fwhm} is

$$\tau_{\text{fwhm}}[\text{fs}] \approx 50n_{18}^{-\frac{1}{2}} \quad (1-16)$$

where n_{18} denotes the plasma electron density in units of 10^{18} cm^{-3} . Amiranoff et al. focused a laser of 400 fs, 1.5 J, and 1 $\mu\text{ m}$ to a maximum intensity of $4 \times 10^{17} \text{ W/cm}^2$ in a plasma with resonant density $2.2 \times 10^{16} \text{ cm}^{-3}$. They observed LWFA accelerated electrons with an energy gain of 1.6 MeV (3 MeV injected). The peak longitudinal electric field was estimated to be 1.5 GV/m [89].

1.3.3.2. *Plasma Beat-Wave Accelerator (PBWA)*

In the early days of this field, femtosecond pulsed lasers were unavailable, and therefore the matched condition could not be realized in plasmas of density $n_e > 10^{14}$ cm^{-3} , at which a > 0.01 GV/m acceleration field was achievable (see Equ. 1-9). Hence, a popular alternative approach was to use two copropagating long ($\tau_p \gg \pi/\omega_p$) laser pulses with slightly different frequencies and wave numbers. The two laser pulses then resonantly excited plasma waves if their beat frequency equaled the plasma frequency [90]. A laser intensity of $a_0 = 0.1$ and laser pulse duration of 100 ps were sufficient to generate a large-amplitude plasma wave because of the resonant and repetitive nature of the beat wave excitation. In this regime, however, surrounding plasma electrons were not trapped inside the wakefield and had to be injected from an outside source, such as a linac [91]. The energy gain ΔE was modest at several tens of MeV, and the energy spectrum had a wide spread.

1.3.3.3. *Far-off-resonantly-driven plasma waves: Self-modulated LWFA*

With the invention of chirped pulse amplification (CPA), subpicoseconds (~ 100 fs) laser pulses of a few terawatts peak power became available for laser-plasma acceleration. As discussed above, resonant LWFA experiments proved difficult because of the requirements of external injection and low energy gain. Researchers soon discovered, however, that 100 fs, terawatt laser pulses yielded copious relativistic electrons when they excited plasmas far denser than the matched resonant condition ($\omega_p \tau_{\text{fwhm}} \gg \pi$). Under those conditions, the relatively long drive pulses split into several shorter laser pulses, each with a duration equal to π/ω_p . A large-amplitude plasma wave was generated in the process because of a parametric instability known as forward Raman scattering [91]. Because this acceleration occurs at higher plasma densities, the

E field of the plasma wave is higher than for a resonantly driven LWFA. The higher laser intensity requirement ($P > P_{\text{crit}}$) ensures relativistic laser pulse guiding and higher a_0 than at the plasma entrance. As the electrons were trapped and accelerated in different plasma periods with random phases, the electron spectrum was normally Maxwellian. The presence of the plasma wave was detected by measuring the Stokes and anti-Stokes peaks in the pump pulse spectrum, or, for time-resolved measurements, in the spectral of a co-propagating probe pulse [92]. Accelerated electron bunches typically contained a charge order of pC, with an ~ 100 MeV energy gain, and they were highly collimated. During this time, relativistic self-focusing was found to guide the laser pulse to propagate beyond the Rayleigh range and extend the acceleration length of the laser until its energy was depleted [93].

1.3.3.4. Raman beam seeded acceleration

Self-modulated acceleration depends on noise or fluctuation as the trigger of the plasma wave generation. When a Raman-shifted laser pulse ($\omega = \omega_0 - \omega_p$) is introduced into plasma with the driver pulse, the power requirement for the driver pulse is lowered. In fact, the driving laser pulse energy can be reduced by a factor of ten times or more, thus enabling high repetition rates (kHz) and new applications [94].

1.3.3.5. Resonantly driven, strongly nonlinear, broken plasma waves: Bubble regime

At high enough laser intensity ($\sim 10^{19}$ W/cm²), the radial ponderomotive force of the laser pulse completely evacuates electrons from its immediate environment and forms an ion cavity [22]. In the meantime, the E field of the laser accelerates electrons transversely, as in DLA (see Sec. 1.2). As electrons leave the high-intensity region, the

positive coulomb force generated by the evacuated region will pull them back. Those electrons then go around the evacuated region and form a thin sheath around it. Finally the electrons will come to the back side of the blow out region and some of the electrons will get injected into the bubble region. As electrons are accelerated to high velocities, the laser loses energy and etches away. The bubble also grows bigger as it traps more and more electrons. This process efficiently stops the electron loading into the bubble and ensures a small energy spread. The bubble also has a transverse field that helps focus the electron beams [95],[57].

The following is an elementary example of a uniformly charged sphere that illustrates the basic structure of the bubble's internal fields in cylindrical coordinates:

$$\mathbf{E}_{bubble} = \frac{en_e}{3\epsilon_0} (z\hat{z} + r\hat{r}) \quad (1-17)$$

where $r = z = 0$ is the bubble's center. Hence, there is an accelerating (decelerating) field for electrons at $z < 0$ ($z > 0$). $\mathbf{E}_{bubble}(z)$ is independent of r , which facilitates monoenergy acceleration if the electron is injected at a fixed z . $\mathbf{E}_{bubble}(r)$ helps focus the electron bunches.

Today, most laser-driven plasma acceleration experiments are performed in this regime, including the experiment that produced the record 1 GeV electron beam [69]. Self-injection of background plasma electrons into the quasistatic plasma bubble can be caused by the slow temporal expansion of the bubble. The combination of the bubble's expansion and contraction results in monoenergetic electron beams [23].

1.3.4. Limitations to acceleration length

To accelerate electrons to high energy, the acceleration must be maintained over as long a distance as possible. For LPAs, there are three main physical limits to acceleration length. An understanding of how these limits scale with laser and plasma parameters is essential to optimizing LPA performance. We discuss each limit in turn.

1.3.4.1. Diffraction length

To achieve high-amplitude plasma waves with $E_{\max}/E_0 \geq 1$, the drive-laser pulse must be focused to relativistic intensity $a_0 \geq 1$ (see Equ. 1-15), or $I \geq 10^{18}$ W/cm² for $\lambda = 1 \mu\text{ m}$ (see Equ. 1-4). For Gaussian spatial and temporal profiles, I is related to the e^{-1} duration τ and spot size w_0 of a pulse of energy E_p by [96]:

$$I = \frac{2E_p}{\tau\pi w_0^2} \quad (1-18)$$

Thus, to achieve large I , small w_0 is required. This in turn implies a small Rayleigh length

$$Z_R = \pi w_0^2 / \lambda \quad (1-19)$$

defined as the distance from the focus ($z=0$) of a Gaussian beam to the point on its propagation axis at which its intensity drops by a factor of 2 (or, equivalently, waist $w(z) = \sqrt{2}w_0$). Thus, for a pulse of fixed E_p and τ , the acceleration length

$$L \approx 2Z_R = \frac{4E_p}{\lambda\tau I} \quad (1-20)$$

scales inversely with peak intensity I in the absence of a guiding mechanism. As a numerical example, many of the experiments in this thesis were performed with pulses of $E_p \approx 1$ J, $\lambda = 0.8 \mu\text{ m}$, and $\tau \approx 30$ fs, yielding

$$L[cm] = \frac{1.67}{I[10^{18}W/cm^2]} \quad (1-21)$$

For a mildly relativistic intensity ($I \approx 10^{18} \text{ W/cm}^2$) appropriate for weakly nonlinear laser-plasma interaction, $L \approx 1.67 \text{ cm}$; for strongly relativistic intensity ($I \approx 10^{19} \text{ W/cm}^2$), required for nonlinear bubble regime acceleration, $L \approx 0.17 \text{ cm}$. Those estimates assume there is no guiding mechanism.

In order to exceed this diffraction limit, the laser pulse needs to be guided. When the index of refraction $\eta(r)$ has a maximum on the axis, that is, $\partial\eta/\partial r < 0$, the phase velocity on the axis will be slower than it would be off the axis. The laser pulse focuses on the axis and guiding becomes possible.

The general expression for the index of refraction of a strongly underdense ($\omega \gg \omega_p$), cylindrically symmetric plasma wave is [97],[85],[86]

$$\eta_r(r) \approx 1 - \frac{\omega_{p0}^2}{2\omega^2} \frac{n_e(r)}{n_{e0}\gamma(r)} \quad (1-22)$$

where ω_{p0} and n_{e0} denote the plasma frequency and electron density, respectively, at $r = 0$, and $n_e(r)$ denotes the charge in electron density with r . $\gamma(r)$ increases with laser intensity, so that a Gaussian laser pulse that has high intensity on the axis will cause relativistic self-focusing and guiding when the laser power exceeds a critical power P_c [98]:

$$P_c(GW) \approx 17.4(\omega/\omega_{p0})^2 \quad (1-23)$$

Numerous experiments have observed relativistic self-focusing in which the laser pulses are guided for a few tens of Rayleigh lengths [99],[100].

From Equ. (1-16), a second way to guide the laser pulse is to introduce an

electron density minimum on the axis. Under some circumstances, that is, the bubble regime — the drive-laser pulse itself forms such an axial minimum by pushing plasma electrons radially outward from within the pulse envelope via the ponderomotive force (see Equ. 1-11). In this case, the plasma channel guiding supplements relativistic self-focusing. Under other circumstances, the plasma channel can be preformed. Several methods have been developed for doing this. In one method, a long (~ 100 ps) laser pulse is focused to a line using an axicon or cylindrical lens, where it ionizes and heats the plasma. The resulting radially expanding plasma shock wave then produces a plasma channel [101-105]. Capillary discharges can also produce a plasma channel through Z – pinch [106], laser ablation [107],[108], and heating [109].

1.3.4.2. *Dephasing length*

Electrons interacting with a wakefield can experience either accelerating fields or decelerating fields, depending on their location within the wave. If electrons do not have a large enough initial velocity, they slip through the plasma and never become trapped by the wave. The minimum velocity for an electron to be trapped by a quasistatic plasma wave can be calculated [110] as

$$v_{min} = -c(1 - \gamma_{min}^{-2})^{1/2}$$

$$\gamma_{min} = \gamma_p(1 + \gamma_p X) - \gamma_p \beta_p [(1 + \gamma_p X)^2 - 1]^{1/2} \quad (1-24)$$

where $\gamma_p = (1 - \beta_p^2)^{-\frac{1}{2}}$, $\beta_p = v_p/c$, v_p is plasma phase velocity, $X = 2\beta_p[(1 + (E_{max}/E_0)^2/2)^2]^{1/2}$. If electrons are fast enough, they accelerate and propagate together with the wave. After electrons acquire velocities larger than the wakefield

phase velocity, however, they outrun the plasma wave and drift into the deceleration region. The distance over which this dephasing occurs is called the dephasing length L_d , and restricts the maximum energy gain to approximately eE_0L_d , where E_0 is the cold nonrelativistic wave-breaking field (see Equ. 1-9). For a sinusoidal plasma wave, acceleration will cease once the electrons phase advance a distance of $(v_e - v_p)t = \lambda_p/2$ with respect to the plasma wave. In the laboratory frame, this distance corresponds to

$$L_d = c\lambda_p/2(c - v_p) \approx \frac{\lambda_p^3}{\lambda^2} \quad (1-25)$$

where v_p denotes the phase velocity of the plasma wave, which is equal to the group velocity v_g of the laser pulse given by [45]

$$v_g = c(1 - \omega_p^2/\omega^2)^{\frac{1}{2}} \quad (1-26)$$

in the linear regime [45]. Approximating $\lambda_p \approx c/\omega_p$ (see Equ. 1-14), we can rewrite Equ. 1-25 as an engineering formula:

$$L_d[cm] = 0.1(n_e[10^{19}cm^{-3}])^{-\frac{3}{2}} \times (\lambda[\mu m])^{-2} \quad (1-27)$$

As a numerical example, the experiments in this thesis were performed with pulses of $\lambda = 0.8 \mu m$ in a plasma of density $10^{19} \leq n_e \leq 3 \times 10^{19} cm^{-3}$, yielding $L_d \approx 0.16 cm$ for $n_e = 1 \times 10^{19} cm^{-3}$ and $L_d \approx 0.03 cm$ for $n_e = 3 \times 10^{19} cm^{-3}$. Both numbers are much smaller than the diffraction length noted above.

While the above analysis gives an adequate rough estimate of L_d , the group velocity of the laser pulse can decrease from that in Equ. 1-25 for several reasons. (1) The laser pulse red-shifts after passing through a time varying index of refraction induced

by the plasma oscillation. The red-shifting causes the laser pulse to slow down [111]. (2) When the laser drives plasma in the bubble regime, the front of the laser spikes up and converts energy into the local plasma electrons. This action causes local pump depletion and erodes the laser front. (3) When the laser pulse is focused tightly, the group velocity is reduced due to the geometric effect [112].

1.3.4.3. Depletion length

As the laser pulse drives the plasma wave, the front of the laser etches back due to local pump depletion. This etching velocity is estimated by using a 1-D nonlinear equation to be [113]

$$v_{etch} \cong c \times \omega_p^2 / \omega_0^2 \quad (1-28)$$

Therefore, the pump depletion length will be

$$L_{depletion} = \frac{c}{v_{etch}} c\tau_{FWHM} = c\tau_{FWHM} \lambda_p^2 / \lambda_0^2 \quad (1-29)$$

where τ_{FWHM} is the laser pulse duration. We can rewrite it as engineering formula:

$$L_{depletion} = 100c\tau_{FWHM} (\lambda_0 [\mu m])^{-2} (n_e [10^{19} cm^{-3}])^{-1} \quad (1-30)$$

As a numerical example, the experiments in this thesis were performed with pulses of $\lambda = 0.8 \mu m$ and $\tau_{FWHM} \approx 30 fs$ in a plasma of density $10^{19} \leq n_e \leq 3 \times 10^{19} cm^{-3}$, yielding $L_{depletion} \approx 1.4 mm$ for $n_e = 1 \times 10^{19} cm^{-3}$ and $L_{depletion} \approx 0.35 mm$ for $n_e = 3 \times 10^{19} cm^{-3}$.

1.3.5. Emerging applications of monoenergetic laser-plasma electron accelerators

The stable generation of monoenergetic, ultra-short, and collimated relativistic electron bunches from laser plasma accelerators is opening up new applications in many fields. These new applications arise from two new, unique features of monoenergetic LPAs. First, they are thousands of times smaller and cheaper than conventional electron accelerators. These advantages make them more convenient for many applications. Second, they produce electron bunches thousands of times shorter (~ 1 fs) than conventional accelerators and thus proportionally larger peak currents for a given bunch charges. Consequently, they are more efficient as radiation sources over a wide spectral range (THz to γ -rays) than conventional accelerators.

Indeed, Nakajima [114] has argued that existing GeV class LPAs have the potential to rival large-scale X-ray FELS, such as the SLAC Linac Coherent Light Source (LCLS) and Deutsches Elektronen-Synchrotron (DESY) in peak X-ray brilliance, potentially putting FELS in every major research university in the world. Leemans *et al.* [115] demonstrated a compact source of coherent THz radiation based on transition radiation at a vacuum-plasma boundary from laser wakefield generated electron beams. With a millimeter transverse scale plasma sheet at the exit of the accelerator, this compact source could produce in excess of $100 \mu\text{ J/pulse}$, which is more than two orders of magnitude higher than those for present sources. Pai *et al.* [116] demonstrated the production of intense infrared pulses with $250\text{-}\mu\text{ J}$ pulse energy from a laser wakefield accelerator. The pulse energy, comparable to that of the most intense free-electron lasers, is strongly correlated with the production of self-injected monoenergetic electron beam. Synchrotron radiation generated using an electron beam from LPAs also makes it

possible to build an X-ray free-electron laser hundreds of times smaller than the LCLS and DESY [117]. Schlenvoigt *et al.* [118] demonstrated the first successful combination of a laser-plasma wakefield accelerator, which produced 55–75 MeV electron bunches, with an undulator to generate visible synchrotron radiation. This result showed the potential for ultracompact and versatile laser-based radiation sources from the infrared to X-ray energies.

1.3.6. How far can laser-plasma electron accelerators go?

Not satisfied with a mere 1 GeV electron beam [69], researchers are already investigating different approaches to reach energies beyond. One approach is to do it all in one stage in the nonlinear bubble regime. A lower n_e is required to extend the dephasing length L_d (see Sec. 1.3.4.2). Higher laser power is also required. Lu *et al.* [95] suggested that a 30 fs, 200 TW laser could produce an ultrashort (10fs), monoenergetic (1.5 GeV), and self-injected electron bunch in a single stage after propagating through a 0.75 cm long plasma with a density of $1.5 \times 10^{18} \text{ cm}^{-3}$. Kalmykov *et al.* [119] showed that a self-injected, self-guided, bubble regime LPA driven by 1 PW pulses can reach ~ 10 GeV in $n_e \sim 10^{17} \text{ cm}^{-3}$ with plasma of length $L \sim 10$ cm. To reach even higher energy (100 GeV), even lower n_e will be required. Using Equ. 1-9 and Equ. 1-26, we can roughly estimate the maximum electron energy achievable. To reach 100 GeV, the plasma density needs to be $4 \times 10^{16} \text{ cm}^{-3}$. However, self-injection and self-guiding are probably no longer possible at such low n_e . Thus, external injection will be necessary (for example, controlled electron injection can be induced by colliding laser

pulses [120]). Meter-scale (0.1 m ~ 1 m), low-density plasma channels for guiding also need to be developed.

The other approach to reaching higher electron energy is to use multiple stages. Leemans *et al.* [121] envisioned to build a much shorter and cheaper LPA-based TeV electron–positron collider by coupling many acceleration stages. A TeV linac would have about 100 10-GeV modular accelerating stages. Each stage would consist of a preformed plasma channel with a plasma electron density of about 10^{17} cm^{-3} . In each stage, electrons would be accelerated by a 30 J, 100 fs laser pulse in a mildly nonlinear plasma wave. In this case, the difficulty of phasing subsequent stages must be addressed. So far, very little work has been done on this approach except for the inverse FEL experiments of Kimura *et al.* [122],[123].

Chapter 2. Visualization of Laser Wakefields in Tenuous Plasma: Frequency-Domain Holography

In this chapter, I will first discuss the importance of imaging plasma structure in LPAs. Frequency Domain Holography (FDH), a technique for imaging objects moving at the speed of light, enables reconstruction of quasi-static structures in tenuous, non-refraction plasma from the phase modulation they imprint on a co-propagating probe pulse. I will describe the theory, setup and analysis of FDH experiments in tenuous plasma. Much of the description closely follows Dr. Matlis' description in his 2006 paper [80] and dissertation [81]. However, I will also describe some of my new analysis of Matlis' results and of artifacts that can creep into reconstructed FDH images that were not included in the 2006 documents. FDH methodology closely precedes Frequency Domain Shadowgraphy (FDS), a technique for reconstructing light-velocity objects in dense, refractive plasma from the amplitude modulation they imprint on a co-propagating probe pulse. My FDS results will be presented in Chapter 3. A comprehensive description of both FDH and FDS was presented in my 2010 paper [124], on which most the present chapter is based.

2.1. WHY WE NEED TO SEE LASER WAKEFIELDS DIRECTLY.

Recent LWFA experiments are performed either in the forced laser wakefield regime or the bubble regime, in which the laser-plasma interaction is highly nonlinear. As a result, the electron spectrum and the plasma accelerator structure are very sensitive to initial conditions, such as the laser pulse profile, pulse duration, gas jet profile, gas

composition, etc. Under these conditions, computer simulation of the acceleration process normally takes days on leading-edge computers and consumes tens of MW electrical power. Thus real time observation of the plasma density distribution and optimization of the electron beam by computer simulation alone is out of the question. The simulation also needs detailed input from the real experiment on the volatile initial conditions mentioned above. In the highly nonlinear regime, a small measurement error is likely to cause a false simulation result. Direct visualization of the plasma structure provides an earlier point of contact for theory and experiment than calculations and measurements of accelerated electrons. *In-situ* visualization also helps theoreticians to benchmark simulation codes, provides immediate feedback on electron generation and in the process will teach us to optimize laser plasma accelerators.

2.2. WHY IT IS DIFFICULT TO VISUALIZE LASER WAKEFIELDS.

Wakefields are difficult to visualize in the laboratory because they move at the speed of light in the plasma and are about the same transverse size as the laser focal spot--typically tens of micrometers. Thus we not only need microscope optics to magnify them, we must also slow down their effective luminal velocity in the lab frame by visualizing them in their moving reference frame. The index of refraction of the plasma is also close to 1, so the wakefield has low optical contrast. A wakefield can be longer than ~ 1 ps, yet to resolve the periods, one needs a resolution of tens of femtoseconds. To make things even worse, pump laser pulses and gas jets usually fluctuate from shot to shot, which makes a single shot measurement essential.

2.3. PREVIOUS METHODS FOR CHARACTERIZING LASER WAKEFIELDS IN TENUOUS PLASMA

To measure something moving very fast, we need to ride along with it. Copropagating a probe pulse with the plasma wave is like riding along a train. The phase of the probe is modulated by the plasma wave in proportion to the plasma's local index of refraction, which depends on its local electron density. This probe pulse phase $\phi(t)$ will cause the centroid of the probe pulse spectrum to shift if $\phi(t)$ is mainly linear in time ($\phi = \phi_0 + \phi_1 t$). This is so-called photon acceleration [125]. By measuring the centroid shift, ϕ_1 is obtained. Though experimentally simple, this method only obtains part of the phase information and is quite sensitive to background noise such as pump light leakage. It is also not much help when the centroid shift is less than the spectral bandwidth of the probe pulse, as is usually the case for plasma waves in the tenuous plasma.

Rosenzweig *et al.* used a low-density 15-MeV witness electron pulse with a variable delay time behind an intense electron drive bunch to probe the wakefield [126]. The probe electron beam experienced the accelerating or deceleration of the wake field depending on the delay. By mapping out the delays and energy centroid changes, the period of the wakefield was experimentally measured. This worked well for probing the longitudinal structure of electron bunch-driven wakes, but is impractical for laser-driven wakes because a source of relativistic witness electron pulses synchronized with the drive laser pulse is not generally available.

Frequency Domain Interference (FDI), where an unchirped reference pulse and probe pulse shorter in duration than a plasma period were used [127-129], put the phase

information in a carrier, analogous to phase sensitive lock- in detection. Complete temporal phase information was recovered. Expressed in an equation:

$$|E_{\text{ref}} + E_{\text{pro}} \exp[j\Phi(\omega)]|^2 = |E_{\text{ref}}|^2 + |E_{\text{pro}}|^2 + E_{\text{ref}}E_{\text{pro}} \cos[\Phi(\omega)], \quad (2-1)$$

where E_{ref} and E_{pro} are the frequency domain amplitudes of reference and probe pulse, and $\Phi(\omega)$ — the phase difference between probe and reference in the frequency domain. Since the probe pulses were not chirped, the phase shifts for all frequency components were about the same. Thus the longitude resolution of FDI was basically the pulse duration. Phase shifts were radially integrated, so the radial structure of plasma waves were not measured by FDI. To map out the whole longitudinal plasma wave structure, multiple shots with different pump – probe delays had to be used. Most of the time, laser energy or profile fluctuates from shot to shot. Multiple shot measurement is prone to error and time consuming. To use multiple shots with different delays at the same time, temporal multiplexing must be used.

2.4. SINGLE-SHOT VISUALIZATION: BASICS OF FDH

Frequency Domain Holography (FDH) images quasi-static structures propagating near light speed c through a transparent medium from the phase modulation they imprint on a long, wide probe pulse that co-propagates with and illuminates the entire object at once, like the “object” beam of conventional holography (see Fig. 2-1). Interference of this probe with a co-propagating, temporally separate “reference” pulse on a detector

encodes the object's phase structure, which is subsequently “read” to reconstruct the object, completing the analogy with conventional holography.

2.4.1. The plasma object

A He plasma containing a luminal-velocity plasma wakefield (the “object”) was created by focusing a ~ 1 J, 800 nm, 30 fs pulse from the HERCULES laser system [130] into a supersonic He gas jet with an f/13 off-axis parabolic mirror (see fig. 2-2), resulting in typical pump spot radius ~ 25 μm at the jet entrance. Images of moving plasma objects $n_e(r, \phi, \zeta, z)$ (where r is radial distance from the propagation axis, ϕ is azimuthal angle around the propagation axis, ζ is the distance behind the drive pulse and z is the drive pulse drive pulse propagation distance into the plasma) reported here are cross-sections at fixed ϕ , so we shall drop the argument ϕ hereafter. Changes in the object’s shape with z can occur because of longitudinal variations in gas jet density and/or drive pulse intensity, and/or because of inherent instabilities in the propagating plasma object. Since FDH averages over such variations, the sharpest images are recovered for quasi-static objects that experience minimal longitudinal variations.

Phase variations $\Delta \phi_{pr}(r, \zeta)$ that the object imprints on the probe are obtained from its refractive index profile $\eta(r, \zeta, z) = [1 - \omega_p^2(r, \zeta, z) / \omega_{pr}^2]^{1/2}$, where ω_p is the plasma frequency corresponding to local electron density $n_e(r, \zeta, z)$, $\gamma = (1 - v^2/c^2)^{1/2}$ is the relativistic Lorentz factor, and e , m and v are the electron charge, rest mass, and

oscillation velocity, respectively. For a tenuous fully-ionized plasma, $\eta - 1 \approx \omega_p^2 / 2\omega_{pr}^2$, so $\eta - 1$ is proportional to $n_e(r, \zeta, z)$ – i.e. $\eta(r, \zeta, z) - 1$ is a replica of the object.

2.4.2. Reference and probe pulses.

Approximately 10% of the energy of the driving pulse was split off prior to compression for a diagnostic pulse, which was independently compressed to 30 fs, then subdivided into reference and probe pulses. In their original FDH work, Le Blanc *et al.* [131] produced the latter in a modified Michelson interferometer, which proved sensitive to small misalignments and yielded probe and reference pulses with different temporal and spatial profiles. Matlis *et al.* [80] developed a more robust, compact configuration that resembles a Fabry-Perot interferometer (see Fig. 2-2), and produced nearly identical reference and probe pulses. The incident 800 nm diagnostic pulse first up-converted to 400 nm in a $\sim 200 \mu\text{m}$ KDP crystal, thin enough to preserve its wide bandwidth. The nearly undepleted 800 and 400 nm pulses then passed through 2 to 3 cm of fused silica, in which they separated temporally by $\tau \approx 3$ ps by group-velocity walk-off. The temporally advanced 800 nm pulse then upconverted in an identical KDP crystal, generating a second 400 nm pulse collinear with the first, of identical spatial profile, and advanced in time by $\tau \approx 3$ ps. The 400 nm pulses recombined collinearly with the pump through a 2.5-cm thick high-reflector for 800 nm with high transmission and group velocity dispersion (GVD) at 400 nm. Both 400 nm pulses chirped to $\tau_{pr} \sim 1$ ps duration upon transmission through this optic, establishing the length $c\tau_{pr}$ of the object that was illuminated for FDH imaging. By inserting additional dispersive glass into the probe-

reference line, $c\tau_{pr}$ can be easily controlled. Using probe and drive pulses with large wavelength difference $\Delta\lambda \equiv \lambda_{pu} - \lambda_{pr}$ facilitates their separation after the interaction region, at the expense of introducing group-velocity walk-off between probe and object in the plasma medium.

2.4.3. Recording frequency-domain holograms

From interacting with the object over length L , the probe acquires phase shift

$$\Delta\phi_{pr}(r, \zeta) = \frac{2\pi}{\lambda_{pr}} \int_0^L [1 - \eta(r, \zeta, z)] dz \approx \frac{e^2 \lambda_{pr}}{mc^2} \int_0^L \frac{n_e(r, \zeta, z)}{\gamma(r, \zeta, z)} dz \quad (2-2)$$

with respect to the reference pulse, thus encoding the object's structure, where the last expression holds for tenuous plasma. From Equ. 2-2, if the object's instantaneous structure $\eta(r, \zeta, z)$ or $n_e(r, \zeta, z)$ evolves with z , the probe phase imprint averages these changes. Even for a non-evolving object, group-velocity walk-off between the 400 nm probe pulse and the wake propagating at the group-velocity of the 800 nm drive pulse causes longitudinal averaging. As a rough criterion, plasma wakes and probe should walk-off less than $\lambda_p/4$ to avoid blurring sub- λ_p structure, limiting interaction to [101] $L = \lambda_p^3/4\lambda_{pu}\Delta\lambda$, or $L \sim 1$ mm for $n_e \sim 10^{19}$ cm⁻³. When structural evolution and group-velocity walk-off are negligible, Equ. 2-2 simplifies to

$$\Delta\phi_{pr}(r, \zeta) \approx \frac{2\pi[1 - \eta(r, \zeta)]L}{\lambda_{pr}} \approx \frac{e^2 \lambda_{pr} L n_e(r, \zeta)}{mc^2 \gamma(r, \zeta)} \quad (2-3)$$

where, again, the last expression holds for tenuous plasma. Equation 2-3 is often adequate for estimating the object's structure directly from measured probe phase shift.

After the interaction region, a dichroic mirror separated probe and reference pulses from the transmitted drive pulse, then a lens imaged them from the exit plane of the plasma onto the entrance slit of an imaging spectrometer, which selected a constant ϕ cross section (see fig. 2-1). To record an orthogonal cross section for 3-D imaging, a beam splitter could direct half of the probe-reference energy to a second spectrometer with an orthogonal entrance slit. Transverse image resolution was limited by the high intensity of the transmitted pump, which forces the dichroic and imaging optics to be placed tens of cm from the gas jet to avoid optical damage. For the images presented here, an optic with $f\# = 8$ yielding resolution close to the theoretical limit $f\#\lambda_{pr} \sim 3 \mu\text{m}$ was used.

The signal recorded at the detection plane of the spectrometer has the form [131],[132]

$$\begin{aligned} S(r, \omega) &= |E_{pr}(r, \omega)|^2 + |E_{ref}(r, \omega)|^2 + E_{pr}^*(r, \omega)E_{ref}(r, \omega) + E_{pr}(r, \omega)E_{ref}^*(r, \omega) \\ &= |A_{pr}(r, \omega)|^2 + |A_{ref}(r, \omega)|^2 + 2A_{pr}(r, \omega)A_{ref}(r, \omega)\cos[\omega_0\tau + \Delta\phi_{pr}(r, \omega)] \end{aligned} \quad (2-4)$$

where $E_{ref}(r, \omega) = A_{ref}(r, \omega)\exp[i\phi_{ref}(r, \omega)]$ and

$E_{pr}(r, \omega) = A_{pr}(r, \omega)\exp[i\phi_{pr}(r, \omega) + i\omega\tau]$ denote complex electric fields of reference and probe pulses, respectively, as functions of transverse position r along the spectrometer slit and frequency ω , τ is the time delay of probe from reference, and $\Delta\phi_{pr}(r, \omega) = \phi_{pr} - \phi_{ref}$ is the phase difference between probe and reference caused by

interaction of the former with the plasma object. In the absence of a plasma object, $\Delta\phi_{pr} = 0$, so r -independent frequency-domain interference fringes $\cos\omega_0\tau$ with period $2\pi/\tau$ are observed (see lower interferogram in Fig. 2-1). When the plasma object is present, $\Delta\phi_{pr}$ is given by Equ. 2-2 and 2-3, so distorted fringes that encode the object's structure are observed (see upper interferogram in Fig. 2-1). CCD pixel density, spectrometer dispersion, and τ are chosen such that 10 to 15 pixels record each period of the interferogram, ensuring adequate resolution when recovering images.

2.4.4. Reading frequency-domain holograms

Whereas conventional holograms are read by diffracting a laser beam from the exposed recording medium, we read FD holograms electronically by a Fourier transform (FT) procedure. First, the complete probe electric field $E_{pr}(\omega) = |E_{pr}(\omega)| \exp[i\phi_{chirp}^{(pr)}(\omega) + i\Delta\phi_{pr}(\omega)]$ is reconstructed in the frequency domain from FDH data at each transverse position r_0 . Second, Fourier transformation of $E_{pr}(\omega)$ yields the time domain field $E_{pr}(\zeta) = |E_{pr}(\zeta)| \exp[i\phi_{chirp}^{(pr)}(\zeta) + i\Delta\phi_{pr}(\zeta)]$. Finally, the temporal phase perturbation $\Delta\phi_{pr}(\zeta)$ yields electron density profile $n_e(\zeta)$ at each r via Equ. 2-2 and 2-3. Along with $\Delta\phi_{pr}(r, \zeta)$, FT of $E_{pr}(r, \omega)$ simultaneously outputs temporal probe amplitude $|E_{pr}(r, \zeta)|$. For weakly refracting plasma, however, $|E_{pr}(r, \zeta)|$ at $z = L$ hardly changes from its incident profile, and thus conveys no information about the plasma structure. In strongly refracting, denser plasma, on the other hand, informative

new features can appear in $|E_{pr}(r, \zeta)|$, creating a shadowgram at $z = L$. This latter case is discussed in the next chapter.

Reconstruction of $E_{pr}(r_0, \omega)$ begins with a lineout $S(r_0, \omega)$ of a FD hologram (see Fig. 2-3(a)). Fourier transformation of $S(r_0, \omega)$ yields $\tilde{S}(r_0, t)$ consisting of a central peak at $t = 0$ corresponding to the FT of $|E_{pr}(\omega)|^2 + |E_{ref}(\omega)|^2$, and side peaks at $t = \pm \tau$ corresponding to the FT of $E_{pr}^*(\omega)E_{ref}(\omega)$ and $E_{pr}(\omega)E_{ref}^*(\omega)$, respectively (see Fig. 2-3(b)). One side peak is windowed (Fig. 2-3(b), dashed box), then inverse Fourier-transformed, yielding $E_{pr}(\omega)E_{ref}^*(\omega) = |E_{pr}(\omega)||E_{ref}(\omega)|\exp[i\Delta\phi_{pr}(\omega)]$. This expression is divided by the separately measured reference power spectrum $|E_{ref}(\omega)|$ (Fig. 2-3(c)). Finally, probe chirp $\phi_{chirp}^{(pr)}(\omega)$ is measured independently by a method such as the one shown in Fig. 2-3(d), in which the chirped 400 nm probe interferes in the frequency domain with a compressed (~ 30 fs) 400 nm reference pulse. In principle, the measurements in Figs. 2-3(c) and (d) should be performed on each shot, and at each r . In practice, we found $|E_{ref}(\omega)|$ and $\phi_{chirp}^{(pr)}(\omega)$ sufficiently stable and uniform that a single, spatially averaged measurement sufficed.

2.5. HOLOGRAPHIC IMAGES OF LASER WAKEFIELDS

A number of FDH images of sinusoidal laser wakefields generated in plasma of density $n_e < 6 \times 10^{18} \text{ cm}^{-3}$ by laser pulses of either 10 TW or 30 TW peak power were

published and discussed in [80]. Here we discuss an image that was recorded by N.H. Matlis, but was not published in 2006 because it contained some features (detailed below) that were not understood at that time. The anomalies in question were present in many of Matlis' images of wakefields generated by 30 TW laser pulses. As part of the work of this thesis, a physical interpretation of these apparent anomalies was developed, and subsequently validated by simulations performed by S. A. Yi and K. Y. Kalmykov. This image, its full interpretation and the simulation were then published for the first time [124] in collaboration with N. H. Matlis. Fig. 2-4(a) shows the FDH image in question, a wake produced by a pulse of peak power 30 TW and vacuum focused intensity $\sim 3 \times 10^{18}$ W/cm² in a plasma of density $n_e = 2.7 \times 10^{18}$ cm⁻³ at the jet centre, measured independently by transverse interferometry. The image appears both as a 3-D false color plot of $\Delta\phi_{pr}(r, \zeta)$ over the ranges $-60 < r < 60$ μm and $0 < \zeta < 0.4$ ps, and as a planar gray-scale projection of the same data. Fig. 2-4(b) shows one snapshot of electron density taken near the centre of the jet in a WAKE [77] simulation performed by S. A. Yi and K. Y. Kalmykov. The laser pulse is self-focused at this location to a spot size $x_{\text{foc}} \approx 19.5$ μm (full width at half-maximum (FWHM) in intensity) and peak intensity $I_{\text{foc}} \approx 5.5 \times 10^{18}$ W/cm².

Three features of the $\Delta\phi_{pr}(r, \zeta)$ image agree quantitatively with features of wake density oscillations $n_e(r, \zeta)$ expected from theory. These points of agreement were described previously [80] in connection with images of wakes generated by 30 TW laser pulses, and are summarized briefly here for completeness. First, six plasma oscillations

occur within 0.4 ps, yielding a period of 67 fs, in excellent agreement with the period $2\pi/\omega_p = 67.6$ fs expected for a plasma of density $n_e = 2.7 \times 10^{18}$ cm⁻³. Thus, the oscillations are indeed electron Langmuir waves. Secondly, the transverse FWHM of the peaks is $x_{\text{FWHM}} \approx 20$ μm, in excellent agreement with the self-focused spot size of the pump pulse. Thirdly, the progressively increasing curvature of the wake fronts from nearly flat profiles immediately behind the pump to concave fronts with radius of curvature $r_c \sim 60$ μm after 6 oscillations agrees with simulations of strongly-driven, nonlinear wakes [87],[133]. The wavefronts curve because as plasma wave amplitude $\delta_0 \equiv |\delta n_e(r=0)/n_e|_{\text{max}}$ approaches unity on axis, electrons making up the wave oscillate relativistically, causing $\omega_p(r=0)$ to decrease by $\sqrt{\gamma}$ relative to its off-axis value. For mildly relativistic wakes, theory and simulations [134] suggest that curvature increases with ζ as $r_c^{-1}(\zeta) \approx 0.45\zeta(\delta_0/w_0)^2$. Here δ_0 refers to the amplitude of the first density maximum behind the pump and w_0 to the transverse radius of the wake. Analysis of wavefront curvature in Fig. 2-4 yields $\delta_0 \approx 0.2$.

One feature of the image in Fig. 2-4 (a) that was not described in the images presented in [80] is that, increasing phase front curvature is correlated closely with progressive growth in the amplitude of density and probe phase perturbations. Fig. 2-4(b) shows a WAKE simulation, carried out by S. A. Yi and K. Y. Kalmykov for the conditions of Fig. 2-4(a), that reproduces the correlated growth in plasma wave curvature and amplitude behind the drive pulse for the case of radially-dependant $\bar{\delta}$. Looking closely, in Fig. 2-4(b) density perturbations increase in a slightly of ζ -axis annulus,

whereas on axis the amplitude does not change. In the FDH image Fig. 2-4(a), the dip on axis is not resolved, but the growth in peak wake amplitude agrees closely with the simulations in most other respects. The close agreement shows that FDH has captured two functionally important features of the wake field for the first time: relativistic wave front curvature, which helps to collimate the accelerated beam, and wave spiking, a precursor of wave breaking and electron injection. The simulation of Fig. 2-4(b) stops just before the onset of wave breaking. The enhancement of wake amplitude can be understood physically by comparing it to the process of compressing an initially spatially chirped laser pulse. As for the chirped laser pulse, here we have a nonlinear plasma wake with a radially-dependant plasma frequency. To compress the laser pulse, its dispersed frequency components must be brought together coherently. When this is done, its pulse duration decreases and its peak intensity rises. Analogously in the nonlinear plasma wave, as distance back from the driver grows, trajectories of electron fluid elements oscillating at neighboring radial locations approaching each other more and more closely and begin to overlap. As a result the plasma pulses compress, decreasing in width and increasing in peak amplitude.

A similar compression process had been observed in simulation of nonlinear plasma wakes in plasma channels, where the radially-dependent plasma frequency arose from the radial density gradient instead of from the radial gradient of the relativistic γ of the plasma electrons as in our case. Those calculations [135],[133],[136] found that the off-axis wake amplitude can grow with distance behind the driver, and can even result in electron injection into the channel. This was because some finite distance the electron

trajectories cross [137], and the wake breaks transversely [138],[139]. Correlated growth in wave curvature and amplitude is thus a precursor of wave breaking and electron injection.

A second feature of the image in Fig. 2-4(a), and of numerous other wakefield images, that was not explained in the work of [80] is the erratic structure near $\zeta = 0$ that does not correspond to expected wake structure $n_e(r, \zeta)$. In other images, such as Fig. 2-5, this appears as fine-scale transverse periodic modulations near $\zeta = 0$ which, again, have no counterpart in computer simulation of the plasma structure. One cause of this false structure that was first discovered in the work of this thesis is interference of radiation at $\lambda \sim 400$ nm, produced by the diverging pump via relativistic second-harmonic generation (SHG) or white-light continuum generation, with the collimated probe and reference, resulting in false structure near $\zeta = 0$ upon reconstruction. Understanding of such structures is important both for removing unphysical artifacts from FDH images and for characterizing nonlinear optical interactions of intense laser pulses with plasmas, such as relativistic harmonic generation and self-phase modulation.

To demonstrate how the false structure could arise, we performed a prototype experiment using 200 mJ, 100 fs, 800 nm beam. It was then split by a 90:10 beam splitter. The weaker beam was converted to two 400 nm probe beams by two 200 μ m thick KDP crystal with a 5 mm HZF4 glass in between, similar to the configuration shown in the upper right portion of Fig. 2-2. HZF4 glass has high group velocity dispersion, similar to SF10 glass. The two 400 nm pulses were then chirped by passing

through 25 mm of HZF4 glass. Afterwards the probes were loosely focused and combined collinearly through a dichroic mirror with the pump beam which was focused by $f\# = 6$ off axis parabola. Both beams were focused into a differentially pumped Helium gas cell with backing pressures ranging from 2 psi to 100 psi. The gas cell is comprised of 2 pinholes and glass side view window. Most of the transmitted 800nm beam is dumped by a 0 degree high reflector after the gas cell. Several BG39 filters before the spectrometer was used to block the rest of the pump beam. A lens with focal length 190mm then imaged the interaction region onto the spectrometer slit.

Originally, this experiment was expected to image wakefield oscillation driven by a long (100 fs) pump pulse either in the resonant regime (plasma density $\sim 10^{17}/\text{cm}^3$) or self-modulation regime (plasma density $\sim 10^{18}/\text{cm}^3$). However, the phase accumulation at self-modulation regime was too small to be detected by FDH and the pump pulse focused intensity ($I \sim 10^{17} \text{ w/cm}^2$) was too weak to create a wakefield and only enough to ionize the helium gas. Instead, we observed a weak second harmonic pulse that diverges rapidly after the cell and spectrally interferes with the collimated probe and reference pulses at the same wavelength. Many mechanisms can generate laser harmonics in plasmas. In the case of the second harmonic, the main mechanism is the presence of density gradients in the plasma [140]. Here the density gradients come from the ionization process and laser radial ponderomotive force.

One typical FDH image is shown in Fig 2-6. Vertical, regularly spaced fringes from FD interference of probe and reference pulses are clearly visible. A coarser modulation of variable period caused by the ionization front is also evident. However,

the feature of interest here is the series of elliptical "Newton rings" in the center, which is superimposed on the background of approximately vertical features described previously. Qualitatively these rings originate from FD interference of rapidly diverging, unchirped pump-generated SHG with collimated, chirped 400 nm probe and reference pulses. To understand those "Newton ring" features quantitatively, we need to look at the interference between the SHG pulse and probe pulse.

$$\begin{aligned}
E(\omega)_{SHG} &= E_{pump} \exp\left[\frac{-1}{4A}(\omega - \omega_0)^2\right] \exp\left[-jk\frac{r^2}{2R}\right] \exp[jt_0\omega] \\
E(\omega)_{probe} &= E_{probe} \exp\left[\frac{-a}{4(a^2+b^2)}(\omega - \omega_0)^2 - \frac{-b}{4(a^2+b^2)}(\omega - \omega_0)^2\right] \\
|E(\omega)_{SHG} + E(\omega)_{probe}|^2 &= E(\omega)_{pump} E_{probe} \exp\left[\left(\frac{-1}{4A} + \frac{-a}{4(a^2+b^2)}\right)(\omega - \omega_0)^2\right] \times \\
&\quad \cos\left[\frac{-b}{4(a^2+b^2)}\left(\omega - \omega_0 + \frac{2t_0(a^2+b^2)}{b}\right)^2 - k\frac{r^2}{2R} + t_0\omega_0 - \frac{t_0(a^2+b^2)}{b}\right] \quad (2-5)
\end{aligned}$$

where A and a are determined by pulse duration, b is determined by chirping of the pulse, R is the radius of curvature at the imaging plane. $E(\omega)_{SHG}$ is pump generated second harmonic beam with center frequency at ~400nm. In the temporal domain, both pump and probe pulses have the form $E(t) = \exp[-at^2]\exp[j(\omega_0 t + bt^2)]$.

The argument of the cosine function in Equ. 2-5 describes an ellipse in ω - r space with major axis determined by the probe parameters a, b and minor axis by R. We have observed the elliptical Newton rings transform to hyperbolae when the SHG pulse is converging at the image plane, reversing the sign of R. When the interferogram is Fourier-transformed, the frequency-domain Newton rings appear as false structure

temporally coincident with, and radially flanking, the pump pulse, as shown in the bottom of Fig. 2-6. The false structure is the similar as in Fig. 2-5. However, the second harmonic generation in the latter case can come from nonlinear Thomson scattering as demonstrated by Chen et al [141]. By performing Fourier filtering in the spatial axis, the effect of the Newton rings on the real data can be reduced but not eliminated. However, this type of artifact can be avoided by using probe pulses at wavelength other than harmonics of the pump, as long as pump-generated continuum is also avoided. One way to do this is to use Raman-shifted probe pulses at 870nm (or their harmonics) [142] so that their spectrum don't overlap in the spectrometer.

2.6. SUMMARY

In this chapter I introduced the FDH technique which can record objects moving at luminal velocity. The basic setup and reconstruction method is discussed. The previous FDH work in tenuous plasma by N. H. Matlis was briefly reviewed. Two new features that were not covered in Matlis' work [80] were investigated. The correlated growth in plasma wave curvature and amplitude behind the drive pulse was explained qualitatively and confirmed by simulation. The transverse features near $\zeta = 0$ are caused by pump-generated second harmonic and (or) white light continuum, that interferes with the probe and (or) reference pulses.

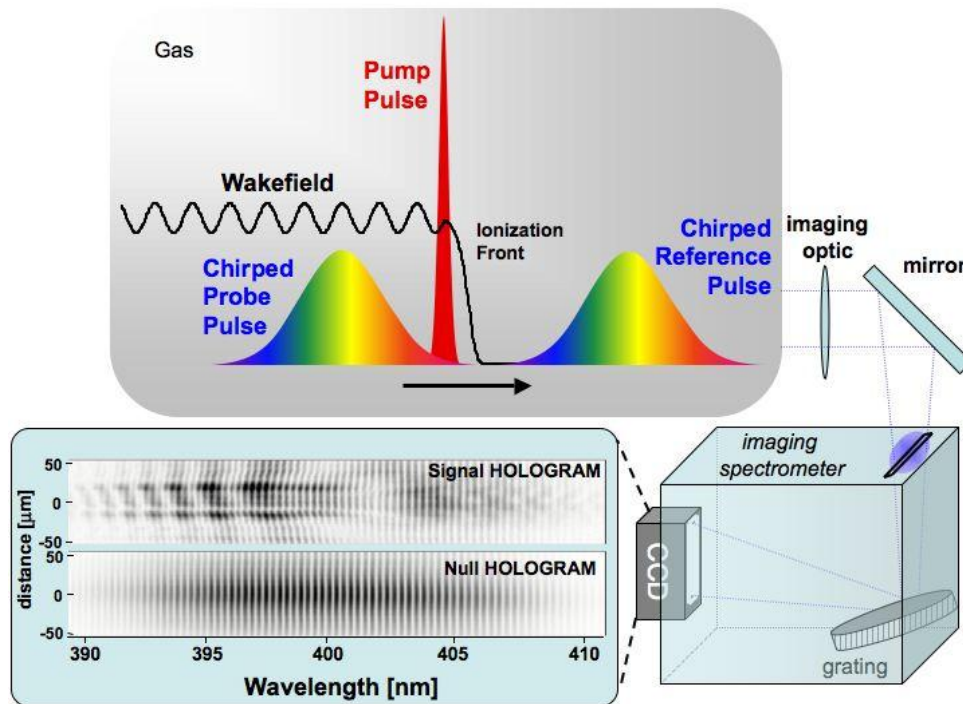


Figure 2-1. Schematic Frequency Domain Holography (FDH) configuration for imaging laser wakefields. Two chirped ps duration pulses (reference and probe) co-propagate with the pump. Phase and amplitude alterations imposed on the trailing probe by the wake are encoded in a frequency domain interferogram, shown at bottom with (upper) and without (lower) a pump, recorded by a CCD camera at the detection plane of an imaging spectrometer with ~ 12 pixels/fringe. Fourier transformation of this data recovers wake structure. This is Fig. 1 of [124], but some details were adopted from Fig. 1 of [80].

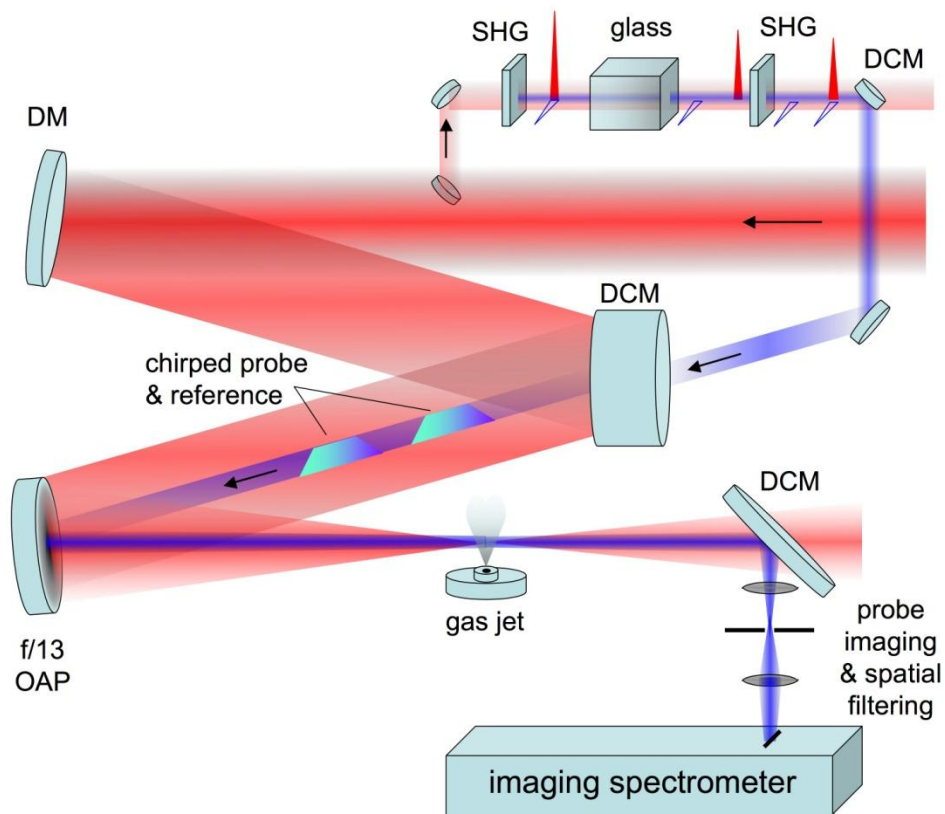


Figure 2-2. Practical FDH configuration for imaging laser wakefields. An $f/13$ parabola focuses an intense 30 fs pump pulse into a jet of He gas, creating a plasma and laser wakefield. The reference-probe pair pulse sequence is created from an incident 800 nm diagnostic pulse that is apertured to ensure a focal spot larger than that of the pump, then upconverted to 400 nm and divided into two pulses by passing through KDP crystal/glass/KDP crystal “sandwich”, as described in the text.

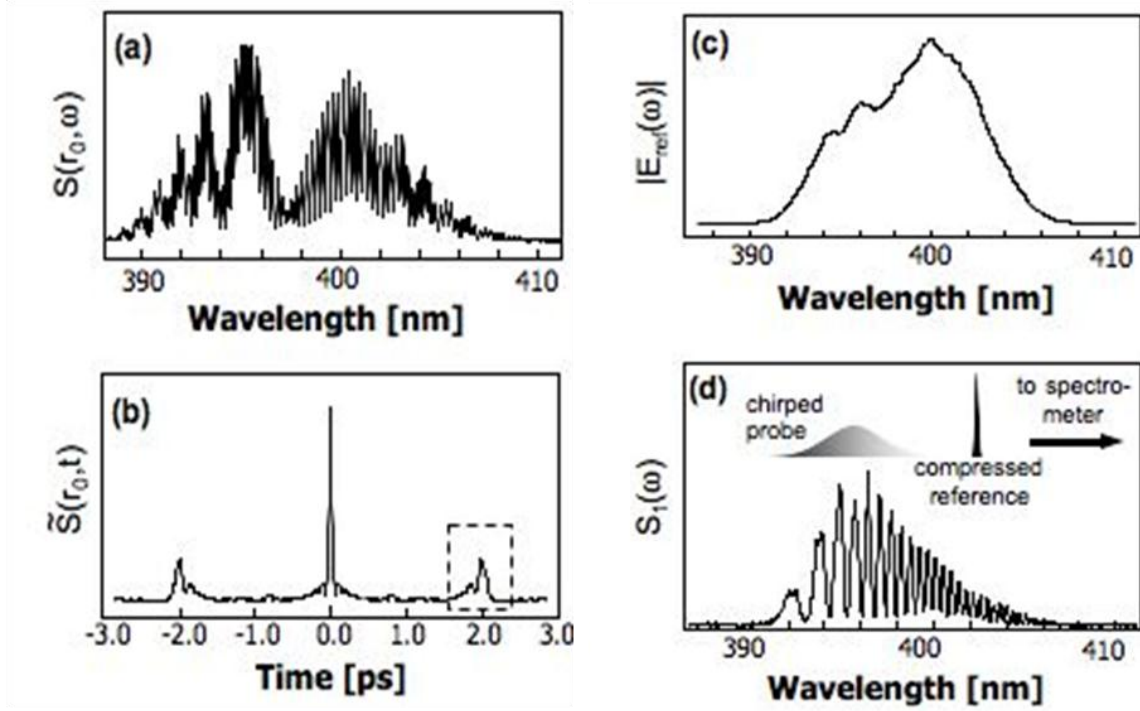


Figure 2-3. Reconstructing probe electric field. **(a)** Lineout of recorded intensity $\tilde{S}(r_0, t)$ at one transverse position r_0 . **(b)** Fourier-transformed intensity $\tilde{S}(r_0, t)$; dashed box highlights peak corresponding to $\text{F.T.}[E_{pr}(\omega)E_{ref}^*(\omega)]$, which is subsequently windowed and inverse Fourier-transformed back to FD to isolate cross term $E_{pr}(\omega)E_{ref}^*(\omega) = |E_{pr}(\omega)||E_{ref}(\omega)|\exp[i\Delta\phi_{pr}(\omega)]$. Normalizing this to separately measured **(c)** power spectrum $|E_{ref}(\omega)|$ of reference pulse and **(d)** FD interference pattern of chirped probe with short pump pulse, which measures $\phi_{chirp}(\omega)$, we obtain the complete probe electric field $E_{pr}(\omega) = |E_{pr}(\omega)|\exp[i\Delta\phi_{pr}(\omega) + \phi_{chirp}(\omega)]$.

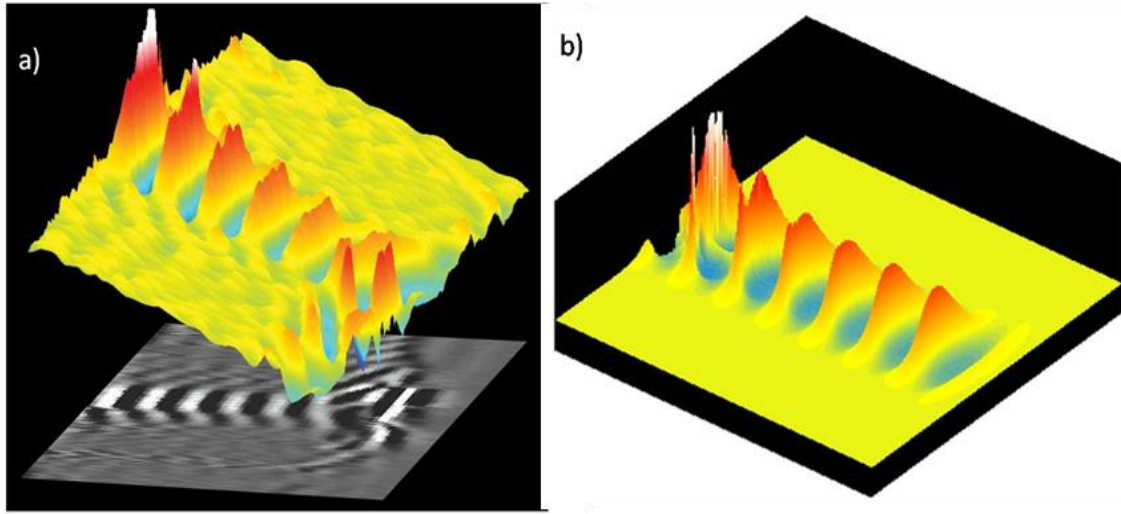


Figure 2-4. Panel (a): single-shot image of a wakefield produced by a 30 TW laser pulse in plasma of electron density $n_e = 2.7 \times 10^{18} \text{ cm}^{-3}$. The colour surface shows a phase change $\Delta\phi_{pr}(r, \zeta)$ of the probe pulse. The grey-scale image is the projection onto a plane. A large index step induced by the ionization front has been subtracted to emphasize the oscillatory wake structure. Panel (b): Electron density snapshot from the WAKE simulation taken near the gas jet centre in the region near axis (the helium gas is fully ionized there). The peak electron density perturbation in the first three periods is about $2n_e$. The transverse dimension of the images is $120 \text{ }\mu\text{m}$, while longitudinally they represent a time span of 0.4 ps . The largest $\Delta\phi_{pr}(r, \zeta)$ (white colour in the panel (a)) corresponds to 22% refractive index perturbation of the background plasma (yellow in panel (a)) averaged over the interaction length. Figure recorded by N. H. Matlis, and published with analysis of previously unexplained features in [124].

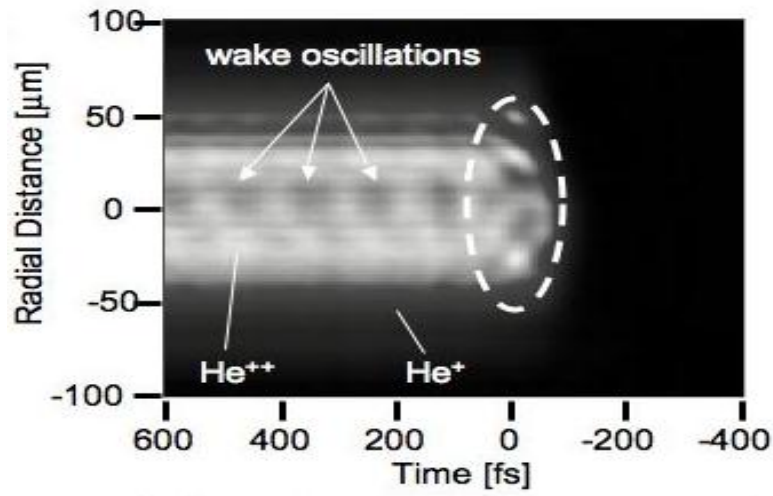


Figure 2-5. 2D grayscale map of reconstructed phase change $\Delta\phi_{pr}(r, \zeta)$ imposed on the probe by the plasma structure propagating in the wake of the pump pulse from [80]. The dashed ellipse highlights periodic false structure near $\zeta = 0$ that was unexplained in the work of [80].

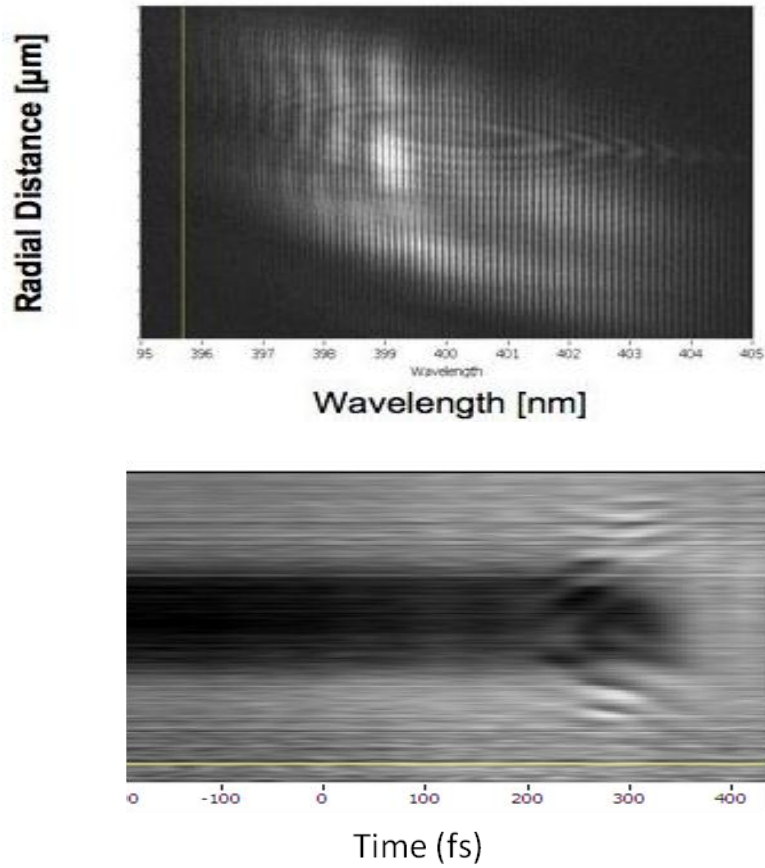


Figure 2-6. Top: Raw FD hologram resulting from interference of probe and reference pulses in detection plane of imaging spectrometer. Elliptical “Newton rings” are visible in the center of the hologram. Bottom: Reconstruction of ionization front with false structure. The false structure is quite similar to the highlighted periodic false structure near $\zeta = 0$ in Fig. 2-5.

Chapter 3. Visualization of Laser Wakefields in Dense Plasma: Frequency-Domain Shadowgraphy

In this chapter, I present an entirely new set of experiments that extends visualization of laser-plasma accelerator (LPA) structures to the most important regime in current LPA science: The “bubble” [22] or “blowout” regime. As pointed out in the introduction to Chapter 1 and sec. 1.3.3.5, the bubble regime underlay an experimental breakthrough in 2004 in which LPAs for the first time produced high quality, monoenergetic, collimated beams of electrons just like conventional accelerators [12-14], with energy that had reached 1 GeV by 2006 [15]. To access the bubble regime, drive laser intensity must reach $I \sim 10^{19}$ W/cm² ($a_0 \sim 3$), about an order of magnitude higher than experiments described in Chapter 2, so that the ponderomotive force becomes high enough to blow out the required electron density bubble. In our experiments, we achieved part of this intensity increase by focusing the 30 TW drive laser pulse more tightly (see Sec. 3.4). However, as in all previous LPA experiments in the bubble regime, most of the intensity increase was achieved by shifting to higher plasma density ($n_e > 10^{19}$ /cm³ instead of low 10^{18} /cm³). This reduced the critical power P_c for relativistic self-focusing (see Equ. 1-16), so the drive laser pulse self-focused to the required intensity through its initial nonlinear interaction with the plasma. Once the bubble formed, its high refractive index cavity helped to guide and temporally compress the drive laser pulse through the remainder of the plasma. Oscillation of the laser pulse spot size $w(z)$, and thus of the bubble size, resulting from the non-mode-matched initial self-focus helped to trigger self-injection of electrons from the surrounding plasma into the bubble accelerator [23]. Thus in the new experiments, unlike the 2006 experiments of Matlis *et al* [80] that produced no relativistic electrons, we were able to correlate LPA visualization data with the properties of accelerated electron on most shots. At the same

time, the standard FDH techniques developed by Matlis *et al* [80] encountered new problems at high n_e that are summarized in Sec. 3.1. In response to these problems, I developed the revised technique of Frequency Domain Shadowgraphy (FDS), which measures and analyzes the changes in amplitude, rather than phase, that the LPA structure imprints on a copropagating probe pulse. Because plasma bubbles focus, guide and compress the pulse that drives them, it is not surprising that they trap and compress probe light to form “optical bullets”, which were discovered and used for bubble characterization for the first time through the work of this dissertation [143].

3.1. NEW ISSUES IN VISUALIZING DENSE PLASMA STRUCTURES

The previous FDH experiment [80] imaged the linear wakefields at low plasma densities (up to $6 \times 10^{18} /\text{cm}^3$). In attempting to extend FDH to higher densities, we encountered several new problems. First, the white light continuum generated by self phase modulation of the pump pulse extended into the ~ 400 nm range. The white light thus interfered with the 400 nm probe and reference pulses, and even saturated the CCD camera, if no efforts were made to filter it. Second, the probe pulse phase often scrambled as it refracted and temporally compressed in the plasma bubble structure. Third, because of the high plasma density, the probe phase shift at some locations became as large as several times 2π . This made the phase retrieval and unwrapping extremely difficult because phase unwrapping is sensitive to noise and local high gradient [144]. Fourth, the probe pulse red shifted or blue shifted as it encountered strong longitudinal density gradient in bubble or ionization front. Thus the duration and chirping of the

probe pulse also changed as the bubble compressed it. Thus, the recovered phase is a complex combination of frequency shift, chirping, and simple phase shift where density is uniform. Under these circumstances, it becomes difficult to derive the plasma structure from recovered probe phase. On the other hand, the probe amplitude is an alternative to reveal plasma electron density information. Recovery of probe amplitude doesn't require phase unwrapping. Probe amplitude is enhanced by pulse compressing, and there is no analogy of 2π phase jumps and discontinuities. Much of the information carried by phase is also present in modified form in the probe amplitude. As discussed in Sec. 2.4.4, the amplitude reconstruction procedure is an integral part of FDH, and thus only requires a small change in the reconstruction algorithm used previously. In some cases it is possible to reconstruct both phase and amplitude at the same time, as discussed in Sec.3.7. The resulting comparison can be extremely valuable in characterizing bubble accelerator physics.

3.2. PREVIOUS METHODS OF CHARACTERIZING LASER WAKES IN DENSE PLASMA

An earlier effort to characterize wakefields in dense plasma ($n_e = 3 \times 10^{19} \text{ cm}^{-3}$) measured the temporal envelope of multiple plasma density oscillations in the wake of an intense ($I \sim 4 \times 10^{18} \text{ W/cm}^2$, $\lambda \sim 1 \mu \text{ m}$) laser pulse (400 fs) by forward collective Thomson scattering from a copropagating, frequency-doubled probe pulse [92],[145]. Because of interference between the probe pulse and plasma wave, certain wavelengths and directions were preferred for the Thomson scattering. Thomson scattered light, the probe light and the plasma wave all propagated in the same direction. The sidebands from the Thomson light were separated by the plasma frequency ω_p , and the wakefield

amplitude was calculated from the intensity of the sidebands. However, this technique did not reveal the internal structure or dynamics of the wake, because the probe bandwidth $\Delta \omega_{pr}$ was less than ω_p

In the bubble regime, early experiments [14] focused on characterizing the monoenergetic electrons that the accelerator produced, leaving bubble structure, dynamics and acceleration physics to computer simulations based on estimated initial conditions. More recent experiments, recognizing the importance of *in-situ* characterization of the accelerator structure itself, independent of accelerated electrons, characterized the bubble through its back reaction on the drive pulse [58]. For example, Thomas *et al.* [146] demonstrated the self-guiding of pump pulses over tens of Rayleigh ranges at certain optimized plasma densities for which bubbles are generated. They also showed that the self-guiding was most effective when the pump pulse focal spot size matched the blowout bubble radius. This was done by varying the pump focal spot from f#3 to f#12 with the pulse duration was roughly equal to the plasma period. The authors found that drive pulses with focal spots slightly smaller than the plasma wavelength could be guided over many Rayleigh ranges. Moreover, nearly monoenergetic electrons are observed in this case. However, too small focal spot results in multi-mode structures, preventing the production of high-quality electron beams. Kaluza *et al.* measured magnetic fields from laser-driven electron currents in the bubble regime using Faraday-rotation of a transversely propagating probe pulse[147]. Because the polarization of the probe pulse was affected by the magnetic field of the bubble sheath, those researchers, after mapping out the polarization change of the probe pulse, were able

to calculate the distribution of the \mathbf{B} field magnitude and deduce the electron beam duration, current, and charge.

3.3. EXPERIMENTAL PROCEDURE FOR SINGLE-SHOT VISUALIZATION OF BUBBLES

To implement FDS, we made revisions in both the experimental procedure and analysis used previously for FDH. We inserted a pinhole into the imaging system to block most of the white light without affecting the probe pulse. This discrimination was possible because the white light had much larger divergence after the interaction region than the probe pulse because of its smaller source size (*i.e.* the pump focus). The resolution of the imaging system was thus downgraded from $5 \mu\text{ m}$ to $\sim 10 \mu\text{ m}$. The energy of the probe pulse pair was also increased by approximately ten times to compensate for the light loss due to spatial filtering of pump-generated white light. This helped eliminated the white light problem in the density range where electrons were stably generated. In the analysis revision, we alternatively used probe amplitude to show the plasma electron density variation. The information carried by the phase also presented itself in the amplitude. Probe amplitude reconstruction, which is easier, faster, and less noisy than phase reconstruction, did not require the additional step of subtracting chirp phase $\phi_{chirp}^{(pr)}(\xi)$, did not require phase unwrapping, and was not affected by pulse compression, jump, and discontinuities.

Table 3-1 lists the differences between the 2006 and 2009 experiments. With more power used to generated probe pulses, the pump pulse power was slightly

decreased. However, the peak intensity was higher because of the smaller focal spot size.

Table 3-1: Comparison of experimental parameters: 2006 experiment versus 2009 experiment.

	Matlis 2006 Linear Regime	Dong 2009 Bubble Regime
Pump pulse power	~30 TW	~28 TW
Pump focal spot size	~25 μ m	~10 μ m
Probe pulse power	~0.2 TW before frequency doubling	~1.9 TW before frequency doubling
White light blocking	No.	Yes.
Electron generation	No.	Yes.
Amplitude reconstruction	No.	Yes
2D phase unwrapping	No.	Yes.
Gas density	Up to $6 \times 10^{18}/\text{cm}^3$	Up to $4 \times 10^{19}/\text{cm}^3$

Figure 3-1 shows the detailed experimental setup. For the experiment, we used the Ti:sapphire HERCULES laser system at the University of Michigan, which provided pulses of duration of 30 fs at 800 nm wavelength and peak power of 30 TW with less than 7% shot-to-shot fluctuation in power [148]. Inside the experimental chamber, a 1-inch diameter aluminum mirror reflected the center portion of the 4-inch diameter pump beam at 45 degrees to create the reference and probe beams. The reflected beam was

converted into two 400 nm probe pulses separated by 2 ps by passing the beam through a 200 μ m KDP crystal, a 0.5 inch BK7 glass, and another 200 μ m KDP crystal. After reflecting off a deformable mirror for wavefront correction to achieve an optimum focal spot size of 10 μ m, the pump pulse recombined collinearly with the probe pulse by means of an 800 nm dielectric mirror. After passing through the mirror, the probe and reference pulses were stretched to 1 ps. Both beams were focused by a 1-meter focal length parabola onto the front edge of a 1.7 mm supersonic gas jet. After the gas jet, a 400 nm high reflector transmitted most of the pump beam and reflected the probe and reference beams into a telescope system that imaged the rear side of the gas jet onto the slit of an imaging spectrometer. An iris was inserted into the imaging system to block pump-generated white light and second harmonic pulses by taking advantage of the different focusing geometries of the pump and probe pulses. For further discrimination, a polarizer was also inserted to block remaining pump light and transmit the orthogonally polarized probe beam. Electron beams were deflected by a 1-tesla magnet onto a fluorescing screen, where the electron spectrum was imaged by a CCD camera. A transverse Michelson interferometer outside the chamber measured the electron density of the laser produced plasma in the gas jet. Thomson scattered light was also collected from the top of the gas jet to monitor the plasma path through the plasma. Figure 3-2 shows the experimental setup.

For the Matlis 2006 experiment, the probe pulse was generated at the front end of the Hercules laser system. The probe pulse had its own compressor and the pump and probe pulses were synchronized before they entered the experimental chamber. For my experiment, because the compressor for the probe pulse was disassembled, we had to split off the probe pulse inside the chamber by inserting a small mirror in the path of the

pump pulse. We noticed no difference in the pump focal spot and electron generation with the small mirror inserted. Also, because everything had to fit inside the chamber, the probe pulse setup was very compact.

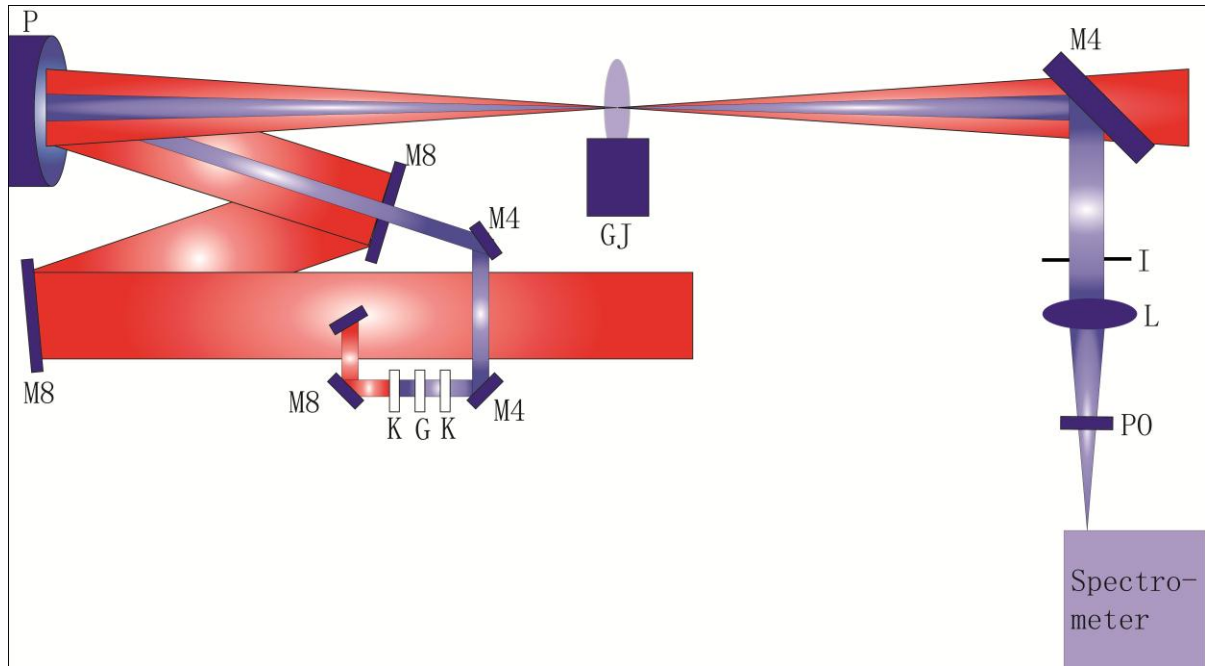


Figure 3-1. The experimental setup: P, parabola; M8, 800 nm dielectric mirror; M4, 400 nm dielectric mirror; K, KDP crystal; G, glass to generate time delay between the probe and reference pulse; GJ, gas jet; I, iris; L, imaging lens; and PO, polarizer.

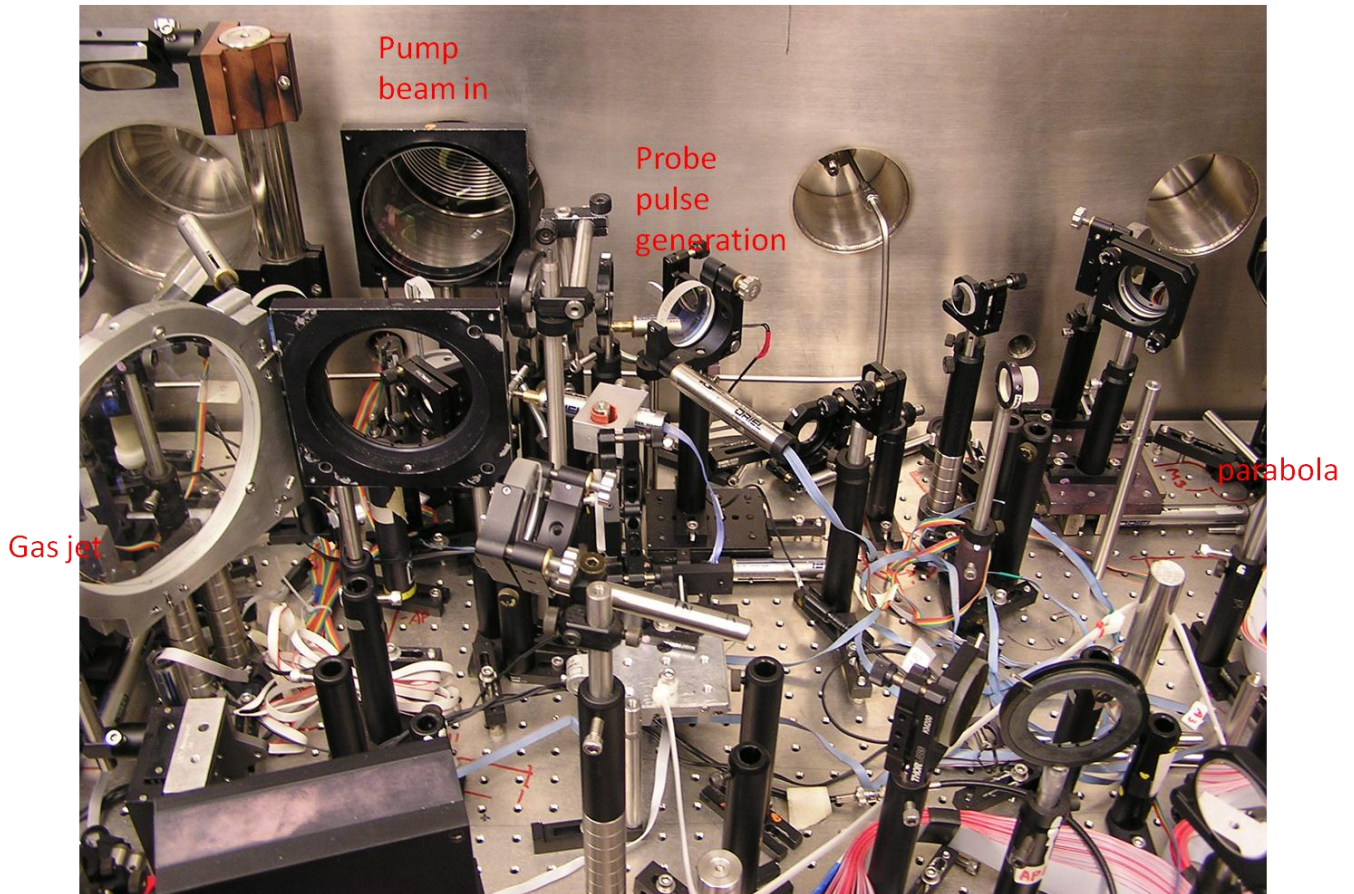


Figure 3-2: Photo of experimental setup. Parabola and gas jet is not shown.

3.4. ELECTRON GENERATION

Before showing the FDH snapshot, I will first describe the electron beam generation. Electron spectra were measured for plasma electron densities in the range from $2 \times 10^{18} \text{ cm}^{-3}$ to $3.2 \times 10^{19} \text{ cm}^{-3}$. The pump pulse focus position was varied from the entrance to the center of the gas jet. No accelerated electrons were detected in any plasma density when the laser focused at the jet center. Electron generation was optimized with the focus at the entrance of the gas jet. Relativistic electrons first appeared at $1.6 \times 10^{19} \text{ cm}^{-3}$ and were detectable at all higher densities.

With plasma density fixed, electron beams tend to have similar average characteristics (with some shot-to-shot fluctuations). As the plasma density changes, five acceleration regimes can be identified. Examples of electron spectra in these regimes are presented in Figure 3-3. Electron beams with low divergence (~ 3 mrad, lanex plate is 30 cm away from the gas jet), low charge (we define the charge of the beam on Fig 3-3 (1) as 1), and a wide, almost flat-top energy spectrum with a sharp cutoff around 90 MeV are observed at $n_e=1.7 \times 10^{19} \text{ cm}^{-3}$. The charge is low, but the trapped electrons are accelerated to high energies due to the long dephasing length (~ 0.15 cm, see Equ. 1-27). At $n_e=2.1 \times 10^{19} \text{ cm}^{-3}$, the electron beams become transversely wide (~ 10 mrad) and carry higher charges (20% higher than at $n_e=1.7 \times 10^{19} \text{ cm}^{-3}$). The electron spectra show a broad peak centered at 50 MeV and a span up to ~ 75 MeV. With higher charges, the beam loading effectively reduces the accelerating gradient and hence the peak electron energy [149]. At $n_e=2.4 \times 10^{19} \text{ cm}^{-3}$, the energy spectra show multiple sinusoidal tracks of electron beams, and the total charge grows further. Since the oscillations are perpendicular to the pump polarization, they are not caused by electron interaction with the effect of the linearly polarized laser electric field. They are possibly caused by out-of-plane betatron oscillations due to asymmetric off-axis injection, which probably is driven by an asymmetric laser pulse intensity distribution [150],[151]. At densities above $n_e=2.4 \times 10^{19} \text{ cm}^{-3}$, a further degradation of electron beam quality is observed. The beam is strongly dispersed in the transverse direction. Most electrons have energies less than 30 MeV, with a weak tail spanning up to 90 MeV. Quite surprisingly, at densities above $n_e=2.9 \times 10^{19} \text{ cm}^{-3}$, monoenergetic electron beams with less than 1% energy spread and small transverse sizes appear. Similar beams were observed in similar conditions by other research groups [152],[153].

In the entire density range from 1.6 to $3.2 \times 10^{19} \text{ cm}^{-3}$, polyenergetic electron beams were sometimes observed. These beams had several distinct electron energy peaks, as is displayed in Fig. 3-4. These peaks might be due to periodic electron injection in the evolving bubble or the trapping and acceleration of electrons in consecutive wake buckets [23],[154]. The wide variety of electron beam properties provides a test bed for multidimensional PIC simulations. Importantly, even with nominally the same laser beam profile, energy, and backing pressure of the gas jet, parameters of the electron beam fluctuate from shot to shot for densities above $2.1 \times 10^{19} \text{ cm}^{-3}$. This fluctuation shows the importance of *in-situ* measurements of the bubble structure, which will be discussed in the next section.

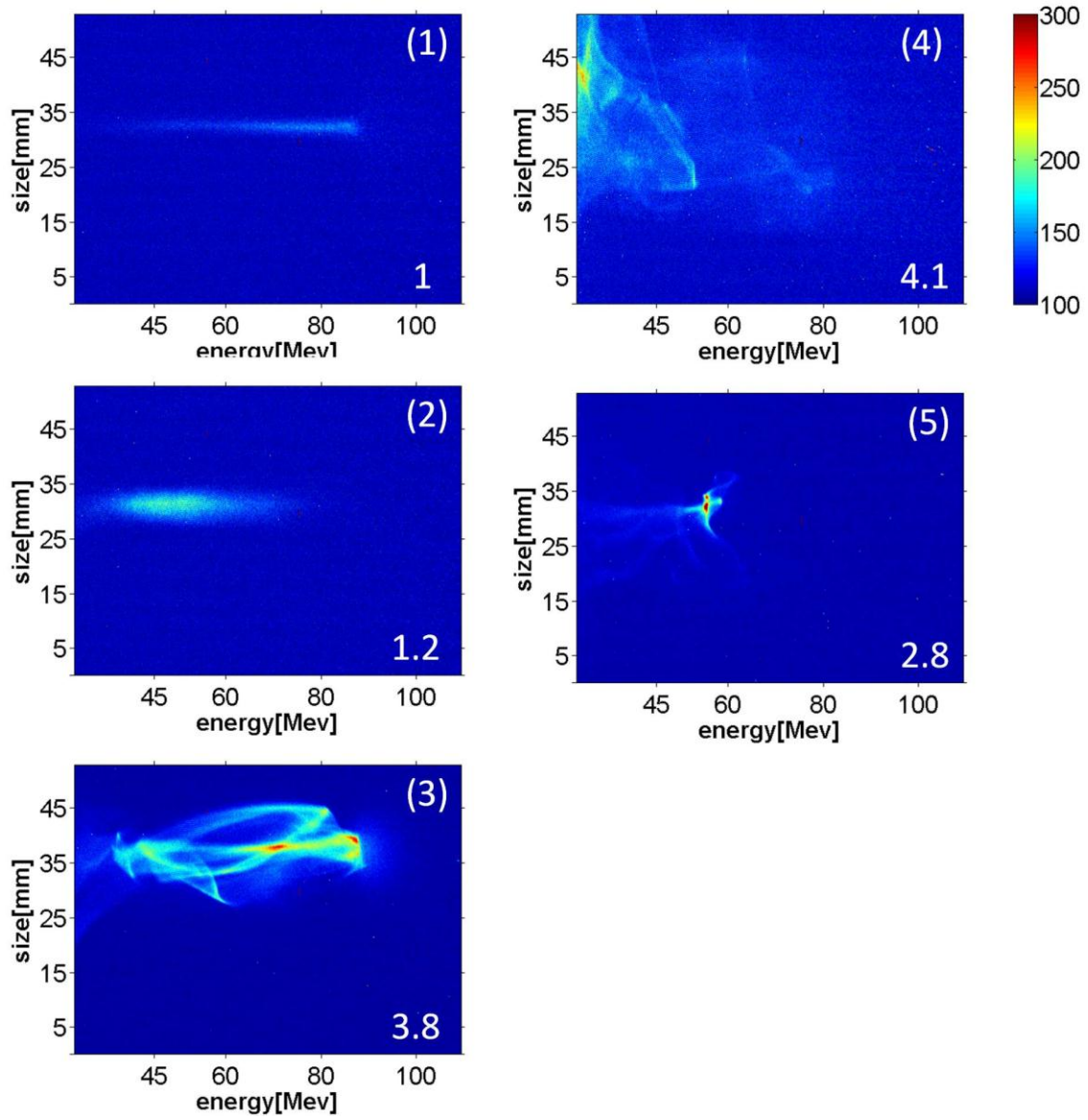


Figure 3-3. False-color images of electron beam energy spectrum at different electron densities. (1) $1.7 \times 10^{19} \text{ cm}^{-3}$; (2) $2.1 \times 10^{19} \text{ cm}^{-3}$; (3) $2.4 \times 10^{19} \text{ cm}^{-3}$; (4) $2.7 \times 10^{19} \text{ cm}^{-3}$; and (5) $2.9 \times 10^{19} \text{ cm}^{-3}$. The color intensity in the panels (1), (2)

and (4) is boosted by a factor 2. The white numbers in the figures right bottom show the lanex plate counts subtracting the background noise.

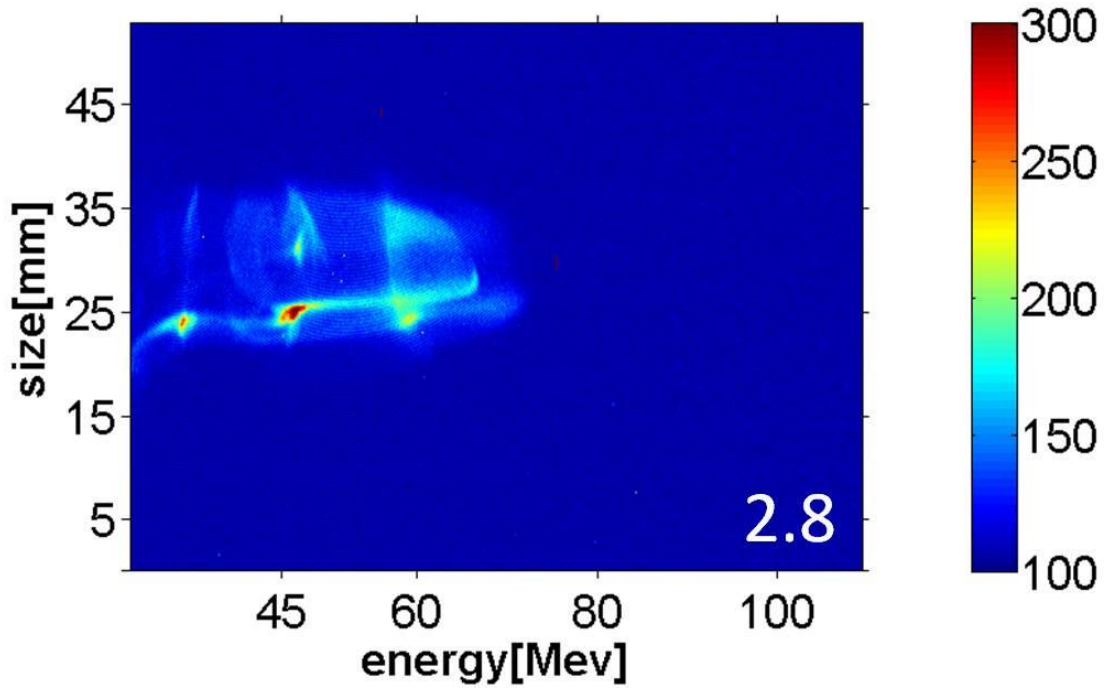


Figure 3-4. False-color images of electron beam energy spectrum at $2.0 \times 10^{19} \text{ cm}^{-3}$. The white number in the figure right bottom shows the lanex plate counts subtracting the background noise.

A theoretical scaling law predicts the peak electron energy as a function of electron density [155]:

$$E_{max} = 0.16mc^2 \frac{c\tau}{\omega_0} \left(\frac{P}{P_{rel}}\right)^{\frac{2}{3}} \left(\frac{n_c}{n_e}\right)^{\frac{1}{3}} \quad (3-1)$$

where m is the mass of electron, c is the speed of light, τ is the full width at half-maximum of the laser pulse in intensity, ω_0 is the laser frequency, P is the laser power, $P_{\text{rel}}=8.5\text{GW}$ is the natural relativistic power unit, and $n_c = m\omega_0^2/4\pi e^2$ is the critical density. The equation is strictly valid for the optimal matched laser spot size and duration at a given plasma density which, as discussed earlier, is not realized in our experiment. Nevertheless, as is seen in Figure 3-5, predictions of Equ. 3.1 fit our experiment results reasonably well. This conformity might be due to the self-focusing and compression of the pump pulse, which shrink the pump pulse focal spot and duration down to the optimal condition.

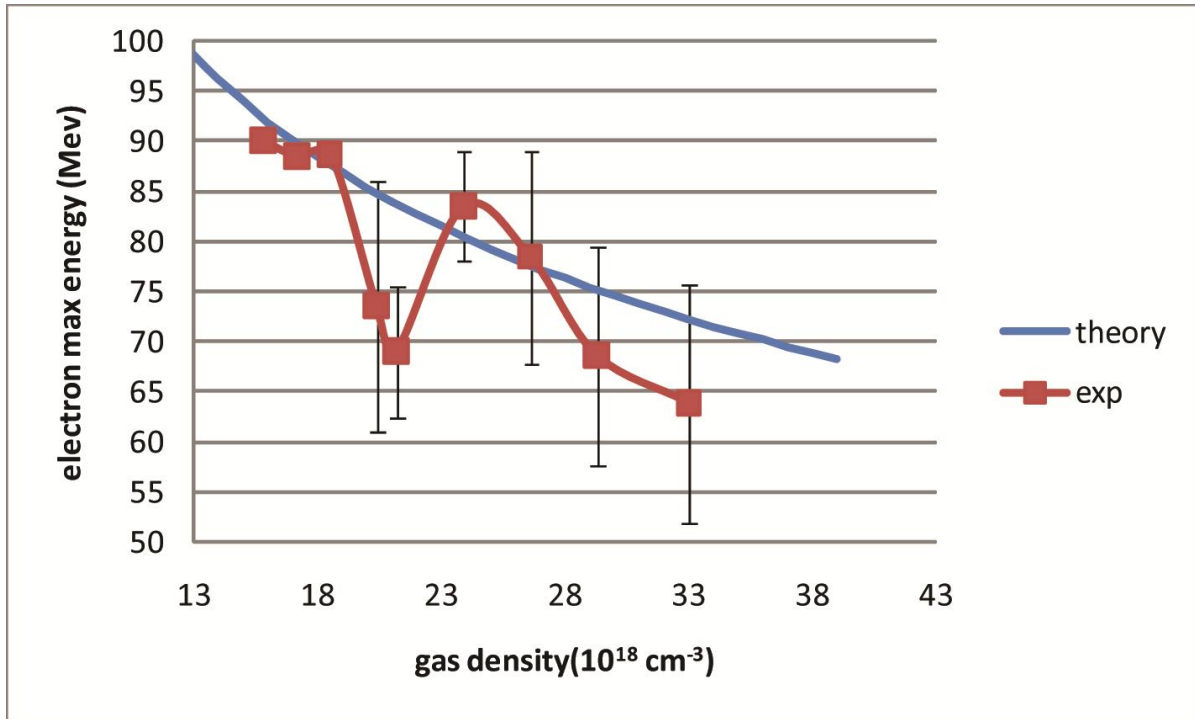


Figure 3-5 Experimental data and analytical prediction of maximum electron energy

3.5. OPTICAL BULLETS

From the FDH measurement, both the temporal amplitude and phase of the probe pulse were reconstructed. In this section, only the amplitude information is shown. Phase reconstruction will be presented in the next section.

The plasma bubble generation is represented by the formation of optical “bullets”, which is observed in the probe pulse amplitude. Plasma bubbles can reshape co-propagating probe pulses into optical bullets, which are a result of spatial focus and temporal compression. The plasma bubble has a transverse index of refraction that can guide and focus copropagating probe pulses like a lens or fiber moving at luminal velocity. The density gradient of the bubble sheath helps to modulate the probe pulse to the size of the bubble, thus compressing the probe pulse. The formation of these optical bullets resembles the controlled guiding of weak signals by optical solitons induced in Kerr media by intense light, a phenomenon that has been widely investigated as a potential basis of future all-optical processing networks [156].

The formation of optical bullets was clearly observed in the experiment. Figure 3-6 shows the spectral phase of the probe pulse at the position of an optical bullet and away from the bullet. At the position of bullet, the phase is linear, which means the pulse is fully compressed. Away from the bullet, the phase is quadratic, which is due to the original chirping of the probe pulse. Figure 3-7 shows the focusing of the probe pulse by the plasma bubble. Without plasma, that probe pulse has a large focal spot. With plasma, the focal spot becomes much smaller.

The probe pulse amplitude reconstruction is shown in Figure 3-8. The strongly nonlinear wakes in dense ($n_e > 10^{19} \text{cm}^{-3}$) plasma reshape the spectral envelope of the frequency domain hologram significantly (see Figure 3-8 (b)-(h), left column). For $n_e > 10^{19} \text{cm}^{-3}$, a streak appears to the red side of the incident probe spectrum along $r \approx 0$ (highlighted by brackets in Figure 3-8 (c)-(h), left column), sometimes accompanied by a weaker extension to the blue side. Moreover, refraction distorts $|E_{\text{pr}}(r, \zeta, z)|$ from the incident profile (see Figure 3-8 (b)-(h), middle column). Moderate distortion is evident already at $n_e = 0.4 \times 10^{19} \text{cm}^{-3}$ (Figure 3-8 (b), middle), because of plasma lensing by the overall ionized gas profile. For $n_e > 0.8 \times 10^{19} \text{cm}^{-3}$, an isolated bright spatiotemporal bullet with peak amplitude as high as or higher than the incident probe at that location forms near the probe is leading edge at the same r as the red-shifted streak (Figure 3-8 (c)-(h), middle, highlighted by vertical arrows) and is a persistent feature of all shots above this density threshold. The spectral phase along this same r (Figure 3-6) is nearly flat, signifying that the bullet is a fully compressed pulse, analogous to spatiotemporal solitons in Kerr media. For $0.8 < n_e < 1.2 \times 10^{19} \text{cm}^{-3}$ no relativistic electrons are produced (Figure 3-8 (c),(d), labeled Regime I), but for $n_e < 1.2 \times 10^{19} \text{cm}^{-3}$, the bullet appears, with varying brightness and size, together with relativistic electrons, either poly- (Figure 3-8 (e),(f), right, labeled Regime II) or quasi-monoenergetic (Figure 3-8 (g)-(h) right, Regime III). Simultaneously a fringe of probe light outlines ionization fronts (see, for example, the horizontal arrows in Figure 3-8 (c), middle).

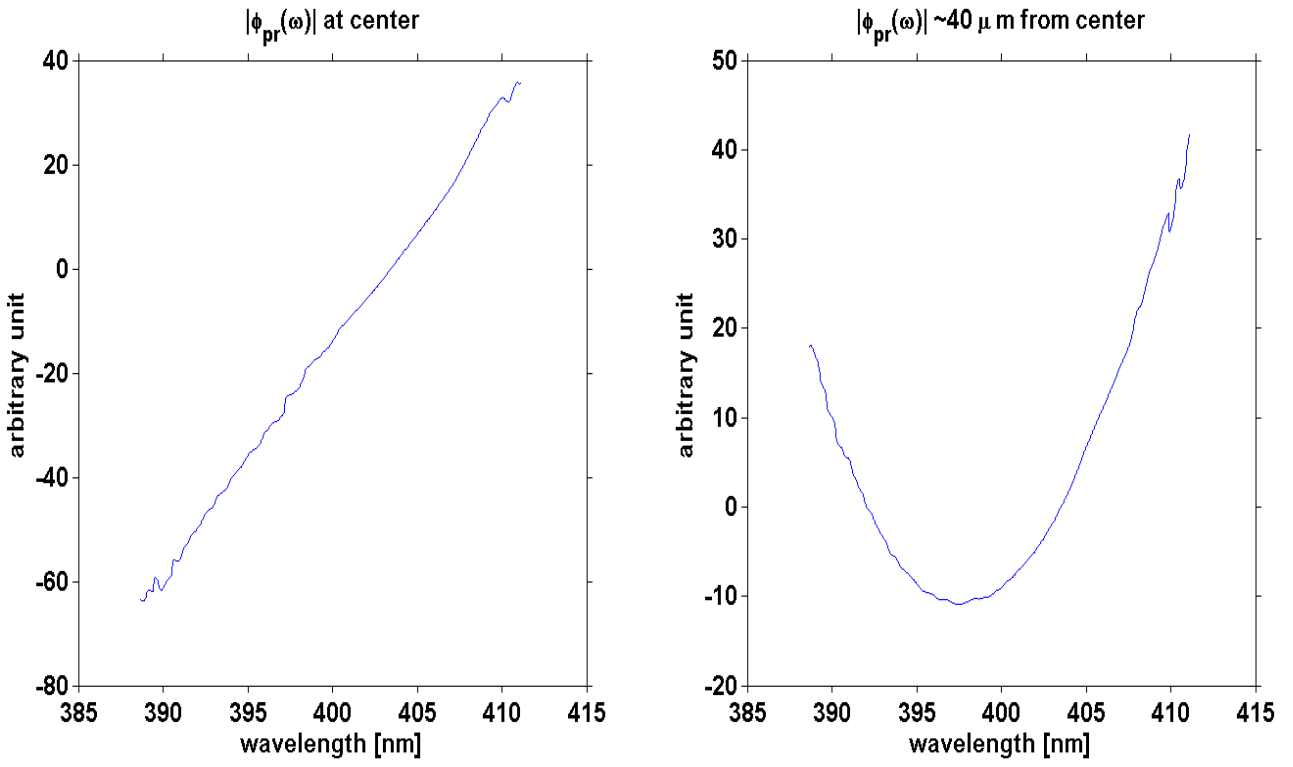


Figure 3-6. $\phi(r, \omega)$ at $r=0 \mu\text{ m}$ (left) and $\phi(r, \omega)$ at $r=40 \mu\text{ m}$ (right).

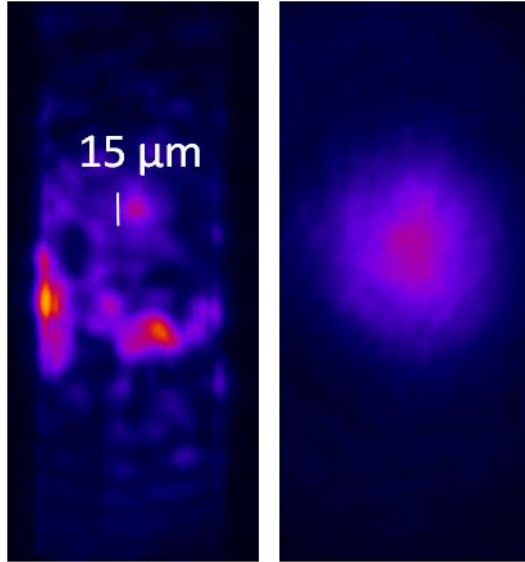


Figure 3-7. Left: Probe pulse focal spot in plasma (pump pulse unblocked). Right: Probe pulse focal spot in vacuum

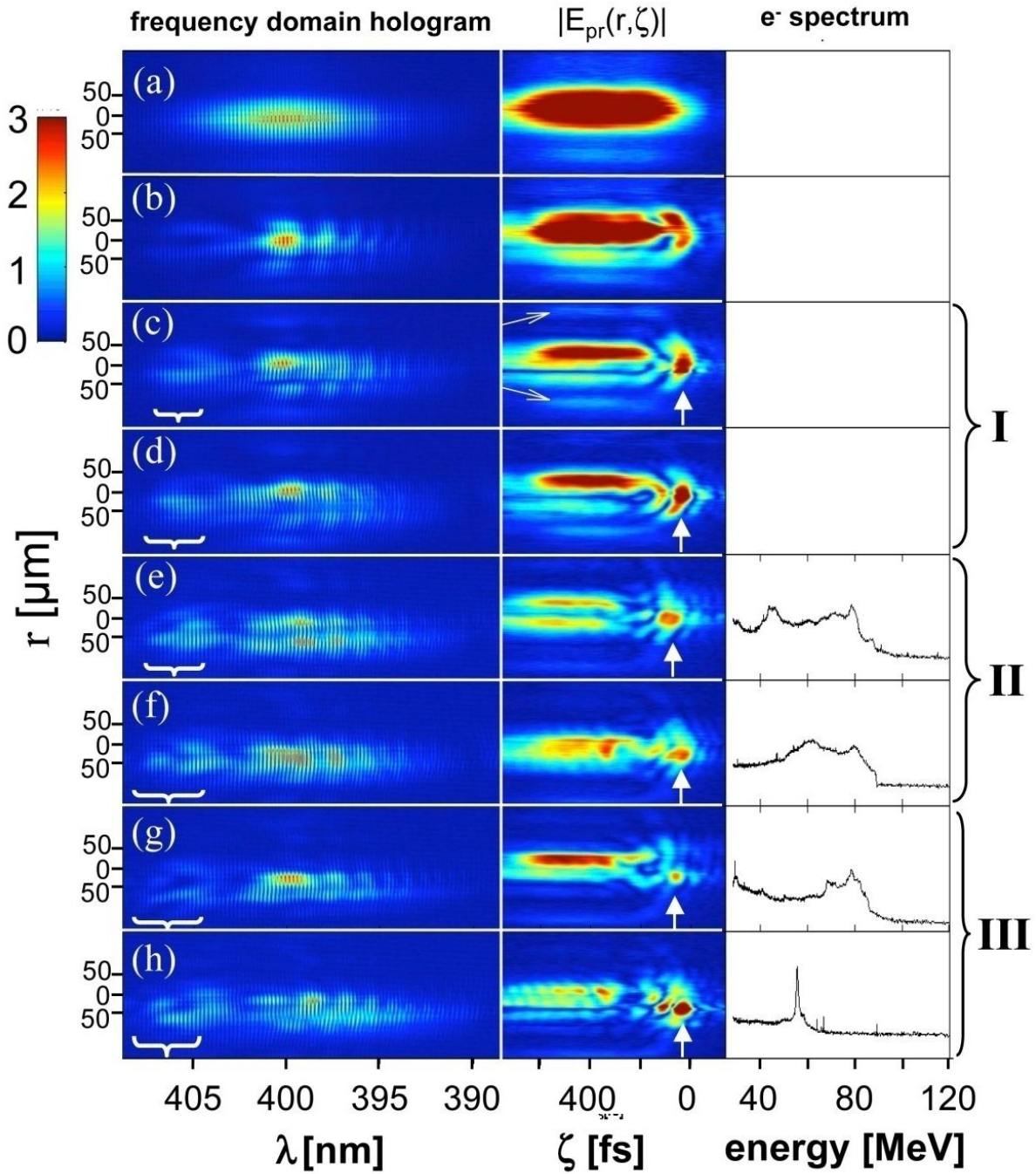


Figure 3-8 Left column: Spectral interferograms at various plasma densities showing Stokes shifted streak near $r \approx 0$ (highlighted by brackets). Middle column:

reconstructed exit probe amplitude profiles, showing distortion compared to (a), including, for (c)-(h) optical bullets (see vertical arrows) near the front edge and fringe outlining the ionization front (*e.g.*, horizontal arrows in (c)). Right column: energy spectrum of electrons produced, showing either (I) no, (II) polyenergetic, or (III) quasi-monoenergetic electrons. Plasma density n_e [10^{19}cm^{-3}] in each row was (a) 0; (b) 0.4; (c) 1.0; (d) 1.2; (e) 2.6; (f) 2.6; (g) 2.6; (h) 3.2 in the doubly-ionized He region.

To understand bullet formation qualitatively, we can regard a pump-generated plasma bubble of radius $R_b = 2c\sqrt{a_0}/\omega_p$ as an optical cavity with internal transverse refractive index profile $\eta_p(r) = 1 - \omega_p^2(r)/2\omega_{pr}^2$ that copropagates with the probe, where $\omega_p^2(r) = n_e(r)e^2/\varepsilon_0 m_e$ is the local plasma frequency. Since η is the maximum on the axis, such a cavity focuses the probe light originally inside the bubble to spot size σ_{bullet} over a distance $f = \pi\sigma_{\text{bullet}}^2/\lambda_{\text{pr}}$. For rough estimates, we assume a parabolic density profile $n_e(r) = n_e r^2/R_b^2$ inside the bubble, self-focused/compressed pump intensity $a_0 \approx 5$, and $n_e \approx 10^{19}\text{cm}^{-3}$, which yields $R_b \approx 7.5 \mu\text{m}$, $\sigma_{\text{bullet}} = \sqrt{R_b\lambda_p/2\pi} \approx 3.5 \mu\text{m}$, and $f \approx 0.1\text{mm}$. Since $f \ll z_{\text{exit}} \approx 2\text{mm}$, a plasma bubble focuses the probe light during jet transit. As a corollary, $\Delta\phi_{\text{pr}}(r, \zeta, z)$ scrambles radially. As a result, reconstructed $\Delta\phi_{\text{pr}}(r, \zeta, z_{\text{exit}})$ profiles become extremely complicated and are no longer simply related to plasma structure as at lower n_e [80]. The profiles will be discussed in Sec. 3.7. Here, we focus instead on $|E_{\text{pr}}(r, \zeta, z_{\text{exit}})|$ profiles, which can be more simply interpreted and are analogous to shadowgraphs projected on a virtual screen at z_{exit} . We call extraction of plasma information from such profiles FD shadowgraphy (FDS).

3.6. SIMULATION OF PLASMA BUBBLE AND OPTICAL BULLET FORMATION

To understand bullet formation quantitatively, we simulated ionization, nonlinear wake generation and copropagation of a 400 nm probe pulse (shortened to ~ 100 fs, centered on the first wake bucket) using the fully relativistic, quasistatic time-averaged particle-in-cell (PIC) code WAKE [157] in an axisymmetric geometry, using profile $n_e(z)$ from transverse interferometry. It should be noted here that the WAKE code does not include the effects of electron acceleration and loading. For the experiment to be fully simulated, a fully 3D PIC code is essential; however, fully 3-D codes are very time consuming, requiring days to finish one run. The WAKE code, on the other hand, is fast and includes all the essential physics when the electrons are not trapped. (All simulations were performed by A. Yi, S. Kalmykov and G. Shvets, with my input of initial experimental conditions).

Figure 3-9 shows the pump intensity profile $|a_{pu}(r, \zeta, z)|^2$ (top row), density profile $n_e(r, \zeta, z)$ (second row), and normalized probe intensity profile (third row) at $z=0.1$ (left column), $z = 0.5$ mm (center column), and $z=1.8$ mm (right column) for peak density $n_e = 0.8 \times 10^{19} \text{ cm}^{-3}$, for which the bubble guides the pump over a nonlinear pump depletion length $L_{pd} \approx \omega_0^2 / \omega p^2 (c\tau) \approx 1.8$ mm limited by the erosion of its leading edge. At $z=0.1$, the pump and probe retain their incident Gaussian spatial-temporal profiles as a plasma wake forms. By $z=0.5$ mm, the pump compresses to $\tau_{pu} \approx 20$ fs, doubling its peak intensity; ionization fronts outline the He^+ fringe and He^{2+} core regions; and electrons are blown out almost completely from the first wake bucket. Simultaneously, the probe is strongly distorted, becoming focused and compressed pulse ~ 5 times as intense as the incident probe forming within the first wake bucket, as the surrounding

regions darken, except for a residual fringe outlining the ionization fronts. This effect shows that the bubble efficiently traps probe light from surrounding regions, which is consistent with the qualitative picture of a moving spherical lens.

At $z = 1.8 \text{ mm} \approx z_{\text{exit}}$ the pump remains guided, although eroded to ~ 5 fs duration consistent with the estimated L_{pd} , while the probe light remains trapped inside the bubble, where it is compressed into micropulses as short as ~ 10 fs. The simulated frequency domain hologram of the exiting probe (Figure 3-9, bottom left) features a frequency-broadened streak centered at $r = 0$ that corresponds to probe light trapped inside the bubble. The probe amplitude profile at z_{exit} is reconstructed using the same reference bandwidth ($\Delta \lambda \approx 10 \text{ nm}$) and imaging resolution ($\sim 10 \mu \text{ m}$) as those of the experiments (Figure 3-9, bottom right) and thus preserves the main features of the exiting probe with degraded resolution. Simulations at higher n_e show that, in principle, the bullet shrinks as $\lambda_p \sim n_e^{-1/2}$ in proportion to the final size of the bubble, but its observed size was limited by optical resolution.

Wake and probe pulse evolutions in Regime II and III were simulated with VLPL [158] to account for electron injection and beam loading. Figure 3-10 (a)-(c) show bubble evolution in fully ionized plasma of $n_e = 2.3 \times 10^{19} \text{ cm}^{-3}$, while Figure 3-10 (e)-(g) show the corresponding evolution of probe pulse amplitude. By $z = 0.56 \text{ mm}$, a bubble (Figure 3-10(a)) and an optical bullet spanning the bubble's length have formed. Trailing wake buckets also trap probe light. By $z = 0.92 \text{ mm}$, massive self-injection fills the rear of the bubble with a dense electron bunch (see Figure 3-10(b)). Electrons' space-charge force prevents the bubble from closing [159]. The trailing periodic wake then collapses, and the only persistent probe feature becomes an optical bullet focused in

the first bucket (Figure 3-10(f)). Probe features trailing the first bucket are intermittent and time-average to negligible amplitude. By $z = 1.56$ mm, the pump is depleted, and the bubble, now driven primarily by electrons, nearly triples in volume (Figure 3-10(c)). The optical bullet outruns the bubble and starts diffracting (Figure 3-10(g)), which may explain the formation of multiple red-shifted streaks in Figure 3-8(e)-(g).

Several conclusions about bullets emerge from the combined simulations. First, the bullet forms in the first bucket before electron self-injection starts (Figure 3-10(e)) and thus outruns the electron bunch, and the bullet is unaffected by the bubble elongation caused by beam loading. The bullet's length thus replicates the bubble's length early in the jet (although probe bandwidth limits its measured length to ~ 30 fs), and its width is the blowout region width (although it appears broader because of limited imaging resolution and diffraction from the front of the bubble before $z = z_{\text{exit}}$), as seen from comparing Figure 3-10(g) and (h). Thus the bullet “remembers” the bubble's shape shortly after it is formed. Second, the bullet interacts primarily with the bubble's quasi-static front end, which both simulation codes model accurately. WAKE simulations with the same input parameters used for Figure 3-10 yield bullet evolutions similar to those in the 3D VLPL results, despite very different evolutions of the bubble tail. Third, the simulations show that the bubble's front end is much less sensitive to changing laser-plasma conditions than its dynamic back end. This difference accounts for the shot-to-shot stability of the bullet size and shape evident in the middle column of Figure 3-8(c)-(h), even while the corresponding electron spectra vary widely. Quasi-monoenergetic electron spectra, as shown in Figure 3-8(g) and simulated in Figure 3-10(d), are common in Regime II, whereas highly mono-energetic spectra, such as that in Figure 3-8(h), were observed occasionally, but never reproduced in 2 mm-long VLPL simulations. Such

features with an $\sim 1\%$ energy spread have been reported previously in this n_e range [160],[161]. In our case, they may result from occasional perturbations in the gas jet profile or pre-pulse excitations that cause the pump to focus near the jet exit, reducing the effective interaction length to below L_{pd} .

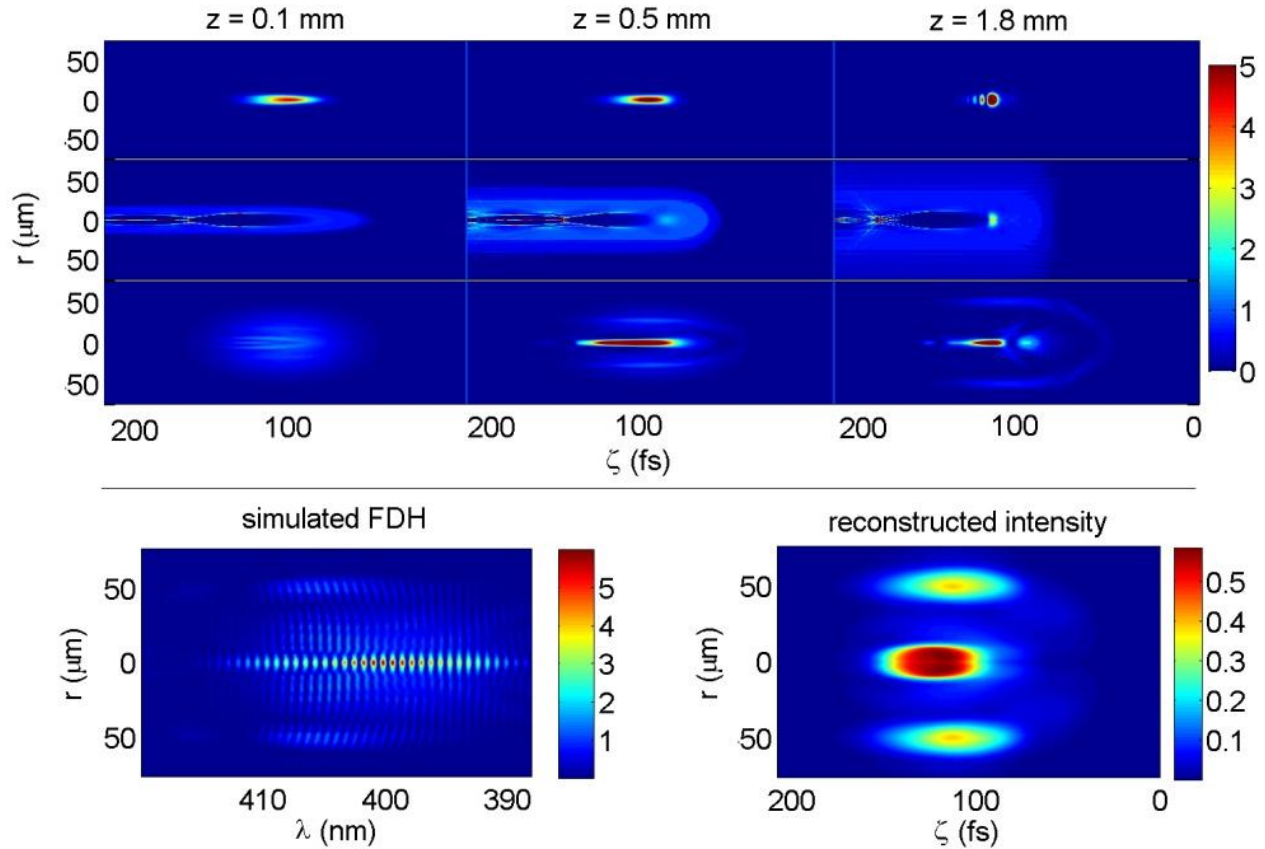


Figure 3-9 WAKE simulations of 800 nm pump (top row), plasma wake (second row), and 400 nm, 100 fs probe (third row) near gas jet entrance (left column), at $z = 0.5$ mm (middle column), and near z_{exit} (right column), showing self-compression of the pump, and strongly refracted probe profile featuring an optical bullet trapped inside the bubble and fringe outlining the ionization front. Pump and probe propagate from left to right. Bottom left: simulated FD hologram shows frequency-broadened streak at $r=0$ corresponding to a bullet inside the bubble. Bottom right: Probe intensity profile reconstructed from FD hologram using experimental reference

bandwidth and imaging resolution. Vertical arrow: Bullet; horizontal arrows: Ionization front.

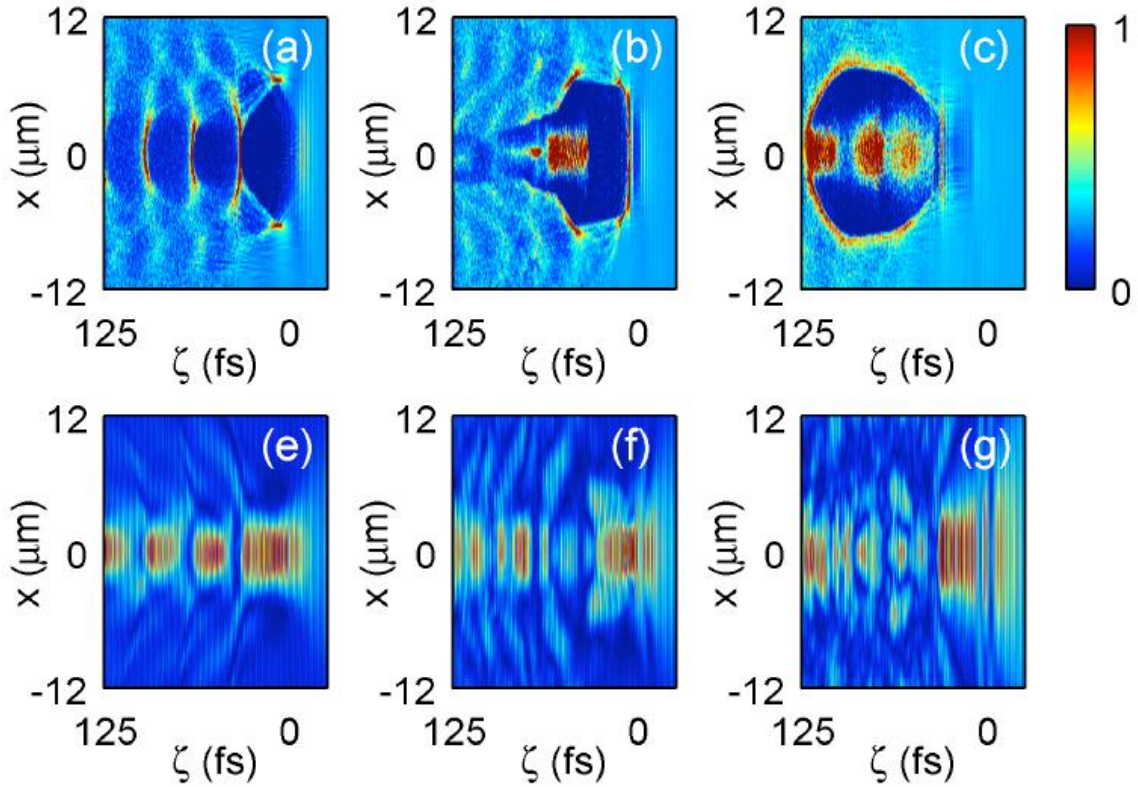


Figure 3-10. VLPL simulations for $n_e = 2.3 \times 10^{19} \text{ cm}^{-3}$. Panels (a)-(c): Plots of electron density showing formation of bubble, injection of electrons ((b) and (c)) at $z = 0.56 \text{ mm}$ (left), 0.92 mm (2nd column), and 1.56 mm (3rd column); Panels (e)-(g): Plots of $|E_{\text{pr}}(r, \zeta, z)$ of the probe at same z values, showing optical bullet formation. Panel (d): Accelerated electron spectrum at $z = 1.56 \text{ mm}$, showing quasi-monoenergetic feature at 90 MeV .

3.7. COMPARISON OF PHASE AND AMPLITUDE RECONSTRUCTION

For some of the FDH phase reconstruction, 2-D phase unwrapping helps to obtain a phase map free of artifacts and sharp discontinuities. Figure 3-11 (a) and (c) show the phase reconstruction with 1-D and 2-D phase unwrapping, respectively, of the same probe pulse shown in Figure 3-8 (d). (a) and (c). At $1.0 \times 10^{19}/\text{cm}^3$, a bubble structure appears at the front of the probe pulse (signified by the black circle in Fig. 3-11 (c)). At a density of $2.4 \times 10^{19}/\text{cm}^3$, on the other hand, the phase snapshot is totally unreadable because of the large amount of phase discontinuities (see Fig. 3-11 (b)). The 2-D phase unwrapping does help to clean the picture and delineates a phase shift column along propagation axis of the probe pulse (see Fig 3-11 (d)). This column may result from the plasma chaotic movement after the plasma bubble passed through.

The bullet outrunning the bubble structure is also observed in the experiment. From Fig. 3-12, the optical bullet (top row) is clearly in front of the bubble structure, which is visible in the probe pulse phase (bottom row). The time difference does not agree with the simulation. There might be several reasons for this. One is the Group velocity difference between the pump pulse and the probe pulse, which is ~ 15 fs at $1 \times 10^{19}/\text{cm}^3$. However, the complicated density profile of the plasma bubble might also enlarge the time. The bubble also slowed due to beam loading and pumps depletion [58]. The temporal walk-off of optical bullet from plasma bubble is an effect that deserves more systematic study in the future work.

Apparently corresponding to the bubble structure in the probe phase reconstruction are bubble-shaped lines in the probe amplitude. Those lines may signify the edges of the plasma bubble (see Fig. 3-12). At $\sim 1.1 \times 10^{19}/\text{cm}^3$, the same density at

which optical bullets (and, by inference, plasma bubble) those line structures start to appear and remain stable from shot to shot, like optical bullets, though their shapes vary (Fig. 3-13). Figure 3-14 shows a lineout of the bubble feature taken from Figure 3-12. The front of the lineout is round, and the rear part extends to the outside. This feature is similar to the shape that what Lu *et al.* described in [57] regarding a bubble sheath in the ultra relativistic blowout regime. Those line formations can be explained in two ways. First, the amplitude is modulated by the plasma density variation. When the probe pulse phase has a sharp jump, the index of refraction is also increasing abruptly. Similarly to optical inhomogeneities in space, light rays bend in proportion to the gradient of refractive index; thus $\frac{\partial^2 x}{\partial z^2} = \frac{1}{n} \frac{\partial n}{\partial x}$, where x is the deflection distance, z is the pulse propagation distance, n is the index of refraction. We have $\alpha = \frac{\partial x}{\partial z} = \frac{1}{n_e} \int \frac{\partial n_e}{\partial x} dz$, where α is the deflection angle. The angle deflection is equal to the integral of the index of refraction gradient in the position on the probe pulse profile. Therefore, any place with a sharp phase change will also have an amplitude drop.

Second, due to the limited bandwidth of the probe pulse, a sharp phase jump will cause an apparent dip in the reconstructed probe pulse amplitude. A simple mathematical model can be built to prove the second point. The ionization front is represented by a sign function in the phase of the electric field. The amplitude of the probe pulse has a smooth Gaussian shape (Figure 3-15). When the bandwidth of the pulse is infinite, a perfect reconstruction of the phase and amplitude is expected

and observed in the simulation. However, as the bandwidth of the pulse is limited to 24 nm at FWHM, the hard edge of the phase is softened and stretched to ~22 fs, which is the transform-limited pulse duration for the 24 nm pulse (

Figure 3-16). The Gaussian-shaped amplitude damps with several dips, which are at the same positions as the phase jumps. The dip height depends on the slope of the phase jump. For a phase jump shorter than the probe pulse duration, the attenuated phase jump is equal to the transform limited pulse duration of the pulse. Thus, the higher the phase jump, the greater the slope and the deeper the dip in amplitude. For bubble structures such as the thin bubble sheath, the thickness is normally less than that of the probe pulse. In an ideal case where the pulse amplitude is not affected by the bubble, we can suppose that the dip height in the amplitude will inform us the electron density in the thin sheath.

Thus, the line features behind the optical bullet do not give us plasma density; rather, they show us the location with the highest density gradients. In most case, that is what researchers are interested in.

Here I will show three more interesting FDS reconstructions with the line features and offer tentative explanations. Figure 3-17, a snapshot before the bubble onset at $1.1 \times 10^{19}/\text{cm}^3$, shows a dark line all the way to the end of the probe profile. A hook appeared in the front of this channel. The bubble is not stably formed; however, an optical bullet has formed in the front, which means the bubble has already begun to trap probe light. Some snapshots show complicated plasma structures that do not show up in the

simulation, as shown in Figure 3-18. Line features show up, that are similar to those appearing at low densities. Here, a line does not complete a circle as does a bubble. Rather, the black line has a fork shapes that radiates outward. Those shapes might be what remains after the bubble breaks up. Figure 3-19 shows a typical snapshot showing an optical bullet in the front, a dark, apparently bubble-related structure, and a channel structure with an electron beam detected. The bubble feature is smaller than that in Figure 3-13, partly because of the higher density and partly because of the trapping of the electrons. More systematic study of these dark features in FDS reconstructions will be part of future work.

3.8. CONCLUSIONS

In this chapter, I discussed how to adapt the FDs technique from the linear plasma wakefield (low plasma density) regime to FDS/FDH in the plasma bubble regime (high density). The formation of the optical bullets is observed for the first time. Bubble generation below the electron trapping threshold is also observed for the first time. The fact that the optical bullet outruns the plasma bubble should give us more insight into the acceleration process. The dark features behind the optical bullet in probe amplitude reconstructions also show variations with the plasma density.

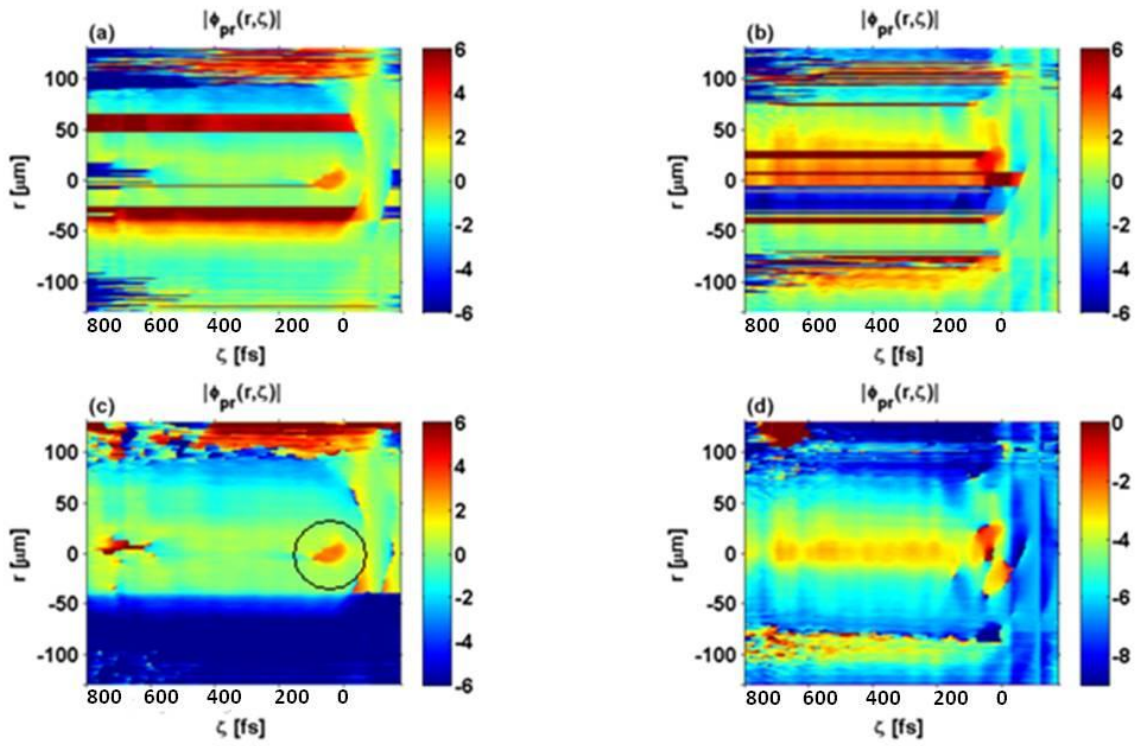


Figure 3-11. 1-D and 2-D phase unwrapping of the phase data. (a) and (c) FDH snapshot $\phi(r, \zeta)$ at $1.2 \times 10^{19} / \text{cm}^{-3}$ for the same shot as shown in Figure 3-8 (d). (a) using 1-D and (c) 2-D phase unwrapping respectively; (b) 1-D and (d) 2-D phase unwrapping FDH snapshot $\phi(r, \zeta)$ at $2.4 \times 10^{19} / \text{cm}^{-3}$.

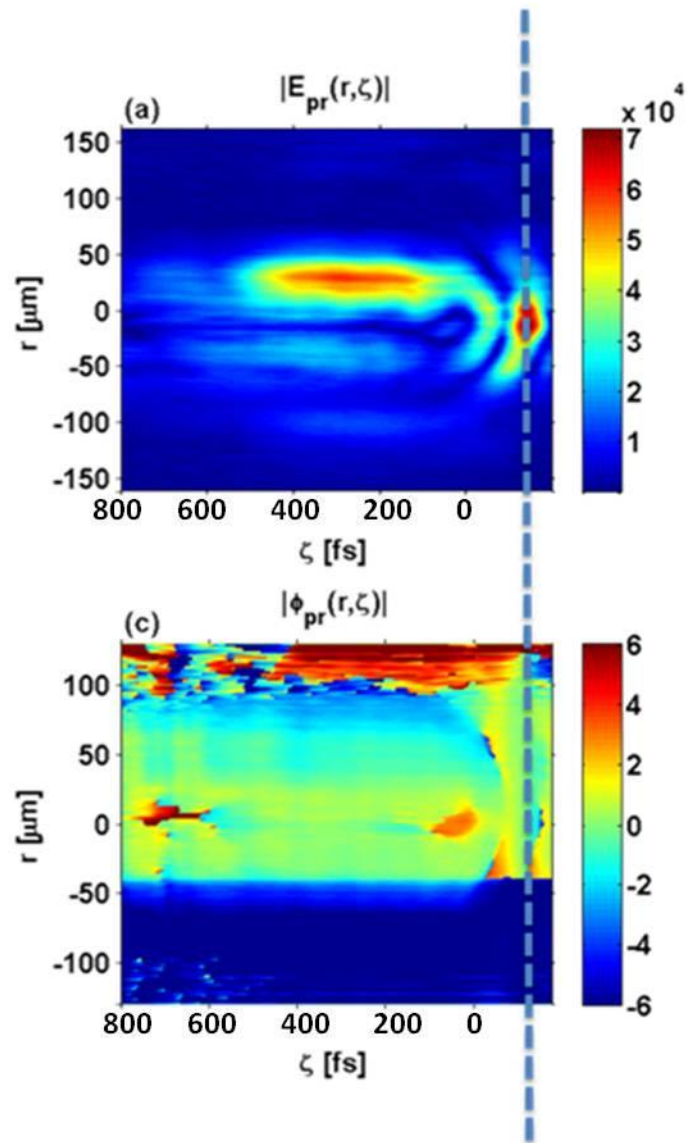


Figure 3-12. Optical bullets outrunning the plasma bubble. Top row: Probe pulse amplitude reconstruction. Bottom row: Probe pulse phase reconstruction.

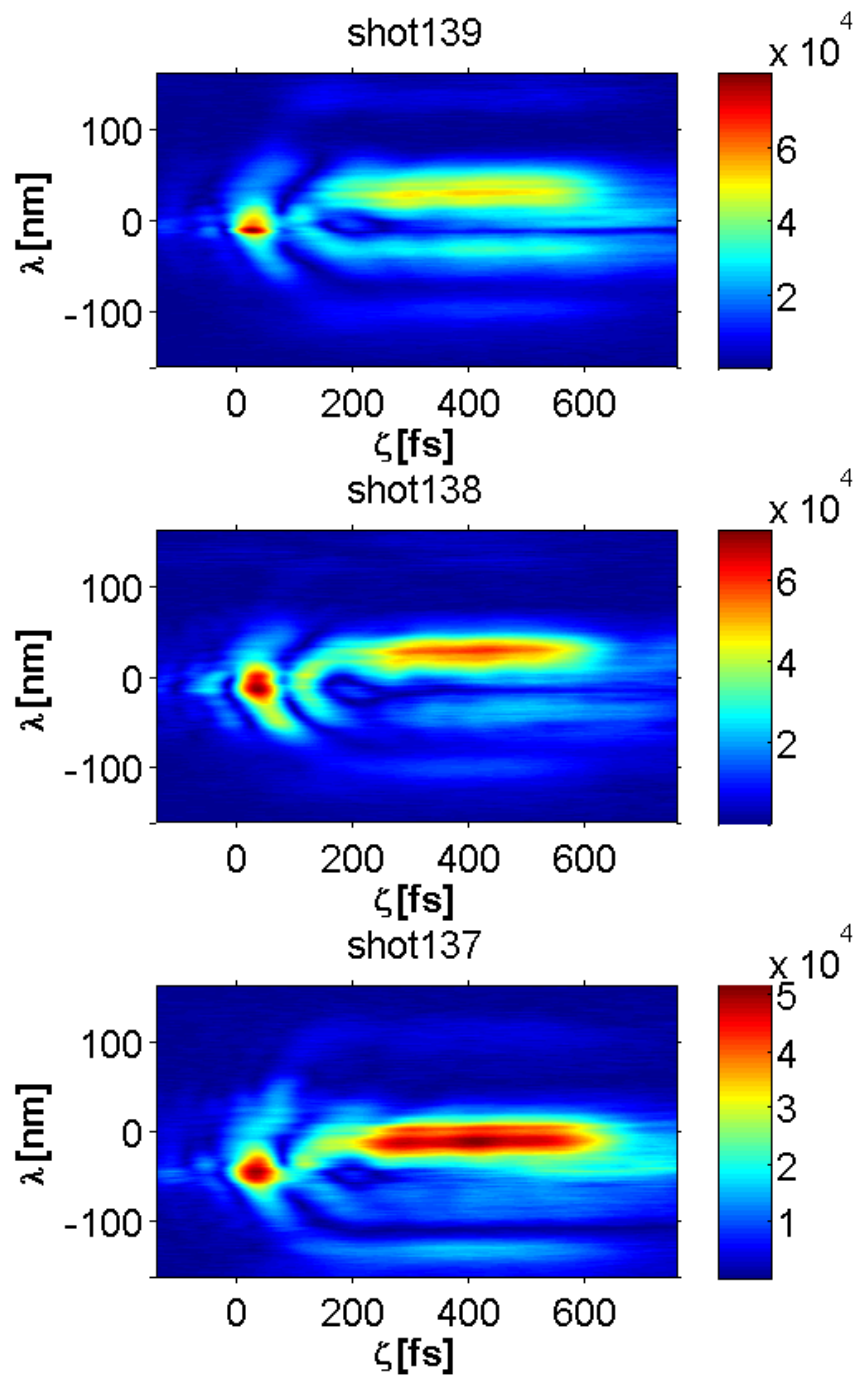


Figure 3-13. Bubble-shaped structure at $1 \times 10^{19}/\text{cm}^3$.

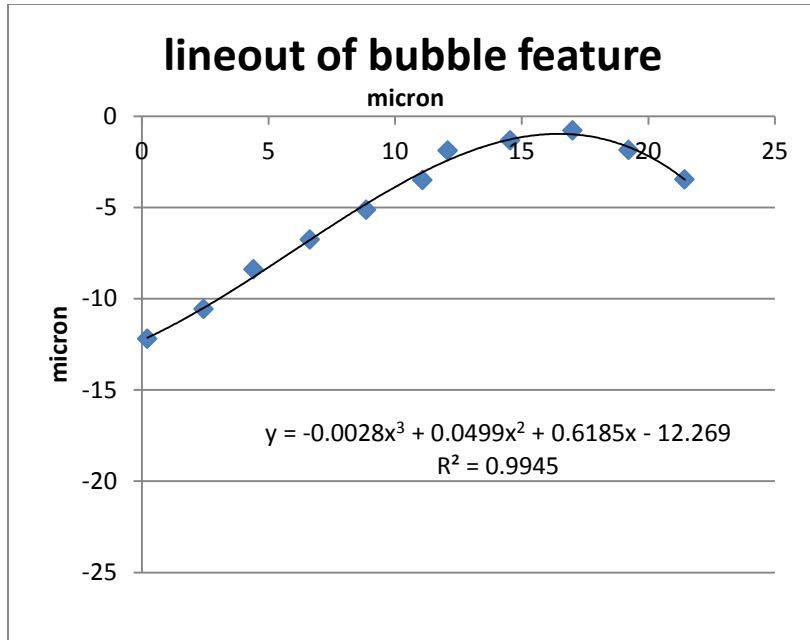


Figure 3-14 Lineout of the bubble feature taken from the line features in the Figure 3-12.

The solid line is a polynomial fitting.

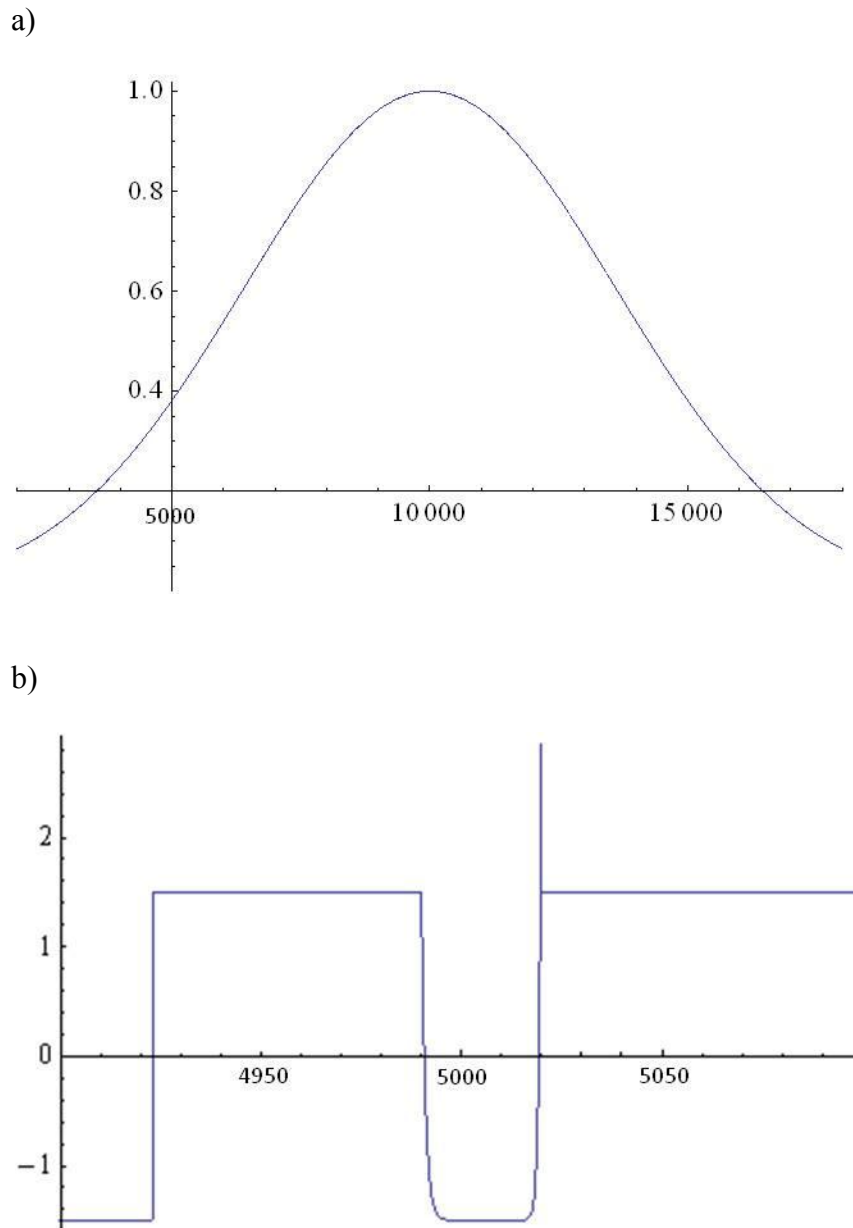
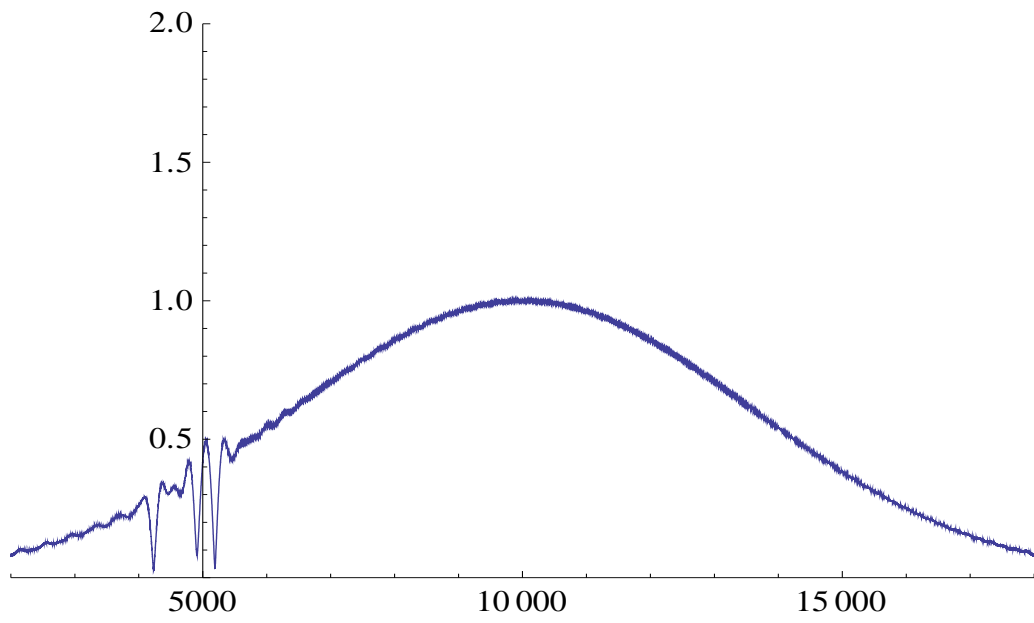


Figure 3-15. Probe pulse amplitude (a) and phase (b) The unit for the horizontal axis is 0.1 fs. The jump at 492.5 fs represents the ionization front. The drop from 499 fs to 502 fs represents the bubble.

a)



b)

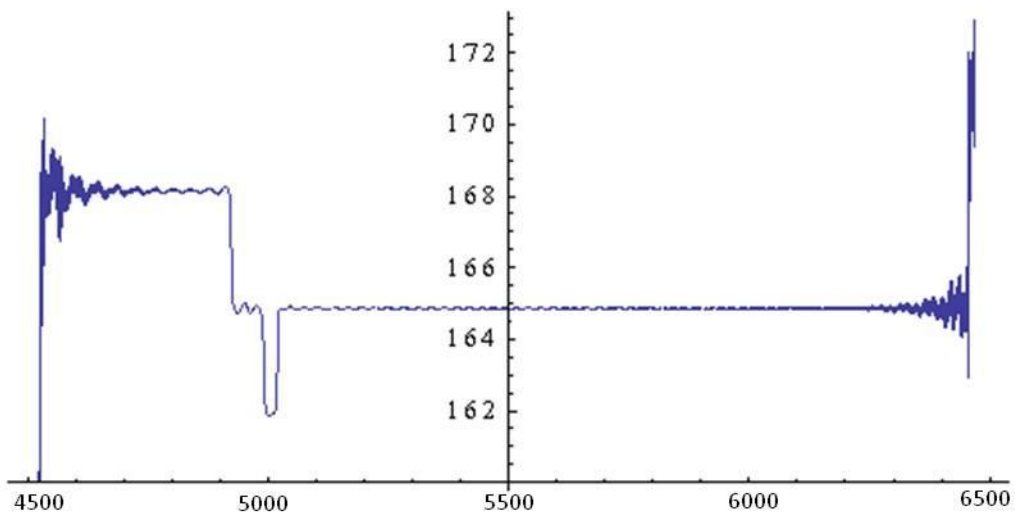


Figure 3-16. Probe pulse reconstruction with limited bandwidth 380nm to 420nm. (a) is amplitude, and b) is phase. The unit for the horizontal axis is 0.1 fs.

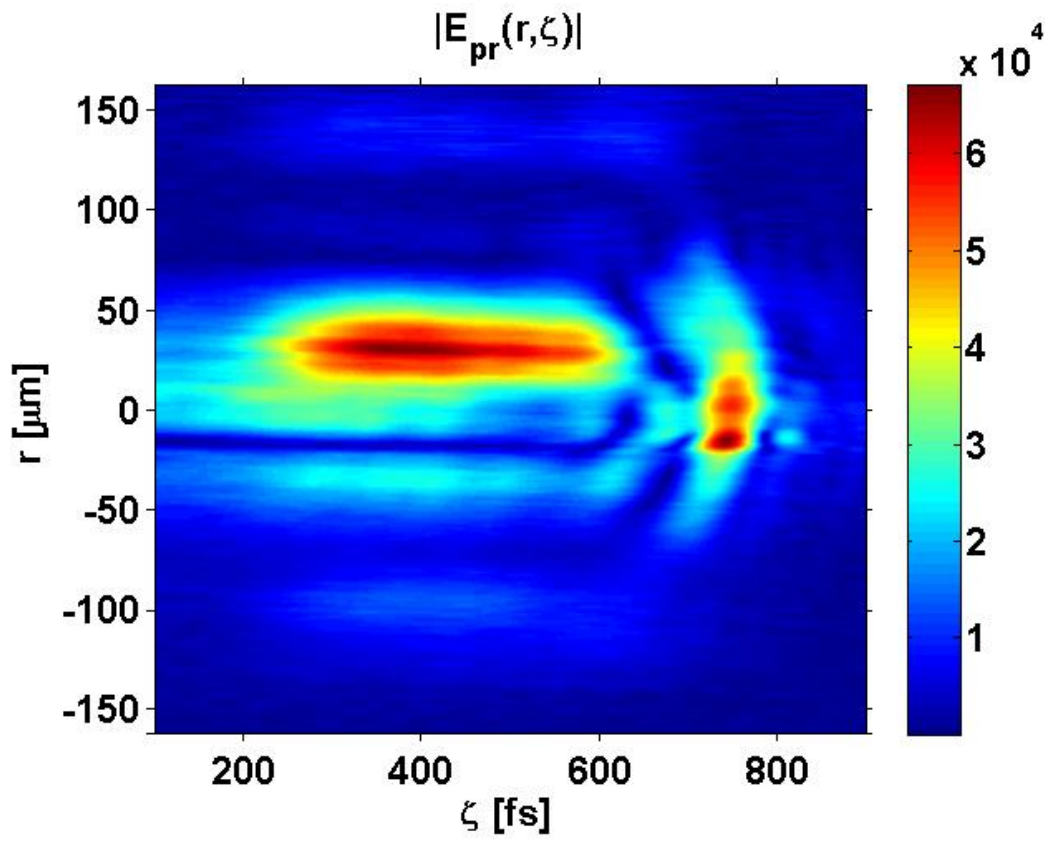


Figure 3-17. The FDS snapshot before the bubble formation ($1.1 \times 10^{19}/\text{cm}^3$)

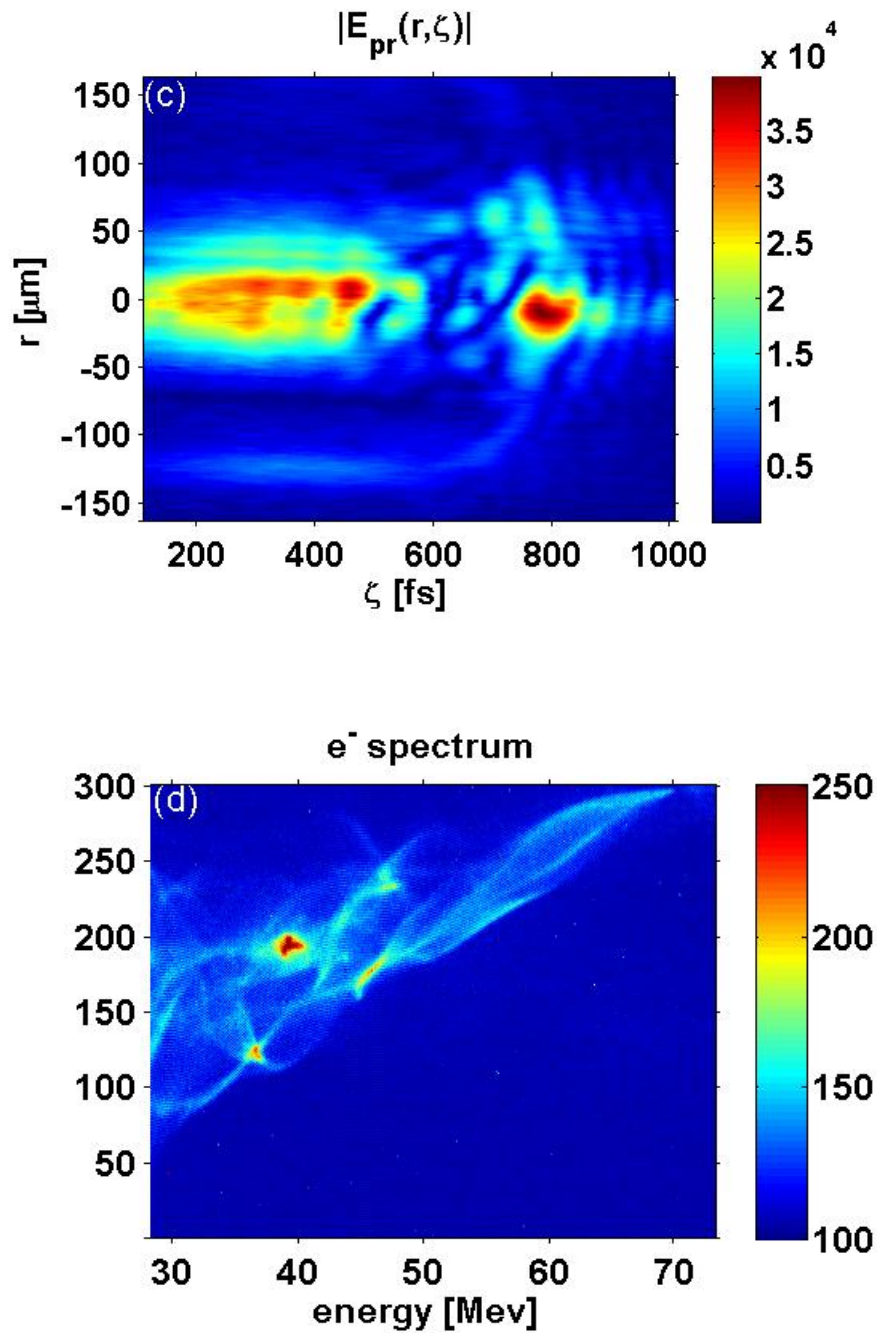


Figure 3-18. Typical FDS snapshot with complicated black line feature and corresponding electron beams ($2.4 \times 10^{19}/\text{cm}^3$).

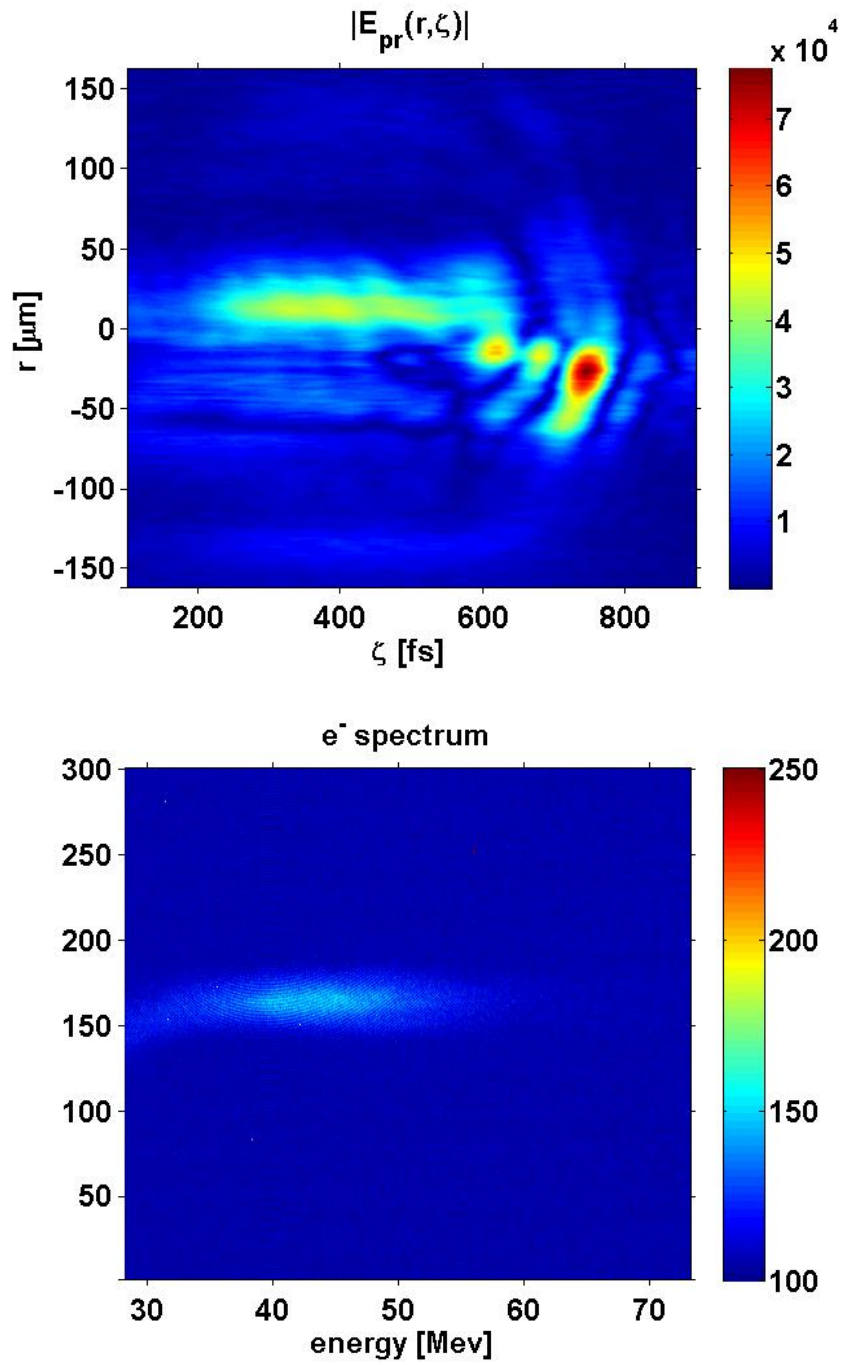


Figure 3-19. A typical snapshot showing an optical bullet in the front, black line bubble structure, and channel structure with electron beam measured ($2.1 \times 10^{19}/\text{cm}^3$).

Chapter 4. Visualization of evolving laser wakefields: frequency-domain tomography

This chapter discusses an extension of the FDH/FDS technique — noncollinear FDH. The collinear FDH/FDS setup is prone to pollution by pump-generated white light and SHG, as discussed in Sec. 3.1. Collinear FDH gives an averaged measurement of the plasma structure without resolving its evolution during transit through the plasma. By introducing a noncollinear FDH setup, we gain the opportunity to time resolve the changing plasma structure. With multiple noncollinear FDH beams, a complete 3-D evolving plasma object can, in principle, be reconstructed in a single shot using tomographic back-projection algorithms similar to those used in medical CAT scan [162]. In this chapter, I carry out a preliminary evaluation of this feasibility and limitations of this Frequency-Domain Tomography (FDT) concept.

4.1. CONCEPT OF FREQUENCY DOMAIN TOMOGRAPHY

A limitation of FDH is that longitudinal variations of the accelerating structure are averaged as the drive pulse propagates through the plasma. Specifically, with the plasma structure expressed as an instantaneous electron density profile $n_e(r, \zeta, z)$ and the corresponding local index of refraction expressed as $\eta(r, \zeta, z)$, the phase change imprinted on the probe pulse is the integral $\Delta\phi(r, \zeta) = \frac{2\pi}{\lambda_{pr}} \int_0^L [1 - \eta(r, \zeta, z)] dz$. Here, as in previous chapters, r denotes distance from the drive pulse propagation axis, ζ is distance behind the drive pulse, and z is the propagation distance from the gas jet entrance, and we have assumed for simplicity that the wake is cylindrically symmetric. Many kinds of longitudinal (z) variations can cause the holographically reconstructed $\Delta\phi(r, \zeta)$ to deviate from the actual plasma wakefield shapes $n_e(r, \zeta, z)$: laser focusing and defocusing, gas jet

density variation, wave breaking, and beam loading. In the bubble regime, this is especially serious because bubbles can form rapidly after the self-focusing and steepening of the drive pulse. Conventional FDH averages over this temporal sequence, preserving no record of the bubble's temporal evolution.

An additional practical limitation of conventional FDH is that a forward-directed white light continuum or optical harmonics generated by the pump can interfere with the probe and reference pulses, which are typically at a different wavelength than that of the pump pulse to enable separation from the pump light. Such undesired background light inhibits image reconstruction, especially in dense plasmas where bubble structures are important. For example, in previous experiments, the white light continuum made image reconstruction impossible at plasma densities above $5.9 \times 10^{18} \text{ cm}^{-3}$. The white light is mainly restricted to the cone of the pump pulse.

4.2. SIMULATIONS OF PHASE STREAKS

We propose augmenting the collinear probe-reference pulse pair with a probe-reference pulse pair propagating at angle α to the pump. For example, Fig. 4-1 shows an oblique probe interacting with a plasma bubble, a nonlinear wake in which the first period behind the drive pulse deepens into a cavity nearly devoid of electrons, while subsequent waves collapse (see Sec. 1.3.3.5 and Chapter 3). We use a plasma bubble as an example here because of its importance in producing quasi-monoenergetic GeV-range electron beams, because my work reported in Chapter 3 provided the first direct, albeit — time-integrated, observation of bubbles in the laboratory, and because simulations show that bubbles often evolve substantially during jet transit. The phase “streak” imprinted

on the probe (Figure 4-1 (b) and (c)) chronicles the evolution of the bubble, which traverses a path across the probe pulse profile in the direction ξ shown in Figure 4-1 b. A change of bubble structure changes the width and depth of the phase streak as a function of ξ , which is recovered (Figure 4-1 c) as in conventional FDH. We therefore call this the Frequency Domain Streak Camera (FDSC). The value $\Delta\phi_{pr}(\xi)$ from a single obliquely propagating probe can help in the interpretation of a longitudinally averaged conventional FDH snapshot. Moreover, for non-zero α , transmitted pump and forward pump-generated radiation propagates away from the detection system, enabling use of lower f-number, higher resolution imaging optics closer to the object than for conventional FDH and avoiding false structure in recovered images.

We simulated a phase streak for realistic experimental conditions using the particle-in-cell (PIC) code WAKE and the finite element code COMSOL. WAKE simulated the axi-symmetric wake structure generated by a pump pulse (peak intensity 9.8×10^{18} W/cm², $w_0 = 16$ μ m, 800 nm) with a Gaussian radial and temporal profile focused at the entrance to a plasma of density $n_e = 1.5 \times 10^{19}$ cm⁻³. Contours $n_e(r, \xi, z_i)$ were generated at 12 pump propagation distances z_i ($1 < i < 12$), which encompassed various stages of bubble evolution. COMSOL solved Maxwell's equations for a 400nm probe pulse propagating obliquely through the plasma object and extracted the phase change $\Delta\phi_{pr}(\rho, \tau)$ induced on its electric field. Here, ρ denotes distance perpendicular to the propagation axis, and τ is time behind the leading edge of the probe pulse. Figure 4-2 (a) shows two of the 12 wake structures: $i = 1$, immediately after the pump entered the plasma and formed a sinusoidal wake (Figure 4-2 (a1)), and $i = 6$, after the pump has propagated half way through the plasma, self-focused, self-steepened, and formed a bubble (Figure 4-2 (a2)). Figure 4-2 (b) shows corresponding sections of the phase

streak: a shallow, smooth profile from averaging peaks and valleys of the sinusoidal wake (Figure 4-2 (b1)), and a deeper, more structured profile after the bubble forms (Figure 4-2 (b2)). The contrast between these two sections of the phase streak enables us to identify the onset of bubble formation. Figure 4-2 (c), a lineout of $\Delta\phi(\xi)$ along ξ , further illustrates the dramatic change in phase that accompanies bubble formation.

4.3. PROTOTYPE FREQUENCY-DOMAIN STREAK CAMERA

Zhengyan Li [163] has some preliminary results of the proof of concept experiment where the focal spots of the 800 nm pump and 400 nm probe pulses overlap inside a fused silica crystal at collinear degree (0 °) and noncollinear degree (14 °) shown at Figure 4-3. In Figure 4-3 (a) pump pulse is ~ 30 fs in duration and the peak intensity is ~ 10^{11} W/cm². Figure 4-3 (a) shows the reconstructed temporal phase jump caused by the n₂I effect in the collinear configuration. The longer duration of the phase jump is due to the slippage between the pump pulse and probe pulse. Figure 4-3 (b) shows a phase streak in the noncollinear configuration. The angle of the phase streak confirms the theoretical prediction. With minor adjustments, the same setup can be utilized in plasma measurement.

4.4. SIMULATIONS OF MULTI-FRAME “MOVIE” RECONSTRUCTION

The FDSC by itself integrates phase along ξ . Thus, the bubble structure at each z_i remains unknown. To overcome this drawback, we propose frequency domain tomography (FDT). In computer-aided tomography (CAT) [162] projections of a stationary 3-D object are recorded on 2-D image surfaces at multiple viewing angles. From those data, cross-sectional images of the 3-D object in various planes are then

reconstructed using filtered back projection algorithms developed in the 1970s. We can achieve an analogous goal — reconstruction of cross-sectional images of a moving, evolving plasma object at various locations z_i — by employing FDSC at multiple viewing angles.

FDT and CAT differ in that the former records accumulated phases of a moving object, the latter of a stationary object. To connect FDT and CAT, consider a reference line ξ_{\perp} perpendicular to ξ in the plane of Fig. 4-1 (b) that remains stationary in the reference frame of the probe. A bubble of radius r_b crosses this line in time $\tau_{\text{transit}} = r_b/c\sin(\alpha/2)$. For example, the bubble in our simulation ($r_b = 20 \mu\text{m}$) crosses it in $\tau_{\text{transit}} = 94 \text{ fs}$ for $\alpha = 90^\circ$. Since the bubble's total propagation time across a 1 mm gas jet is 3.3 ps, it is reasonable to assume that its structure remains quasi-static during τ_{transit} . With this mild assumption, the accumulated phase profile $\Delta\phi(\xi_{\perp})$ along the reference line ξ_{\perp} is identical to the phase profile that would be accumulated by the same probe propagating across an identical *stationary* bubble at angle $\pi/2 - \alpha/2$ with respect to its front-back axis. The existence of this equivalent problem establishes the connection between FDT and CAT, and enables the use of reconstruction techniques already developed for CAT scans with little alteration.

To complete the space-time reconstruction of the bubble, additional reference lines parallel to ξ_{\perp} were constructed along the phase streak at spacings $\geq \tau_{\text{transit}}$. Phase profiles along these lines represent 1-D projections of quasi-static bubble structure at different stages of evolution. We then acquire an equivalent family of phase profiles from streaks recorded at different intersection angles α and apply the clinical CAT algorithm. Figure 4-4 shows a simulated tomographic reconstruction of the bubble of

Figure 4-2 at z_0 (Figure 4-4 (a)) using different numbers of probe pulses in the same plane. Three probe beams are enough to detect the head and tail of the plasma bubble, where n_e is high (Figure 4-4 (b)). With ~ 10 probe beams the whole bubble shape is discernible (Figure 4-4 (c)), and sharpens with additional probes (Figure 4-4 (d)). Similar reconstructions are obtained for other z_i . Strung together, they form a movie. Oblique angle probes provide the only way to image wakes inside of preformed plasma channels, since probe pulses do not propagate freely along the channel axis.

4.5. DESIGN OF FREQUENCY-DOMAIN STREAK CAMERA FOR THE TEXAS PETAWATT LASER-PLASMA ACCELERATION EXPERIMENT

The ongoing Texas Petawatt laser electron acceleration experiment [164] promised to generate multi-GeV electron beams. To visualize the plasma structure, one must use a non-collinear setup because of the difficulty of separating the probe pulse from the transmitted petawatt beam after the interaction region. The result from the non-collinear probe probably yields more insights into the acceleration process than a collinear probe, because oscillations of the bubble's length are essential to triggering self-injection of electrons at the low plasma density ($n_e \sim 10^{17} \text{ cm}^{-3}$) being used in this experiment [23]. The theory of electron trapping by evolving bubble structures [23] can also be tested here. Fig. 4.5 shows the target region setup of the petawatt experiment. First small chamber in the left is used to combine the probe pulse pair with the pump pulse. The chamber in the middle is the target chamber, where the pump pulse focuses in the gas cell. Probe pulse pair is separated with pump pulse here and sent into a spectrometer. Low energy electrons ($< \sim 300 \text{ MeV}$) are measured in this chamber with a $\sim 1 \text{ T}$ magnet and a Lanex screen. In the final chamber, a 0.1 mm Al film blocks the pump pulse. Optical transmission radiation (OTR) is also measured from this Al film.

A calorimeter at the end of the chamber measures the energy of the electrons generated within the range of 1-10 GeV.

The probe beam pair is taken from the leakage of the petawatt beam (1.06 μ m, 167 fs, 186 J) [165] before it is fully amplified. The probe beam is then compressed with a miniature copy of the main compressor. After that, the beam is converted to 532 nm by a KDP crystal. The beam is then sent through a \sim 8cm long gas cell at \sim 4 $^\circ$ with respect to the main beam and collected by a spectrometer. The angle cannot be too large; if it is, the probe pulse will not cover the entire acceleration length. It cannot be too small either, or the mirror that collects the probe beam will be damaged by the transmitted pump pulse. These trade-offs are illustrated in Fig 4-6. The collecting imaging optics needs to be close enough to obtain a \sim 10 μ m resolution. Here, an F#10 lens is used. Additional probe beams are also implemented to measure gas density and Thomson scattering.

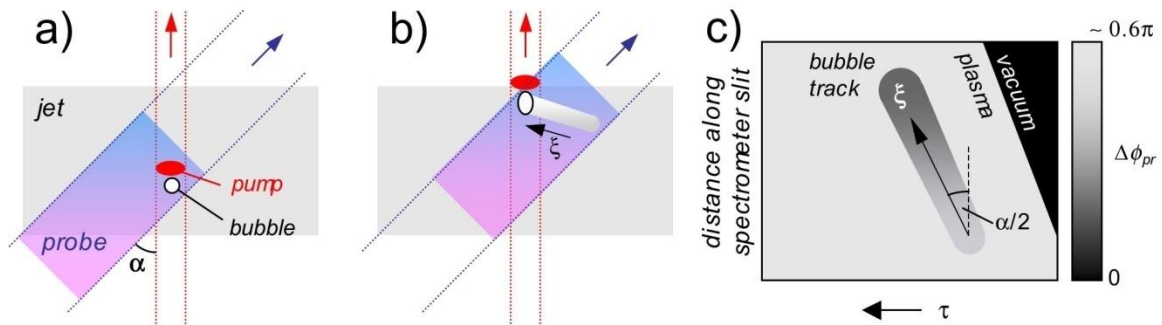


Figure 4-1. Schematic of noncollinear FDH for characterizing longitudinal evolution of a luminal velocity plasma bubble. (a) Pump (red), trailing bubble (white), and chirped probe overlapping at angle α in gas jet; (b) Same at a later time, showing how the evolving bubble sweeps out a streak (gray) tilted at angle $\alpha/2$ from the leading edge of the probe; (c) Schematic reconstructed probe phase shift $\Delta\phi_{pr}(\rho, \tau)$, where ρ denotes the distance perpendicular to the propagation axis, and τ is the time behind the leading edge of probe.

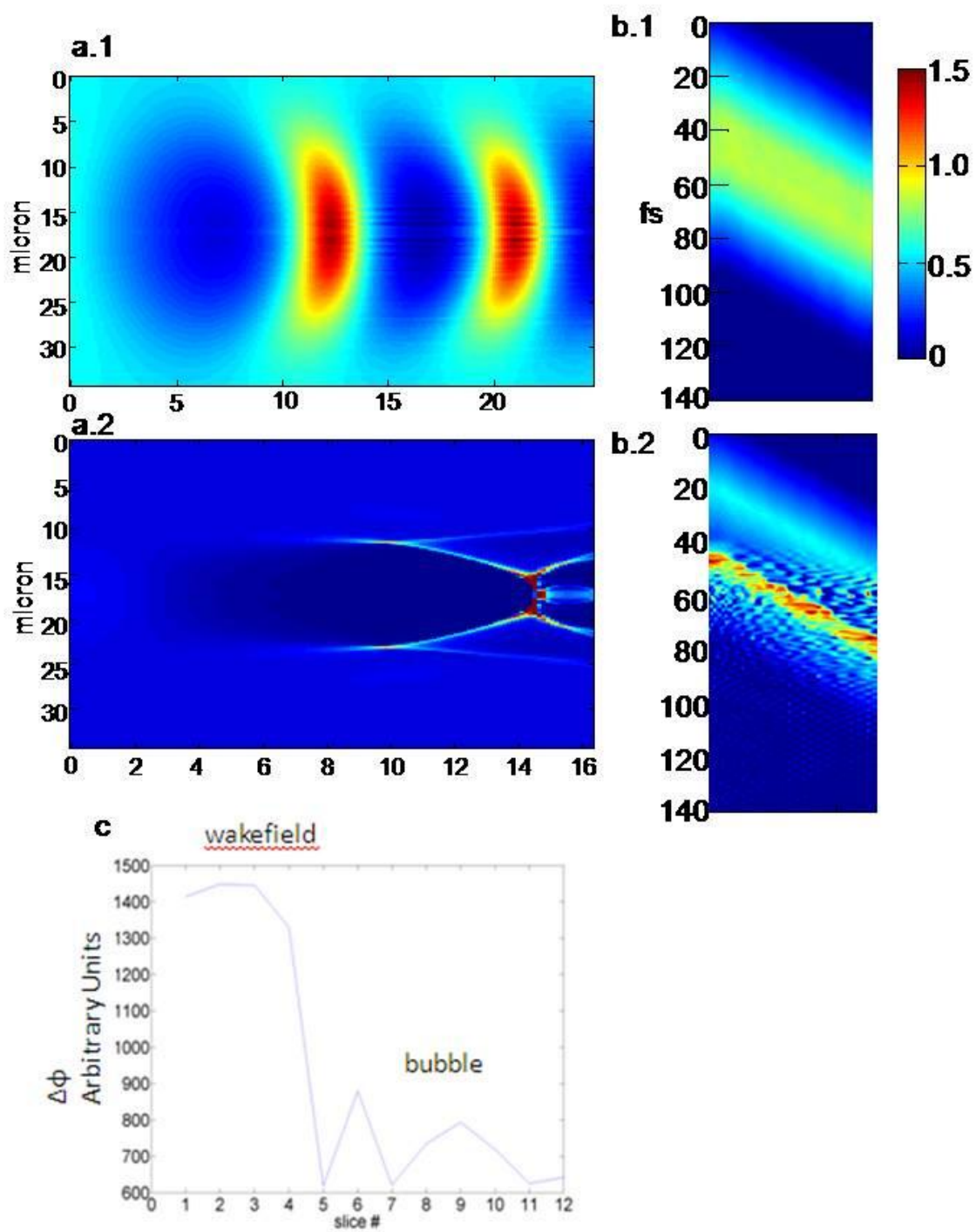


Figure 4-2 Simulation of the frequency domain streak camera. (a) Wake profiles $n_e(r, \zeta, z_i)$ at two pump propagation distances, z_1 and z_6 , into the plasma, simulated by the PIC code WAKE: (a1) Sinusoidal wake at z_1 , immediately after the pump enters the plasma; (a2) Fully formed bubble at z_6 , half way through plasma. (b) Corresponding “frames” of phase streak imposed by structures $n_e(r, \zeta, z_{1,2})$ on a probe pulse after propagating through them at right angles to the pump. These frames show a clear contrast between the wakefield and bubble stages. (c) A lineout of phase change $\Delta\phi_{pr}(\xi)$ imposed on the probe along the axis ξ of the phase streak, garnered from 12 consecutive frames corresponding to pump propagation distances z_1 thru z_{12} . A large change in $\Delta\phi_{pr}(\xi)$ at frame 5 identifies the point of bubble formation.

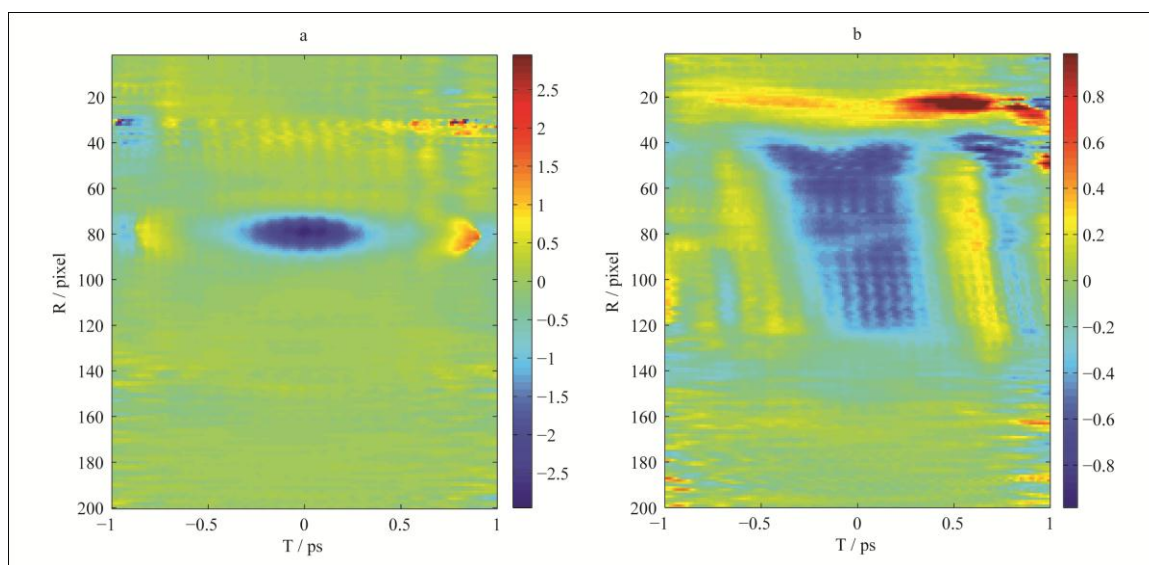


Figure 4-3 Experimental results [163] showing formation of a phase bullet due to the n_2I effect when pump and probe pulses go through 3mm fused silica crystal collinearly (a), and the phase streak when the pulses cross each other noncollinearly at 14° (b). Courtesy of Zhengyan Li .

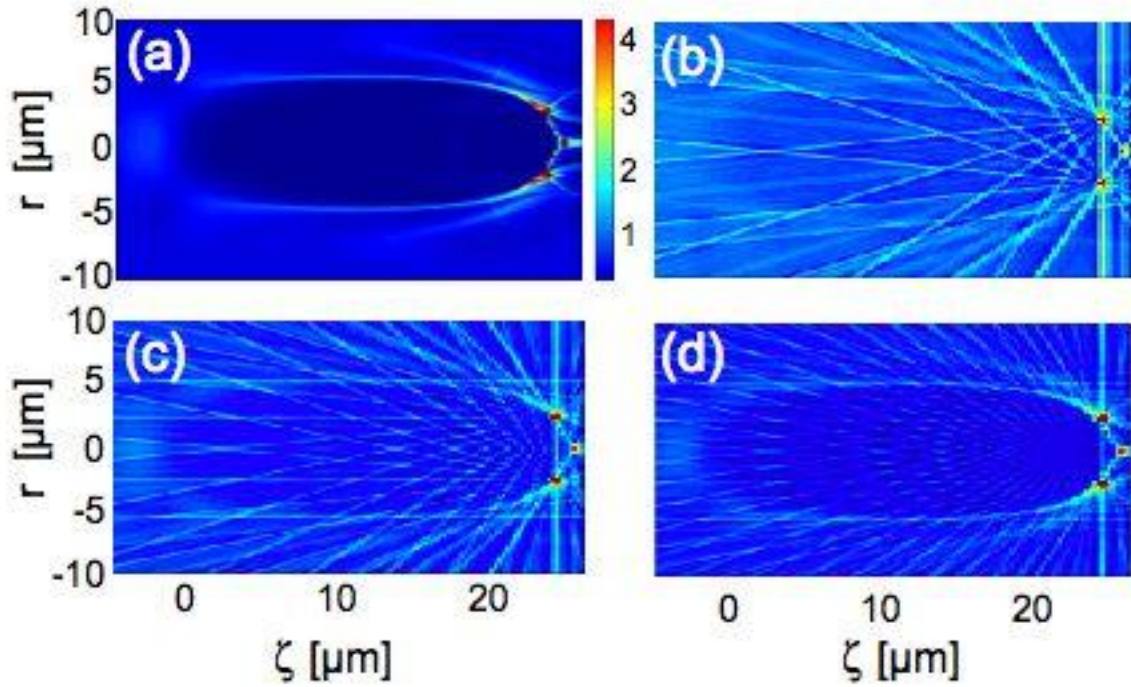


Figure 4-4 Simulation of frequency-domain tomography. (a) Bubble profile $n_e(r, \zeta, z_9)$ in frame z_9 of simulation in Fig. 4-2. Color scale is labeled in units of 10^{19} cm^{-3} . Remaining frames show reconstructions of this profile using probes at multiple angles α and filtered back projection algorithm: (b) 5 probes ($0^\circ \leq \alpha \leq 80^\circ$, 20° increments); (c) 10 probes ($0^\circ \leq \alpha \leq 90^\circ$, 10° increments); (d) 20 probes ($0^\circ \leq \alpha \leq 90^\circ$, 5° increments).

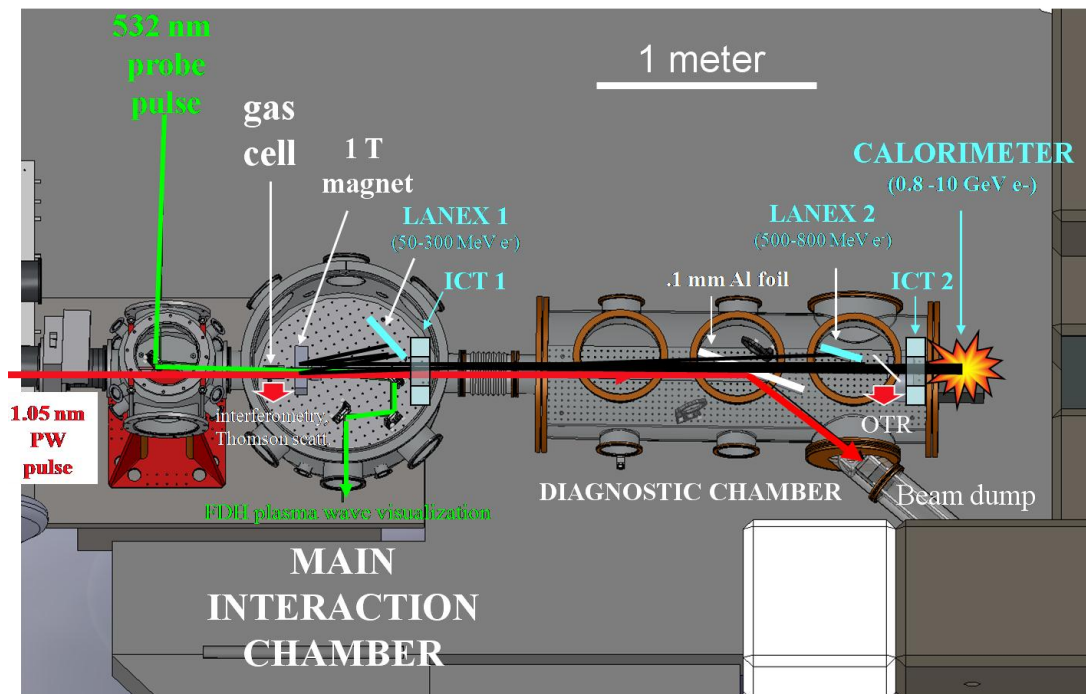


Figure 4-5 Preliminary experimental setup of Texas Petawatt LWFA experiment.

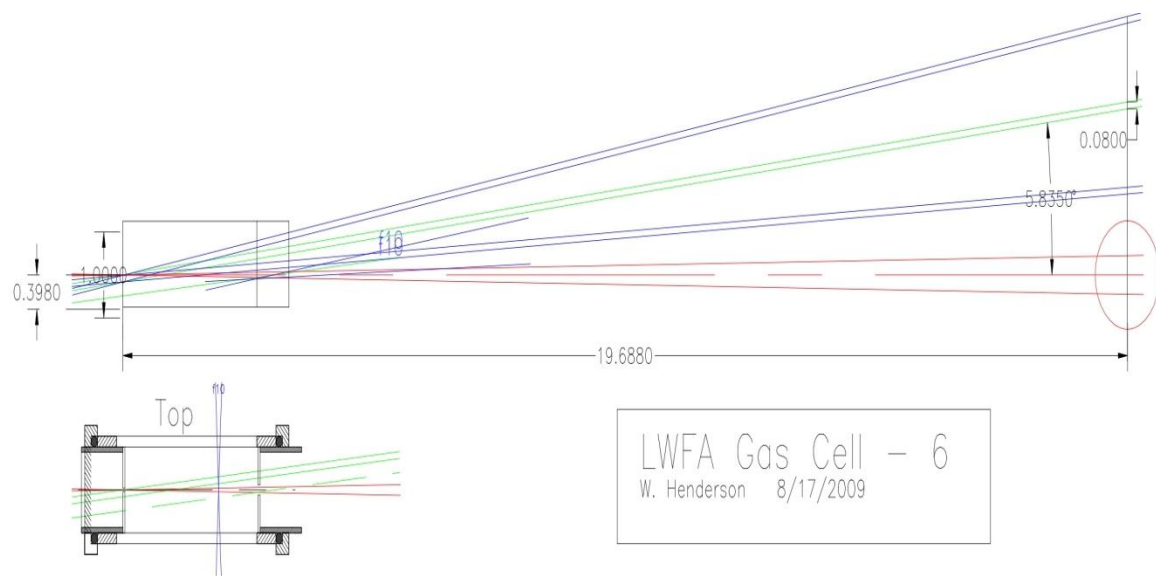


Figure 4-6 A design setup of the probe pulse intersecting the gas cell (courtesy of W. Henderson). Red lines represent the pump beam. Green lines represent the FDH probe beam. Blue lines represent the probe beam for Michelson interferometer.

Chapter 5. Future directions

This chapter discussed the prospect of using FDH technique to visualize beam-driven PWFAs and channeled LWFAs

5.1. VISUALIZATION OF BEAM-DRIVEN PWFAS

A recent electron plasma accelerator experiment at SLAC [166] demonstrated the doubling of the energy of the 42 GeV electron beam at SLAC over a distance of ~ 1 m. In their one electron beam setup, however, the electron spectrum was wide spread, because the earlier part of the electron beam when driving the wakefield, transferred energy to the later part of the electron beam. Lee et al [167] proposed the idea of doubling both the electron and positron beam energy from the SLAC over a few meters of plasma afterburner. They suggested splitting the current 42 GeV electron or positron beam into two bunches. The first sets up the wakefield, and the trailing bunch surfs on it. In this way, the electron beams are mono-energetic. The positron-excited wakefields are normally smaller than electron wakes because of the analogous “suck-in” behavior [168]. To achieve the same amplitude, a hollow channel must be used. To understand the differences between electron and positron driven wakes and fully implement the afterburner idea, one needs observational tools for the beam-driven wakefield. The frequency domain technique should accomplish much in this field due to the similarity between the beam driven and laser-driven wakefield.

Our group member, Dr. Rafal Zgadzaj is performing a project at Brookhaven National Laboratory’s Accelerator Test Facility (BNL-ATF) to measure the wakefield amplitude change when it is resonantly excited by a train of electron microbunches [169]. Fig. 5-1 shows the schematic setup of the experiment. Chirped optical probe and

reference pulses will co-propagate with ATF's 70 MeV, 100 pC e-drive-bunch train and its plasma wake. Compared to previous visualization of LPAs, this experiment faces two primary technical challenges: 1) timing jitter. The timing jitter between the electron bunch and probe laser pulse is at sub-picoseconds levels. The plasma wakefield wavelength is at ~ 200 fs. Clearly the timing jitter will prevent any meaningful measurement. This jitter is managed by implementing the electro-optic (e-o) detection scheme as shown in Fig. 5-1. The 70 MeV drive bunches pass near a ZnTe crystal, and their electric fields electro-optically induces a transient refractive index change that is sensed by a split-off portion of the probe pulse. The timing of the e-o change within the probe pulse is then measured with ~ 50 fs accuracy by an FD interferometry (FDI) system using the same spectrometer. By repeating this e-o measurement on each shot, relative timing of e-bunches driving the plasma and probe pulses probing the plasma will be known with the enough accuracy, enabling accurate interpretation of data and multi-shot averaging to improve sensitivity. A similar jitter correction technique was developed by Cavalieri et al. [170], for optical pump/x-ray probe experiments at the Sub-Picosecond Pulse Source at the Stanford Linear Accelerator. 2) Low plasma density. The plasma density in this experiment is at $10^{16} - 10^{17} \text{ cm}^{-3}$ range. With plasma density perturbation in the range of 1% and 10%, the anticipated probe phase shift is at $0.5 \times 10^{-2} < \Delta\phi < 0.5 \times 10^{-1}$ radians, ~ 5 to $\sim 50\times$ smaller than $\Delta\phi$ measured typically in our previous single-shot experiments, but comparable to $\Delta\phi$ measured in multi-shot-averaged FDI experiments [79]. On the other hand, background noise level is much lower because of the complete absence of scattered, frequency-shifted pump light, the major noise source in previous single-shot experiments. The BNL-ATF experiments will provide the first direct visualization of plasma wakes driven by charged particle bunches.

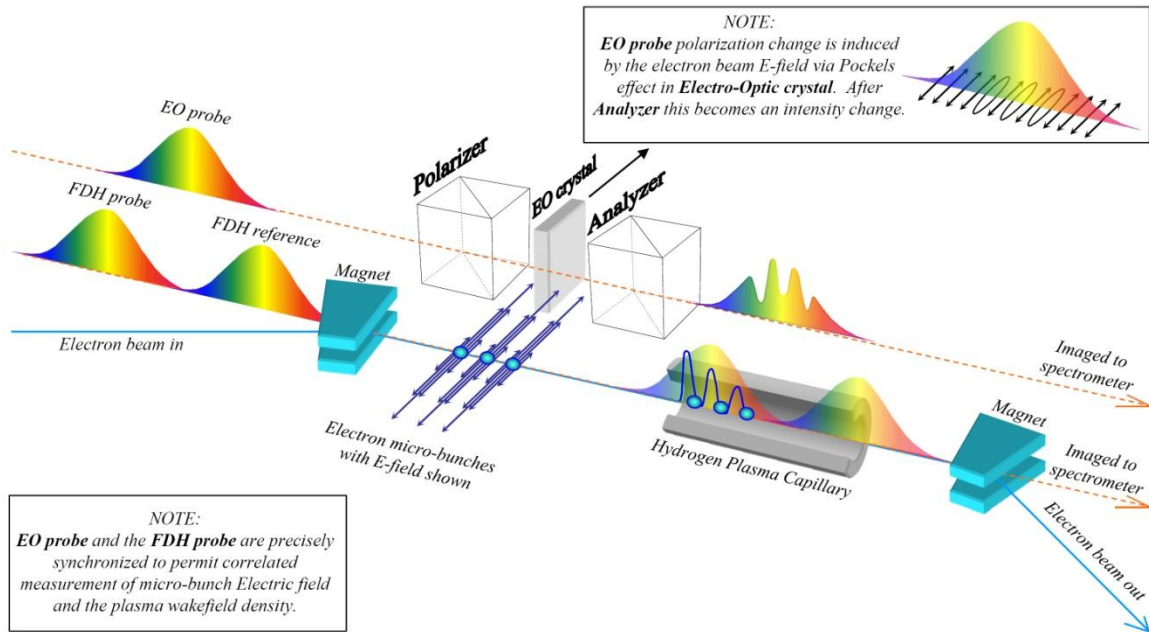


Figure 5.1 Schematic layout of BNL-ATF experiment. The electron beam is combined with the chirped, temporally stretched, FDH probe/reference pulses beam at a turning magnet. The probe pulse overlaps the electron bunch train in time; the reference pulse precedes it. After the interaction in the discharge capillary, the laser pulses are again separated at a turning magnet. The laser mode exiting the capillary is finally imaged onto a spectrometer slit, and the plasma wave longitudinal and radial structure is recovered by conventional FDH methods. In parallel a nondestructive e-o measurement of relative delay of the two beams, and of the duration and format of the e-beam bunch train, will be made on every shot. Courtesy of Rafal Zgadzaj.

5.2. VISUALIZATION OF CHANNELED LWFAS

The role of plasma channel guiding in future laser plasma accelerators is still under debate. Most recent demonstrations of quasi-monoenergetic LWFA have used no

external guide (relying on self-guiding of the driving pulse). On the other hand, the most energetic quasi-monoenergetic electrons (up to 1 GeV) have been achieved with capillary guiding [15]. Looking to the future, the simulations [95] of based on the 3D PIC code OSIRIS envision several possible roadmaps for future laser-plasma accelerators that produce electron bunches ranging from 1 GeV to 1 TeV in energy. These include viable designs using both channel and self-guiding. Thus it appears that researchers will continue to pursue both approaches to LWFA for the foreseeable future.

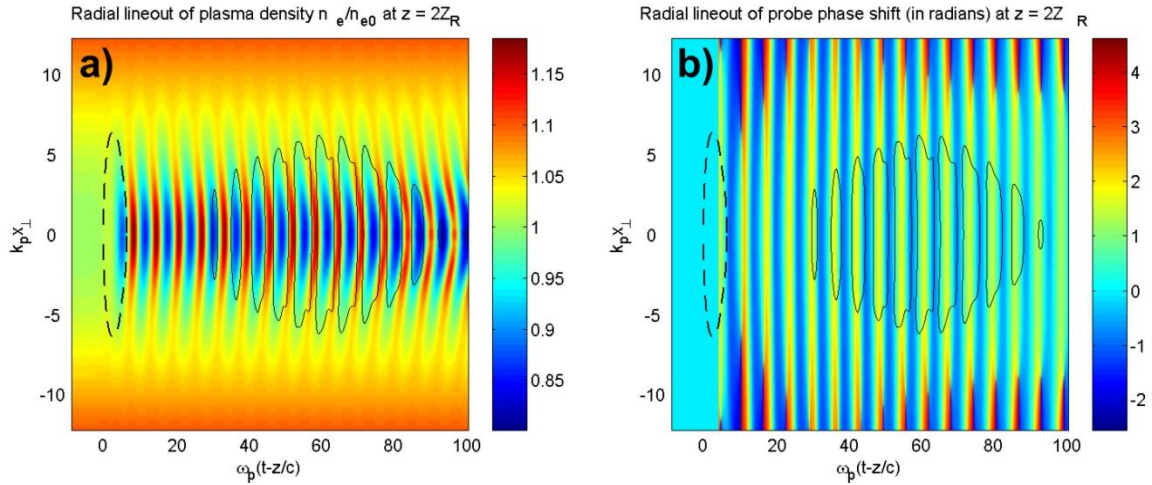


Fig. 5.2. WAKE simulations (done by Serguei Kalmykov) showing plasma wake generated in a preformed plasma channel with parabolic radial density profile, axial density $n_e(r=0) = 3 \times 10^{18} \text{ cm}^{-3}$ by a mildly relativistic drive pulse (40 fs, 800 nm, 5 TW, 0.6 Pcr) propagating to left (dashed contour shows e^{-2} intensity), focused to a perfectly matched channel eigenmode with $a_0 = 0.48$, Gaussian waist $w_0 = 25 \text{ }\mu\text{m}$. a) electron density profile $n_e(r, \zeta, z = 2z_R)$ after propagating 2 Rayleigh lengths, showing curved wavefronts. b) phase shift $\phi_{pr}(r, \zeta)$ imposed on co-propagating 800 nm probe (solid contour) after 2 Rayleigh lengths, showing apparent flattening of wave fronts.

Conventional collinear FDH suffers from two major problems in probing wakefields propagating in plasma channels: (1) Group-velocity walk-off for 400 nm probe/800 nm pump combination will be unacceptably high. The minimum axial density achievable in laser-generated channels is $n_e \sim 5 \times 10^{18} \text{ cm}^{-3}$, causing 800/400nm pulses to walk off by $\lambda_p/4$ in < 2 mm. This can be alleviated by using probe pulses closer in wavelength to the pump pulse. For example, in my early work as a graduate student, I helped develop a Chirped Pulse Raman Amplifier, still operational in our laboratory, that produces 870 nm pulses that are temporally synchronized with the main 800 nm pulses of our laser system [142]. 870 nm probe/reference pulses would extend the $\lambda_p/4$ walk-off distance to > 1 cm. On the other hand, the problem of interference from pump-generated white light (see Sec. 3.1) could become even more severe than for 400 nm probe pulses.

(ii) Information about radial structure of a channeled wake becomes scrambled, because radial components of the k-vector of the guided probe pulse interchange during propagation over more than a Rayleigh length z_R . In a ray optics picture, radial scrambling results from internal reflections of the probe from interior waveguide walls. To illustrate this, Fig. 5.2 shows WAKE simulations by S. Kalmykov of **a)** electron density $n_e(r, \zeta, z = 2z_R)$ behind a drive pulse after guiding over $2z_R$ through a preformed channel, and **b)** the corresponding phase shift $\phi_{pr}(r, \zeta)$ imparted to a co-propagating probe. For simplicity, pump and probe were mode-matched perfectly to the channel (to avoid beam radius oscillations) and identical in wavelength (to avoid group velocity walk-off), and the drive pulse was only mildly relativistic ($a_0 = 0.48$) to avoid strong self-

focusing. Fig. 5.2a shows curved plasma wave front developing behind the pump, similar to those observed by collinear FDH in [80]. However, Fig. 5.2b shows that these wavefronts, though visible in the longitudinal direction, appear radially flattened in the corresponding probe phase shift plot after guided propagation of $2z_R$. In fact, the radial scrambling of phase information by the guiding action of the channel is exactly analogous to phase scrambling by refraction in propagating bubbles, as described in Chapter 3. When it occurs over long path lengths, it prevents image reconstruction. Additional information loss can be expected when pump and probe differ in group velocity, are mode-matched imperfectly to the channel, or experience strong relativistic self-focusing.

To avoid this loss of information, I anticipate it will be necessary to use the non-collinear FDSC and FDT techniques described in Chapter 4 to visualize wakefields propagating in plasma channels. Oblique-incidence probes avoid the strong refraction that 0° probe/ref pulses experience when interacting with plasma channels because a given point of the oblique probe pulse profile interacts with the channel only during its transit across the structure, which is much shorter than the length of the channel. Thus the proposed FDT system will open channeled LWFAs to direct laboratory visualization for the first time. Of course the non-collinear probe will also provide temporal evolution information as discussed in Chapter 4. Our group has recently initiated a collaboration with the L'Oasis group at Lawrence Berkeley National Laboratory (LBNL) to develop wake visualization tools for the Berkeley Electron Laser Accelerator (BELLA)

experiment at LBNL. At BELLA, 40 J, 30 fs laser pulses will drive evolving plasma waves quasi-linearly inside plasma waveguides [109] of tapered $\bar{n}_e(z)$ formed by electrical discharge inside transparent sapphire structures. The channel is optically accessible from the side to FDSC/FDT probes along most of its length. To help us develop and refine an FDSC/FDT system, the BELLA team will provide us with test sapphire channel structures with rectangular bores through which we will propagate 1 J, 30 fs pulses from our UT system to create test plasma structures (*e.g.* ionization fronts, linear wakes) that we will probe transversely via FDSC/FDT. Test results will be used to plan implementation of FDSC/FDT at BELLA.

Through these collaborations with BNL-ATF, FACET and BELLA, the combined work of this thesis and of my predecessor N. Matlis will begin to impact the highest profile plasma accelerator experiments in the world. FDH, FDS, FDSC and FDT will “remove the blindfolds” from plasma-based accelerator science, and contribute in a fundamental way to the development and maintenance of the next generation’s accelerators.

Appendix: Publications by the Author

F. B. Grigsby, **P. Dong**, and M. C. Downer, “*Chirped-pulse Raman amplification for two-color, high-intensity laser experiments*”, JOSA B **25**, Issue 3, 346-350 (2008)

P. Dong, S. Reed, S. Kalmykova, G. Shvets, M. C. Downer et al., “*Electron beam generation in blowout regime and imaging of plasma bubble in laser wakefield accelerators using Frequency Domain Holography*”, High Energy Density Physics **6**, 153–156 (2010)

P. Dong, S. Reed, S. Kalmykova, G. Shvets, M. C. Downer et al., “*Holographic Visualization of Laser Wakefields*”, New Journal of Physics **12**, 045016 (2010)

P. Dong, S. Reed, S. Kalmykova, G. Shvets, M. C. Downer et al., “*Formation of optical bullets in laser-driven plasma bubble accelerators*”, Physical Review letters **104**, 134801 (2010)

Bibliography

1. Fernow, R.C. *Introduction to Experimental Particle Physics*. (Cambridge University Press: 1989).
2. Karzmark, C.J., Nunan, C.S. & Tanabe, E. *Medical Electron Accelerators*. (McGraw-Hill Companies Health Professions Divi: 1992).
3. Neutze, R., Wouts, R., van der Spoel, D., Weckert, E. & Hajdu, J. Potential for biomolecular imaging with femtosecond X-ray pulses. *Nature* **406**, 752-757 (2000).
4. Brumfiel, G. Physicists pitch biggest accelerator. *Nature* **445**, 694 (2007).
5. Tajima, T. & Dawson, J.M. Laser Electron Accelerator. *Phys. Rev. Lett.* **43**, 267–270 (1979).
6. Nakajima, K. et al. Observation of Ultrahigh Gradient Electron Acceleration by a Self-Modulated Intense Short Laser Pulse. *Phys. Rev. Lett.* **74**, 4428 (1995).
7. Coverdale, C.A. et al. Propagation of Intense Subpicosecond Laser Pulses through Underdense Plasmas. *Phys. Rev. Lett.* **74**, 4659 (1995).
8. Modena, A. et al. Electron acceleration from the breaking of relativistic plasma waves. *Nature* **377**, 606-608 (1995).
9. Umstadter, D., Chen, S., Maksimchuk, A., Mourou, G. & Wagner, R. Nonlinear Optics in Relativistic Plasmas and Laser Wake Field Acceleration of Electrons. *Science* **273**, 472-475 (1996).
10. Clayton, C.E. et al. Plasma Wave Generation in a Self-Focused Channel of a Relativistically Intense Laser Pulse. *Phys. Rev. Lett.* **81**, 100 (1998).
11. Dewa, H. et al. Experiments of high energy gain laser wakefield acceleration. *Nuclear Instruments and Methods in Physics Research Section A: Accelerators, Spectrometers, Detectors and Associated Equipment* **410**, 357 - 363 (1998).
12. Mangles, S.P.D. et al. Monoenergetic beams of relativistic electrons from intense laser-plasma interactions. *Nature* **431**, 535-538 (2004).
13. Geddes, C.G.R. et al. High-quality electron beams from a laser wakefield accelerator using plasma-channel guiding. *Nature* **431**, 538-541 (2004).
14. Faure, J. et al. A laser-plasma accelerator producing monoenergetic electron beams. *Nature* **431**, 541-544 (2004).
15. Leemans, W.P. et al. GeV electron beams from a centimetre-scale accelerator. *Nature Physics* **2**, 696-699 (2006).
16. Mangles, S.P.D. et al. Laser-Wakefield Acceleration of Monoenergetic Electron Beams in the First Plasma-Wave Period. *Phys. Rev. Lett.* **96**, 215001 (2006).
17. Karsch, S. et al. GeV-scale electron acceleration in a gas-filled capillary discharge waveguide. *New J. Phys.* **9**, 415-415 (2007).
18. Osterhoff, J. et al. Generation of Stable, Low-Divergence Electron Beams by Laser-Wakefield Acceleration in a Steady-State-Flow Gas Cell. *Phys. Rev. Lett.* **101**, 085002 (2008).
19. Hafz, N.A.M. et al. Stable generation of GeV-class electron beams from self-guided

- laser-plasma channels. *Nauret Photon* **2**, 571-577 (2008).
20. Kneip, S. et al. Near-GeV Acceleration of Electrons by a Nonlinear Plasma Wave Driven by a Self-Guided Laser Pulse. *Phys. Rev. Lett.* **103**, 035002 (2009).
 21. Froula, D.H. et al. Measurements of the Critical Power for Self-Injection of Electrons in a Laser Wakefield Accelerator. *Phys. Rev. Lett.* **103**, 215006 (2009).
 22. Pukhov, A. & Meyer-ter-Vehn, J. Laser wake field acceleration: the highly non-linear broken-wave regime. *Applied Physics B-Lasers And Optics* **74**, 355-361 (2002).
 23. Kalmykov, S., Yi, S.A., Khudik, V. & Shvets, G. Electron Self-Injection and Trapping into an Evolving Plasma Bubble. *Phys. Rev. Lett.* **103**, 135004 (2009).
 24. Hegelich, B.M. et al. Laser acceleration of quasi-monoenergetic MeV ion beams. *Nature* **439**, 441-444 (2006).
 25. Hatchett, S.P. et al. Electron, photon, and ion beams from the relativistic interaction of Petawatt laser pulses with solid targets. *Phys. Plasmas* **7**, 2076 (2000).
 26. Snavelly, R.A. et al. Intense High-Energy Proton Beams from Petawatt-Laser Irradiation of Solids. *Phys. Rev. Lett.* **85**, 2945 (2000).
 27. Chen, H. et al. Relativistic Positron Creation Using Ultraintense Short Pulse Lasers. *Phys. Rev. Lett.* **102**, 105001 (2009).
 28. Robinson, A.P.L., Zepf, M., Kar, S., Evans, R.G. & Bellei, C. Radiation pressure acceleration of thin foils with circularly polarized laser pulses. *New J. Phys.* **10**, 013021 (2008).
 29. Thaddeus Trenn J. The Self-Splitting Atom: The History of the Rutherford-Soddy Collaboration. 58-60, 111-117 (1977).
 30. Aleklett, K., Morrissey, D.J., Loveland, W., McGaughey, P.L. & Seaborg, G.T. Energy dependence of ²⁰⁹Bi fragmentation in relativistic nuclear collisions. *Phys. Rev. C* **23**, 1044 (1981).
 31. Adamenko, S.V., Selleri, F. & Merwe, A.V.D. *Controlled Nucleosynthesis: Breakthroughs in Experiment and Theory*. (Springer Netherlands: 2009).
 32. Bloom, E.D. et al. High-Energy Inelastic e-p Scattering at 6° and 10°. *Phys. Rev. Lett.* **23**, 930 (1969).
 33. Perl, M.L. et al. Evidence for Anomalous Lepton Production in e⁺-e⁻ Annihilation. *Phys. Rev. Lett.* **35**, 1489 (1975).
 34. Bergmann, H. *Radioactive Isotopes in Clinical Medicine and Research*. (Birkhauser: 1995).
 35. Giannuzzi, L.A. & University, N.C.S. *Introduction to Focused Ion Beams: Instrumentation, Theory, Techniques and Practice*. (Springer: 2004).
 36. History of Synchrotron Radiation Sources. at <http://xdb.lbl.gov/Section2/Sec_2-2.html>
 37. Wiedemann, H. *Synchrotron Radiation*. (Springer Berlin Heidelberg: 2010).
 38. McNeil, B. Free electron lasers: First light from hard X-ray laser. *Nature Photon* **3**, 375-377 (2009).
 39. Jackson, J.D. *Classical Electrodynamics Third Edition*. (Wiley: 1998).
 40. Braun, H.H., D'bert, S., Wilson, I. & Wuensch, W. Frequency and Temperature

- Dependence of Electrical Breakdown at 21, 30, and 39 GHz. *Phys. Rev. Lett.* **90**, 224801 (2003).
41. <<http://www-rcf.usc.edu/~muggli/accelerators.html#>>
 42. Strickland, D. Compression of amplified chirped optical pulses. *Optics Communications* **55**, 447-449 (1985).
 43. Ta Phuoc, K. et al. X-Ray Radiation from Nonlinear Thomson Scattering of an Intense Femtosecond Laser on Relativistic Electrons in a Helium Plasma. *Phys. Rev. Lett.* **91**, 195001 (2003).
 44. Bahk, S.W. et al. Generation and characterization of the highest laser intensities (10(22) W/cm(2)). *OPTICS LETTERS* **29**, 2837-2839 (2004).
 45. Kruer, W. *The Physics of Laser Plasma Interactions*. (Westview Press: 2001).
 46. Landau, L.D. & Lifshitz, E. *The Classical Theory of Fields, Fourth Edition: Volume 2*. (Butterworth-Heinemann: 1980).
 47. Troha, A.L. & Hartemann, F.V. Reply to "Comment On 'Vacuum electron acceleration by coherent dipole radiation' ". *Phys. Rev. E* **65**, 028502 (2002).
 48. Plettner, T., Byer, R.L. & Smith, T.I. First Observation Of Laser-Driven Acceleration Of Relativistic Electrons In A Semi-Infinite Vacuum Space. (2005).
 49. Kimura, W.D. et al. Laser Acceleration of Relativistic Electrons Using the Inverse Cherenkov Effect. *Phys. Rev. Lett.* **74**, 546 (1995).
 50. York, A.G., Milchberg, H.M., Palastro, J.P. & Antonsen, T.M. Direct Acceleration of Electrons in a Corrugated Plasma Waveguide. *Phys. Rev. Lett.* **100**, 195001 (2008).
 51. Kimura, W.D. et al. Demonstration of High-Trapping Efficiency and Narrow Energy Spread in a Laser-Driven Accelerator. *Phys. Rev. Lett.* **92**, 054801 (2004).
 52. Gahn, C. et al. Multi-MeV Electron Beam Generation by Direct Laser Acceleration in High-Density Plasma Channels. *Phys. Rev. Lett.* **83**, 4772 (1999).
 53. Lawson, J.D. Lasers and Accelerators. *Nuclear Science, IEEE Transactions on* **26**, 4217-4219 (1979).
 54. Mori, W., Joshi, C., Dawson, J., Forslund, D. & Kindel, J. Evolution of self-focusing of intense electromagnetic waves in plasma. *Phys. Rev. Lett.* **60**, 1298-1301 (1988).
 55. Gaul, E.W. et al. Production and characterization of a fully ionized He plasma channel. *Appl. Phys. Lett.* **77**, 4112 (2000).
 56. Karsch, S. et al. GeV-scale electron acceleration in a gas-filled capillary discharge waveguide. *New J. Phys.* **9**, 415-415 (2007).
 57. Lu, W., Huang, C., Zhou, M., Mori, W.B. & Katsouleas, T. Nonlinear Theory for Relativistic Plasma Wakefields in the Blowout Regime. *Phys. Rev. Lett.* **96**, 165002-4 (2006).
 58. Ralph, J.E. et al. Self-Guiding of Ultrashort, Relativistically Intense Laser Pulses through Underdense Plasmas in the Blowout Regime. *Physical Review Letters* **102**, 175003 (2009).
 59. Perry, M.D. & Mourou, G. Terawatt to Petawatt Subpicosecond Lasers. *Science* **264**, 917-924 (1994).

60. Mourou, G. & Umstadter, D. Development and applications of compact high-intensity lasers. *Physics of Fluids B: Plasma Physics* **4**, 2315-2325 (1992).
61. Strickland, D. & Mourou, G. Compression of amplified chirped optical pulses. *Optics Communications* **56**, 219 - 221 (1985).
62. Malka, V. et al. Electron Acceleration by a Wake Field Forced by an Intense Ultrashort Laser Pulse. *Science* **298**, 1596-1600 (2002).
63. Leemans, W.P. et al. Electron-Yield Enhancement in a Laser-Wakefield Accelerator Driven by Asymmetric Laser Pulses. *Phys. Rev. Lett.* **89**, 174802 (2002).
64. Gahn, C. et al. Multi-MeV Electron Beam Generation by Direct Laser Acceleration in High-Density Plasma Channels. *Phys. Rev. Lett.* **83**, 4772-4775 (1999).
65. Ting, A. et al. Plasma wakefield generation and electron acceleration in a self-modulated laser wakefield accelerator experiment. *The 38th annual meeting of the Division of Plasma Physics (DPP) of the American Physical Society* **4**, 1889-1899 (1997).
66. Umstadter, D., Chen, S., Maksimchuk, A., Mourou, G. & Wagner, R. Nonlinear Optics in Relativistic Plasmas and Laser Wake Field Acceleration of Electrons. *Science* **273**, 472-475 (1996).
67. Nakajima, K. et al. Observation of Ultrahigh Gradient Electron Acceleration by a Self-Modulated Intense Short Laser Pulse. *Phys. Rev. Lett.* **74**, 4428-4431 (1995).
68. Modena, A. et al. Electron acceleration from the breaking of relativistic plasma waves. *Nature* **377**, 606-608 (1995).
69. Leemans, W.P. et al. GeV electron beams from a centimetre-scale accelerator. *Nat Phys* **2**, 696-699 (2006).
70. Faure, J. et al. Controlled injection and acceleration of electrons in plasma wakefields by colliding laser pulses. *Nature* **444**, 737-739 (2006).
71. Geddes, C.G.R. et al. Plasma-Density-Gradient Injection of Low Absolute-Momentum-Spread Electron Bunches. *Phys. Rev. Lett.* **100**, 215004 (2008).
72. Osterhoff, J. et al. Generation of Stable, Low-Divergence Electron Beams by Laser-Wakefield Acceleration in a Steady-State-Flow Gas Cell. *Phys. Rev. Lett.* **101**, 085002 (2008).
73. Hafz, N.A.M. et al. Stable generation of GeV-class electron beams from self-guided laser-plasma channels. *Nature Photon* **2**, 571-577 (2008).
74. Malka, V. et al. Principles and applications of compact laser-plasma accelerators. *Nature Physics* **4**, 447-453 (2008).
75. Mori, W.B., Joshi, C., Dawson, J.M., Forslund, D.W. & Kindel, J.M. Evolution of self-focusing of intense electromagnetic waves in plasma. *Phys. Rev. Lett.* **60**, 1298-1301 (1988).
76. Dawson, J.M. Particle simulation of plasmas. *Rev. Mod. Phys.* **55**, 403-447 (1983).
77. Mora, P. & Thomas M. Antonsen, J. Kinetic modeling of intense, short laser pulses propagating in tenuous plasmas. *Physics of Plasmas* **4**, 217-229 (1997).
78. Tsung, F.S. et al. Near-GeV-Energy Laser-Wakefield Acceleration of Self-Injected Electrons in a Centimeter-Scale Plasma Channel. *Phys. Rev. Lett.* **93**, 185002 (2004).

79. Siders, C.W. et al. Laser wakefield excitation and measurement by femtosecond longitudinal interferometry. *Phys. Rev. Lett.* **76**, 3570-3573 (1996).
80. Matlis, N.H. et al. Snapshots of laser wakefields. *Nature Physics* **2**, 749-753 (2006).
81. Matlis N. H. Frequency Domain Holography of laser wakefields. (2006).
82. Gibbon, P. *Short Pulse Laser Interactions with Matter: An Introduction*. (World Scientific Publishing Company: 2005).
83. Kruer, W. *The Physics of Laser Plasma Interactions*. (Westview Press: 2001).
84. Sprangle, P., Esarey, E., Ting, A. & Joyce, G. Laser wakefield acceleration and relativistic optical guiding. *Appl. Phys. Lett.* **53**, 2146-2148 (1988).
85. Sprangle, P., Esarey, E. & Ting, A. Nonlinear theory of intense laser-plasma interactions. *Phys. Rev. Lett.* **64**, 2011 (1990).
86. Sprangle, P., Esarey, E. & Ting, A. Nonlinear interaction of intense laser pulses in plasmas. *Phys. Rev. A* **41**, 4463 (1990).
87. Bulanov, S.V., Pegoraro, F., Pukhov, A.M. & Sakharov, A.S. Transverse-Wake Wave Breaking. *Phys. Rev. Lett.* **78**, 4205 (1997).
88. Bulanov, S.V., Pegoraro, F. & Pukhov, A.M. Two-Dimensional Regimes of Self-Focusing, Wake Field Generation, and Induced Focusing of a Short Intense Laser Pulse in an Underdense Plasma. *Phys. Rev. Lett.* **74**, 710 (1995).
89. Amiranoff, F. et al. Observation of Laser Wakefield Acceleration of Electrons. *Phys. Rev. Lett.* **81**, 995 (1998).
90. Clayton, C.E. et al. Ultrahigh-gradient acceleration of injected electrons by laser-excited relativistic electron plasma waves. *Phys. Rev. Lett.* **70**, 37 (1993).
91. Everett, M. et al. Trapped electron acceleration by a laser-driven relativistic plasma wave. *Nature* **368**, 527-529 (1994).
92. Le Blanc, S.P. et al. Temporal Characterization of a Self-Modulated Laser Wakefield. *Phys. Rev. Lett.* **77**, 5381 (1996).
93. Hora, H. Theory of relativistic self-focusing of laser radiation in plasmas. *J. Opt. Soc. Am.* **65**, 882-886 (1975).
94. Fomyts' kyi, M., Chiu, C., Downer, M. & Grigsby, F. Controlled plasma wave generation and particle acceleration through seeding of the forward Raman scattering instability. *Physics of Plasmas* **12**, 023103 (2005).
95. Lu, W. et al. Generating multi-GeV electron bunches using single stage laser wakefield acceleration in a 3D nonlinear regime. *Phys. Rev. ST Accel. Beams* **10**, 061301 (2007).
96. Siegman, A.E. *Lasers*. (University Science Books: 1986).
97. Sprangle, P. & Esarey, E. Interaction of ultrahigh laser fields with beams and plasmas. *Phys. Fluids B* **4**, 2241-2248 (1992).
98. Sprangle, P., Ting, A. & Tang, C.M. Analysis of radiation focusing and steering in the free-electron laser by use of a source-dependent expansion technique. *Phys. Rev. A* **36**, 2773 (1987).
99. Wagner, R., Chen, S., Maksimchuk, A. & Umstadter, D. Electron Acceleration by a Laser Wakefield in a Relativistically Self-Guided Channel. *Phys. Rev. Lett.* **78**, 3125 (1997).

100. Krushelnick, K. et al. Plasma Channel Formation and Guiding during High Intensity Short Pulse Laser Plasma Experiments. *Phys. Rev. Lett.* **78**, 4047 (1997).
101. Zgadzaj, R., Gaul, E.W., Matlis, N.H., Shvets, G. & Downer, M.C. Femtosecond pump-probe study of preformed plasma channels. *J. Opt. Soc. Am. B* **21**, 1559-1567 (2004).
102. Durfee III, C.G., Lynch, J. & Milchberg, H.M. Development of a plasma waveguide for high-intensity laser pulses. *Phys. Rev. E* **51**, 2368–2389 (1995).
103. Gaul, E.W. et al. Production and characterization of a fully ionized He plasma channel. *Appl. Phys. Lett.* **77**, 4112 (2000).
104. Volfbeyn, P., Esarey, E. & Leemans, W.P. Guiding of laser pulses in plasma channels created by the ignitor-heater technique. *Physics of Plasmas* **6**, 2269 (1999).
105. Nikitin, S.P., Alexeev, I., Fan, J. & Milchberg, H.M. High efficiency coupling and guiding of intense femtosecond laser pulses in preformed plasma channels in an elongated gas jet. *Phys. Rev. E* **59**, 3839–3842 (1999).
106. Hosokai, T. et al. Optical guidance of terrawatt laser pulses by the implosion phase of a fast Z-pinch discharge in a gas-filled capillary. *Opt. Lett.* **25**, 10-12 (2000).
107. Kaganovich, D., Satorov, P., Cohen, C. & Zigler, A. Variable profile capillary discharge for improved phase matching in a laser wakefield accelerator. *Appl. Phys. Lett.* **75**, 772 (1999).
108. Ehrlich, Y. et al. Guiding of high intensity laser pulses in straight and curved plasma channel experiments. *Phys. Rev. Lett.* **77**, 4186–4189 (1996).
109. Butler, A., Spence, D.J. & Hooker, S.M. Guiding of high-intensity laser pulses with a hydrogen-filled capillary discharge waveguide. *Phys. Rev. Lett.* **89**, 185003 (2002).
110. Esarey, E., Sprangle, P., Krall, J. & Ting, A. Overview of plasma-based accelerator concepts. *IEEE Trans. on Plasma Science* **24**, 252–288 (1996).
111. Yudin, L.A., Korenev, I.L., Kapchinsky, M.I. & Efimov, S.P. Electrodynamics as a problem of eigenvalues. II. Variational method of calculation of electromagnetic field oscillations in dispersive medium. *Phys. Plasmas* **3**, 47-51 (1996).
112. Esarey, E. & Leemans, W.P. Nonparaxial propagation of ultrashort laser pulses in plasma channels. *Phys. Rev. E* **59**, 1082 (1999).
113. Decker, C.D., Mori, W.B., Tzeng, K. & Katsouleas, T. The evolution of ultra-intense, short-pulse lasers in underdense plasmas. *Phys. Plasmas* **3**, 2047 (1996).
114. Nakajima, K. Compact X-ray sources: Towards a table-top free-electron laser. *Nature Physics* **4**, 92–93 (2008).
115. Leemans, W.P. et al. Observation of Terahertz Emission from a Laser-Plasma Accelerated Electron Bunch Crossing a Plasma-Vacuum Boundary. *Phys. Rev. Lett.* **91**, 074802 (2003).
116. Pai, C. et al. Production of Infrared Pulses from a Laser Wakefield Electron Accelerator. *Conference on Lasers and Electro-Optics/International Quantum Electronics Conference JWD3* (2009).
117. Nakajima, K. Compact X-ray sources: Towards a table-top free-electron laser. *Nature Physics* **4**, 92-93 (2008).

118. Schlenvoigt, H. et al. A compact synchrotron radiation source driven by a laser-plasma wakefield accelerator. *Nat Phys* **4**, 130-133 (2008).
119. Kalmykov, S.Y. et al. Numerical modelling of a 10-cm-long multi-GeV laser wakefield accelerator driven by a self-guided petawatt pulse. *New J. Phys.* **12**, 045019 (2010).
120. Faure, J. et al. Controlled injection and acceleration of electrons in plasma wakefields by colliding laser pulses. *Nature* **444**, 737-739 (2006).
121. Leemans, W. & Esarey, E. Laser-driven plasma-wave electron accelerators. *Phys. Today* **62**, 44 (2009).
122. Kimura, W.D. et al. First Staging of Two Laser Accelerators. *Phys. Rev. Lett.* **86**, 4041 (2001).
123. Kimura, W.D. et al. Demonstration of High-Trapping Efficiency and Narrow Energy Spread in a Laser-Driven Accelerator. *Phys. Rev. Lett.* **92**, 054801 (2004).
124. Dong, P. et al. Holographic visualization of laser wakefields. *New J. Phys.* **12**, 045016 (2010).
125. Wilks, S.C., Dawson, J.M., Mori, W.B., Katsouleas, T. & Jones, M.E. Photon accelerator. *Phys. Rev. Lett.* **62**, 2600 (1989).
126. Rosenzweig, J.B. et al. Experimental Observation of Plasma Wake-Field Acceleration. *Phys. Rev. Lett.* **61**, 98 (1988).
127. Marqu's, J.R. et al. Temporal and Spatial Measurements of the Electron Density Perturbation Produced in the Wake of an Ultrashort Laser Pulse. *Phys. Rev. Lett.* **76**, 3566 (1996).
128. Siders, C. et al. Plasma-based accelerator diagnostics based upon longitudinal interferometry with ultrashort optical pulses. *IEEE Transactions on Plasma Science* **24**, 301-315 (1996).
129. Siders, C.W. et al. Laser Wakefield Excitation and Measurement by Femtosecond Longitudinal Interferometry. *Phys. Rev. Lett.* **76**, 3570 (1996).
130. Bahk, S. et al. Generation and characterization of the highest laser intensities (10^{22} W/cm²). *Opt. Lett.* **29**, 2837-2839 (2004).
131. Le Blanc, S.P., Gaul, E.W., Matlis, N.H., Rundquist, A. & Downer, M.C. Single-shot measurement of temporal phase shifts by frequency-domain holography. *Opt. Lett.* **25**, 764-766 (2000).
132. Geindre, J. et al. Frequency-Domain Interferometer For Measuring The Phase And Amplitude Of A Femtosecond Pulse Probing A Laser-Produced Plasma. *Opt. Lett.* **19**, 1997-1999 (1994).
133. Andreev, N.E., Gorbunov, L.M. & Ramazashvili, R.R. Theory of a three-dimensional plasma wave excited by a high-intensity laser pulse in an underdense plasma. *Plasma Physics Reports* **23**, 277-284 (1997).
134. Kalmykov, S.Y., Gorbunov, L.M., Mora, P. & Shvets, G. Injection, trapping, and acceleration of electrons in a three-dimensional nonlinear laser wakefield. *Phys. Plasmas* **13**, 113102 (2006).
135. Shvets, G. & Li, X. Theory of laser wakes in plasma channels. *Phys. Plasmas* **6**, 591 (1999).

136. Shvets, G., Wurtele, J.S., Chiou, T.C. & Katsouleas, T.C. Excitation of accelerating wakefields in inhomogeneous plasmas. *IEEE Transactions on Plasma Science* **24**, 351 -362 (1996).
137. Marqu's, J.R. et al. Frequency Increase and Damping of Nonlinear Electron Plasma Oscillations in Cylindrical Symmetry. *Phys. Rev. Lett.* **78**, 3463 (1997).
138. Dawson, J.M. Nonlinear Electron Oscillations in a Cold Plasma. *Phys. Rev.* **113**, 383–387 (1959).
139. Bulanov, S.V., Pegoraro, F., Pukhov, A.M. & Sakharov, A.S. Transverse-wake wave breaking. *Phys. Rev. Lett.* **78**, 4205-4208 (1997).
140. Malka, V. et al. Second harmonic generation and its interaction with relativistic plasma waves driven by forward Raman instability in underdense plasmas. *Physics of Plasmas* **4**, 1127–1131 (1997).
141. Chen, S., Maksimchuk, A. & Umstadter, D. Experimental observation of relativistic nonlinear Thomson scattering. *Nature* **396**, 653-655 (1998).
142. Grigsby, F.B., Dong, P. & Downer, M.C. Chirped-pulse Raman amplification for two-color, high-intensity laser experiments. *J. Opt. Soc. Am. B* **25**, 346-350 (2008).
143. Dong, P. et al. Formation of Optical Bullets in Laser-Driven Plasma Bubble Accelerators. *Phys. Rev. Lett.* **104**, 134801 (2010).
144. Cusack, R., Huntley, J.M. & Goldrein, H.T. Improved noise-immune phase-unwrapping algorithm. *Appl. Opt.* **34**, 781-789 (1995).
145. Ting, A. et al. Temporal Evolution of Self-Modulated Laser Wakefields Measured by Coherent Thomson Scattering. *Phys. Rev. Lett.* **77**, 5377 (1996).
146. Thomas, A.G.R. et al. Effect of Laser-Focusing Conditions on Propagation and Monoenergetic Electron Production in Laser-Wakefield Accelerators. *Phys. Rev. Lett.* **98**, 095004 (2007).
147. Kaluza in press. (2010).
148. Yanovsky, V.P. et al. Ultra-High Intensity-High Contrast 300-TW Laser at 0.1 Hz Repetition Rate. *Conference on Lasers and Electro-Optics/Quantum Electronics and Laser Science Conference and Photonic Applications Systems Technologies JWD7* (2008).
149. Tzoufras, M. et al. Beam loading by electrons in nonlinear plasma wakes. *Phys. Plasmas* **16**, 056705 (2009).
150. Glinec, Y. et al. Direct observation of betatron oscillations in a laser-plasma electron accelerator. *Europhys. Lett.* **81**, 64001 (2008).
151. Matsuoka, T. & others Laser wakefield acceleration experiments at the University of Michigan. *AIP Conf. Proc.* **1086**, 184-189 (2009).
152. Wiggins, S.M. et al. Narrow spread electron beams from a laser-plasma wakefield accelerator. *Harnessing Relativistic Plasma Waves as Novel Radiation Sources from Terahertz to X-Rays and Beyond* **7359**, 735914-10 (2009).
153. Issac, R.C. et al. Electron beam pointing stability of a laser wakefield accelerator. *Harnessing Relativistic Plasma Waves as Novel Radiation Sources from Terahertz to X-Rays and Beyond* **7359**, 735915-7 (2009).
154. Oguchi, A. et al. Multiple self-injection in the acceleration of monoenergetic

- electrons by a laser wake field. *Phys. Plasmas* **15**, 043102 (2008).
155. Hidding, B. et al. Quasimonoenergetic electron acceleration in the self-modulated laser wakefield regime. *Phys. Plasmas* **16**, 043105 (2009).
 156. Yariv, A. *Quantum Electronics*. (Wiley: 1989).
 157. Mora, P. & Antonsen, T.M. Kinetic modeling of intense, short laser pulses propagating in tenuous plasmas. *Physics Of Plasmas* **4**, 217-229 (1997).
 158. PUKHOV, A. Three-Dimensional Electromagnetic Relativistic Particle-in-Cell Code VLPL (Virtual Laser Plasma Lab). *Journal of Plasma Physics* **61**, 425-433 (1999).
 159. Tzoufras, M. et al. Beam Loading in the Nonlinear Regime of Plasma-Based Acceleration. *Phys. Rev. Lett.* **101**, 145002 (2008).
 160. Maksimchuk, A. et al. Energy scaling of quasi-monoenergetic electron beams from laser wakefields driven by 40-TW ultra-short pulses. *Applied Physics B: Lasers and Optics* **89**, 201-207 (2007).
 161. Gallacher, J.G. et al. A method of determining narrow energy spread electron beams from a laser plasma wakefield accelerator using undulator radiation. *Phys. Plasmas* **16**, 093102 (2009).
 162. Prince, J.L. & Links, J. *Medical Imaging Signals and Systems*. (Prentice Hall: 2005).
 163. Li, Z. *submitted, Opt. Lett.* (2010).
 164. Kalmykov, S.Y. et al. Numerical modelling of a 10-cm-long multi-GeV laser wakefield accelerator driven by a self-guided petawatt pulse. *New J. Phys.* **12**, 045019 (2010).
 165. Gaul, E.W. et al. Demonstration of a 1.1 petawatt laser based on a hybrid optical parametric chirped pulse amplification/mixed Nd:glass amplifier. *Appl. Opt.* **49**, 1676-1681 (2010).
 166. Blumenfeld, I. et al. Energy doubling of 42 GeV electrons in a metre-scale plasma wakefield accelerator. *Nature* **445**, 741-744 (2007).
 167. Lee, S. et al. Energy doubler for a linear collider. *Phys. Rev. ST Accel. Beams* **5**, 011001 (2002).
 168. Lee, S., Katsouleas, T., Hemker, R.G., Dodd, E.S. & Mori, W.B. Plasma-wakefield acceleration of a positron beam. *Phys. Rev. E* **64**, 045501 (2001).
 169. Muggli, P., Yakimenko, V., Babzien, M., Kallos, E. & Kusche, K.P. Generation of Trains of Electron Microbunches with Adjustable Subpicosecond Spacing. *Phys. Rev. Lett.* **101**, 054801 (2008).
 170. Cavalieri, A.L. et al. Clocking Femtosecond X Rays. *Phys. Rev. Lett.* **94**, 114801 (2005).

Vita

Peng Dong was born in Beijing, China on Jan 15th, 1980, the son of Guijin Dong and Xiuzhen Li. He received the Bachelor of Science degree in Physics from Jilin University (Changchun, China) in 2002. He began his graduate study in University of Texas at Austin from August, 2002. His doctoral work in Femtosecond Spectroscopy Laboratory is supervised by Professor Michael C. Downer.

Permanent address: Beijing

This dissertation was typed by Peng Dong.